Efficient time-integration schemes for discontinuous Galerkin non-hydrostatic atmospheric models

by

Lei Bao

B.A., Wuhan University, 2010

M.S., University of Colorado at Boulder, 2014

A thesis submitted to the

Faculty of the Graduate School of the

University of Colorado in partial fulfillment

of the requirements for the degree of

Doctor of Philosophy

Department of Applied Mathematics

2016

This thesis entitled:
Efficient time-integration schemes for discontinuous Galerkin non-hydrostatic atmospheric models
written by Lei Bao
has been approved for the Department of Applied Mathematics

_____

Prof. Henry M. Tufo

_____

Dr. Ram Nair

Date _____

The final copy of this thesis has been examined by the signatories, and we find that both the content and the form meet acceptable presentation standards of scholarly work in the above mentioned discipline.

Bao, Lei (Ph.D., Applied Mathematics)

Efficient time-integration schemes for discontinuous Galerkin non-hydrostatic atmospheric models

Thesis directed by Prof. Henry M. Tufo

This thesis presents the ongoing work on the numerical aspects of designing a numerical framework on which to build a high-resolution atmospheric model using the discontinuous Galerkin (DG) methods. As the horizontal resolution exceeds the hydrostatic limit ($1/10^\circ$ or 10 km), which is usually referred as the non-hydrostatic (NH) scale, the compressible Euler system must be employed to characterize the motion of the air flow.

To simulate this system numerically, we consider the DG method for the spatial discretization and cubed-sphere grid system. The High-Order Method Modeling Environment (HOMME) is a highly scalable hydrostatic dynamical core based on spectral element and/or DG methods. It utilizes cube-sphere geometry and shows great scalability. Our goal is to extend HOMME-DG model to the non-hydrostatic scale.

We use the global shallow water equations to study the influence of the full conservative equation sets in conserving integral invariants is rigorously compared against the vector-invariant form. Several important components, such as the horizontal discretization and numerical diffusion are also discussed briefly.

The terrain-following height-based coordinate transform is adopted to handle the orography. For the time discretization, we consider a Horizontally explicit and Vertically implicit operator splitting based on Strang-splitting approach. HEVI treats the vertical component implicitly and the horizontal component explicitly. As a consequence, the maximum allowed time-step size is only constrained by the horizontal grid spacing, which is usually several orders of magnitude higher than the vertical. We compare HEVI operator splitting with Implicit-explict (IMEX) linear-nonlinear splitting ideas. We also perform the linear stability study of various IMEX Runge-Kutta schemes. HEVI-Strang splitting shows large stability region in the well-resolved scale and only requires one

implicit solve compared with other IMEX-RK schemes. This study is the first time testing the DG scheme with the dimensional splitting approach. The HEVI-Strang scheme shows qualitatively comparable results at a more lower computational cost. The efficiency of the linear solver resulting from the Newton's method is also investigated. A right preconditioner is suggested to improve the convergence of the GMRES iterative solver. Numerical results show that the preconditioned GMRES and the direct solvers are both viable options to solve the vertical implicit component.

The global 3D DG-NH model is constructed by vertical stacking of the horizontal cubes-sphere layers. The 3D global advection problem is tested using two DCMIP test cases. We also present some preliminary results for the non-hydrostatic inertia gravity wave test utilizing the HEVI-Strang time integration scheme. The results of 3D DG-NH model based on HEVI-Strang time integration scheme are qualitatively in line with other non-hydrostatic models. The time-step size of the HEVI-Strang scheme is not affected as the vertical grid spacing varies and the 3D DG-NH model maintains the scalability of the HOMME framework.

Dedication

To Mom Yuqin - my love will always be with you.

Acknowledgements

First of all, I would like to say thanks my parents for the years and years of support and encouragement. They are so thoughtful and helpful throughout my entire life. I want to say thank you to my mom again. Your devotion and endless support are the main source of my courage and my confidence in my journey. I would not have made it through without you.

I would like to extend my deepest gratitude to my supervisors Henry M. Tufo and Ram D. Nair for very interesting and challenging topic of this thesis, for the enduring support during the past four years. I want to express a special thank you to Ram D. Nair for your support and your insight into both the mathematics and also the physical understanding. You are not only the supervisor who guide me in the academic exploration, but also my life mentor. It is a great pleasure to work with you.

I'd like to thank the Department of Applied Mathematics for all the support I received as a graduate student. Thank you so much, my friends in Boulder. You guys really make my life in Boulder vivid and colorful. It is so lucky to meet you, my dear friends.

Many thanks go to my NCAR buddies. Thank you so much for supporting me and accompanying me. I want to offer thanks to the SIParCS intern program. It is a really wonderful program that I met a lot of friends. To me, NCAR is like a warm family. When I have any trouble, you are always the first one to step in and help me through. I am very grateful to all of you.

Most importantly, I would like to thank my boyfriend, Liang Wang. Your companionship has made my life here so sweet. Your support through stressful times and your share through happy moments is invaluable to me.

Contents

Chapter

Tables

Table

Figures

Figure

Chapter 1

Introduction

1.1 Motivations: Why non-hydrostatic models?

Atmospheric models are a powerful tool to study the statistical properties and long term trends of the climate system. By nature, the atmosphere consists of a vertical stack of stratified horizontal layers. To model the atmosphere, the horizontal resolution typically ranges from $\mathcal{O}(10^3)$ m to $\mathcal{O}(10^5)$ m depending on the applications, while the vertical resolution varies little by applications and goes from $\mathcal{O}(10)$ m to $\mathcal{O}(10^3)$ m. The aspect ratio between horizontal and vertical resolution is about $\mathcal{O}(10^2)$ for high-resolution weather applications and is about $\mathcal{O}(10^4)$ for climate modeling [49]. To study the atmospheric dynamics, hydrostatic models have been primarily used for the past several decades. They approximate the vertical structure of the atmosphere to be in a state of hydrostatic balance. Under this approximation, the vertical velocity is no longer a prognostic quantity but is instead determined using the computed pressure and divergence of the horizontal velocity field. This approximation works well when the horizontal grid spacing is much larger than the vertical grid spacing and is larger than $1/10^\circ$ (10 km). However, with the increasing computing resources available to atmospheric modelers, the grid resolution is reaching the hydrostatic limit.

Since the target resolution for global modeling is getting close to the non-hydrostatic scale, the hydrostatic balance approximation is no longer valid to model the underlying dynamics, therefore a non-hydrostatic atmosphere model is a must in this regime. Hydrostatic models cannot adequately represent clouds and it requires the use of cumulus parameterizations to incorporate the effects

of deep convection. However, cumulus parameterizations are the most ambiguous and expensive factor in climate models.

Unlike hydrostatic models, non-hydrostatic (NH) models make no approximation to the vertical structure of the atmosphere and so allow for features such as horizontal transport of vertical momentum. As a consequence, high resolution NH models overcome the cumulus parameterization issue by explicitly calculating deep convective circulations over the global domain without using cumulus parameterizations. In other words, global NH models are "cloud-resolving models", in which we explicitly represent the clouds instead of using a sub-grid scale model to parameterize it. Moreover, to study extreme weather events caused by climate change, including floods, droughts, severe storms, a fine resolution atmospheric model also helps to meet this need. With the arrival of petascale computing resources with core counts ranging from tens of thousands to hundreds of thousands to millions, the construction of efficient global NH models has always been feasible but applying them for the operational climate model is still challenging. There have been vast research efforts devoted to developing non-hydrostatic atmospheric model using novel ideas, such as finite volume methods and spectral element methods [2, 10, 27, 47, 61, 77, 91] in recent years.

1.2 Challenges for non-hydrostatic modeling

To characterize the atmospheric motion in the NH scale, the hydrostatic primitive equation sets are not valid any more. The compressible Euler equations or Navier-Stokes equations will be employed, or a filtered set of those equations that removes the overly time-step restrictive sound waves. We choose the compressible Euler equations, which describes the motion of fluids from a set of conservation laws: conservation of mass, momentum, energy and tracers.

To build a full global NH model, solving the shallow water equations (SWE) is usually a first step in designing the numerical framework. The SWE can be derived from the compressible Euler equations under the assumption that the vertical dimension is much smaller than the horizontal scale. The equations contain all the horizontal aspects found in 3D NH models [26] including but not limited to horizontal motions such as inertial gravity waves and Rossby waves [32, 73]. The

SWE is widely used as a test-bed for designing discretization techniques used in complex 3D models. The SWE framework allows one to answer some questions about the horizontal discretization and physical conservation properties at a much lower computational cost.

Research in Non-hydrostatic modeling faces many scientific and computational challenges. For example, there is a strong demand for satisfaction of built-in physical conservation laws (e.g., conservation of mass, energy, enstrophy, etc.). One solution is to require that the governing equations be cast in a conservative form or flux form. The importance of the conservative form of the governing equation set becomes more evident in the non-hydrostatic scale [27]. A study in the context of SWE can give us some insights of the influence of the conservative form in the full atmosphere model.

The conventional lat-lon geometry has polar singularities due to the convergence of meridian lines. Non-local polar filtering required by such grid systems greatly impacts the parallel efficiency of Eulerian grid-point models that relied on such grid systems [45]. To address this issue, the cubed-sphere geometry is reintroduced to the global modeling community [54, 55, 92]. The cubed-sphere geometry avoids the pole problem by inscribing the cube in a sphere and using a central (gnomonic) projection from the sphere to the cube [70], resulting in a quasi-uniform grid on the sphere under the equiangular projection.

In addition, the numerical algorithms should have the local properties such as high on-processor floating-point operation count and minimum parallel communication overhead. The discontinuous Galerkin (DG) method is a high-order discretization techniques that combines the attractive properties from both finite element (or spectral element SE) and finite volume (FV) methods. The DG method is rigorously based on conservation laws as in the case of a finite-volume method, but retains all the merits of the SE approach while being more flexible on various grid types and mesh adaptivity. DG is an appealing option for the spatial discretization in the NH atmospheric model.

The High-Order Method Modeling Environment (HOMME) [1] is a set of hydrostatic models built on finite-element-type compact methods, including spectral element and DG in the horizontal

and relies on cubed-sphere grid system. HOMME has been adopted as the default dynamical core for the NCAR Community Atmospheric Model (CAM) [16] due to its salient features such as its inherent scalability and single thread performance. As a consequence, a three-dimensional (3D) DG-NH model, based on the Euler/Navier-Stokes system of equations in the HOMME framework [1], is considered for this study. For the 3D DG-NH model, the inherent horizontal aspects of the domain will remain the same as the current HOMME cubed-sphere grid system, while the vertical discretization is based on the terrain-following z-coordinate system.

Explicit time integration schemes are popular in the atmospheric community because they are easy to implement and the locality of data allows efficient evaluation of the the equations of motions on large-scale parallel machines. So, instead of filtering the acoustic wave (i.e. anelastic approximation), we decide to solve the entire system without modifying the governing equations. In general, the maximum stable explicit time step size is constrained by the Courant-Freidrichs-Lewy (CFL) condition, which is defined as

$$\tau = \frac{c_{max}\Delta t}{\Delta x}, \tag{1.1}$$

where c_{max} is the maximum wave speed of the system, Δx is the grid spacing, and Δt is the maximum stable time step size. For most explicit time-integration schemes $\tau \leq 1$. However, the fast moving acoustic waves, together with gravity waves, and the large aspect ratio between horizontal and vertical resolution impose a significant time step restriction in the explicit time-integration methods. Although a variety of time-stepping schemes rely on implicit and semi-implicit methods available, it is not clear how computationally efficient (or parallel efficient) these schemes are for a complex problem such as global climate simulation. The "horizontally explicit and vertically implicit" or HEVI scheme, addresses these issues by treating the vertically propagating waves implicitly while still using an explicit scheme to solve the terms responsible for horizontal wave motion. As a consequence, the Courant-Friedrichs-Lewy (CFL) stability restriction is only constrained by the horizontal grid-spacing, which is typically several orders of magnitude larger than the vertical grid-spacing. Moreover, for the atmospheric community, the domain decomposition is

usually in the horizontal, maintaining an entire vertical column on a single processor. By using the HEVI time discretization, the vertical implicit component can be efficiently solved with no inter-processor communication. Therefore, HEVI is a practical and efficient choice for the atmospheric numerical framework under consideration here.

One of the most challenging practical issue with the 3D climate model development is testing (debugging) the model (code), which requires huge computing resources due to the problem size and relatively smaller time integration rate. Fortunately, most of the problematic issues resulting from the vertical discretization and time integration schemes can be reliably tested in a simple 2D (x-z) setup. To this end, a 2D non-hydrostatic (NH) compressible Euler (Navier-Stokes) model based on the DG method in (x, z)-plane, is used to study the vertical aspect of the atmospheric dynamics in the NH scale.

The 3D DG-NH model can be constructed by vertically stratified horizontal layers, where the vertical grid system is based on a terrain-following height-based coordinate and the horizontal grid is used cubed-sphere geometry. The HEVI time-integration schemes can be evaluated in this full 3D model. The quality of the model will be validated through dynamical-core model-intercomparison project (DCMIP) test suite [34].

1.3 Outline of This Work

In this thesis, we study several numerical aspects of constructing a NH model in the HOMME framework. In particular, the HEVI time integration schemes are investigated for the two- and three- dimensional Euler system. For the atmospheric application, HEVI is widely used and shown to be a viable and practical choice for NH models.

The thesis is organized as follows. In Chapter 2, we describe the cubed-sphere geometry used for horizontal layers and the discontinuous Galerkin spatial discretization method. In Chapter 3, we study the influence of the conservation form, or flux form, of the equation sets in the shallow-water framework. A HEVI scheme based on Strang-splitting is studied in Chapter 4 in a 2D Cartesian plane to address the issue of the small time-step size at the NH scales. The linear stability analysis

and the efficiency comparison of various IMEX-RK schemes in the HEVI context is presented in Chapter 5. In Chapter 6, we show our ongoing work to construct a 3D DG-NH model and test the HEVI-Strang scheme in this framework. We summarize our work and provide some future research direction in Chapter 7. Supplementary materials are provided in the Appendices.

1.4 Publications

The following manuscripts have been published in investigating this thesis.

1. R. Nair, L. Bao, M. Toy. A Time-Split Discontinuous Galerkin Transport Scheme for Global Atmospheric Model. Procedia Computer Science, 51:20562065, 2015. 2015

2. L. Bao, R. D. Nair, and H. M. Tufo. A mass and momentum flux-form high-order discon- tinuous Galerkin shallow water model on the cubed-sphere. J. Comput. Phys., 271(0):224-243, 2014

3. L. Bao, R. Klöfkorn, and R. D. Nair. Horizontally explicit vertically implicit (HEVI) type time integration scheme for a discontinuous Galerkin non-hydrostatic model. Monthly Weather Review, 2015.

1.5 Contributions

- *Study of the vector-invariant form and flux-form of the equation sets on the cubed-sphere geometry using the discontinuous Galerkin spatial discretization*

  The conservation performance of two forms of equation sets are evaluated using several benchmark test cases. Several numerical aspects of the horizontal component of the full 3D DG-NH model are also studied. The flux-form of the compressible Navier-Stokes equations is adopted as the governing equations to characterize the idealized NH air flow.

- *Comparison of fully explicit and HEVI time integration approach and exploration for possible efficiency improvement.*

  Horizontal-explicit-vertical-implit (HEVI) scheme is considered for the time integration

scheme. The numerical experiments in the simplified 2D Cartesian plane show that the HEVI scheme can overcome the CFL constraint due to the small vertical grid spacing and thus the simulations are comparable to the unsplit version. The terrain-following height-based coordinate system is capable of handing tough oragraphy. The artificial viscosity works effectively with HEVI and stabilizes the flow field. This is the first work using the operator splitting DG method.

- *Contruction and verification of HEVI-Strang time integration in the 3D discontinuous Galerkin non-hydrostatic model*

  The accuracy of the model is examined using advection test cases. The 3D inertia gravity wave test is chosen to verify the scalability of the 3D DG-NH model. The parallel efficiency is tested under moderate horizontal-vertical aspect ratio. The strong scalability result demonstrates that HEVI-Strang relaxes the CFL constraint while maintaining the scalability of HOMME framework.

Chapter 2

Mathematical Formulation

In this chapter, we will discuss the cubed-sphere grid system and discontinuous Galerkine (DG) spatial discretization.

2.1 Cubed-sphere geometry

The cubed-sphere was originally introduced by Sadourny [71], and variants including equiangular projection were developed by Ronchi et al. [67] and Rančić et al. [64]. Let sphere **S** be the physical domain, which is the surface of the planet earth. The left panel in Fig. 2.1 is a schematic of physical domain on a cubed-sphere grid. **S** is partitioned into six identical patches that are obtained by the projection of the faces of an inscribed cube. In the present model, we consider the gnomonic (equiangular) central projection [71], which is nonorthogonal but more uniform than the conformal mapping [64]. The salient features of the resulting gnomonic coordinate system on **S** are a global grid system without polar singularities, and identical metric terms on each panel with quasi-uniform grid cells [59]. We define the local equiangular coordinate system of each face as $x^1 = x^1(\lambda, \phi), x^2 = x^2(\lambda, \phi)$, where $x^1, x^2 \in [-\pi/4, \pi/4]$ and λ, ϕ are the longitude and latitude of a sphere with radius R. Let $\mathbf{a_1}, \mathbf{a_2}$ be the covariant base vectors of the transformation between the inscribed cube **C** and the spherical surface **S**, then the corresponding transformation matrix is defined as:

$$A = \begin{bmatrix} \cos\phi\partial\lambda/\partial x^1 & \cos\phi\partial\lambda/\partial x^2 \\ \partial\phi/\partial x^1 & \partial\phi/\partial x^2 \end{bmatrix} = [\ \mathbf{a_1} \quad \mathbf{a_2}\ ].$$

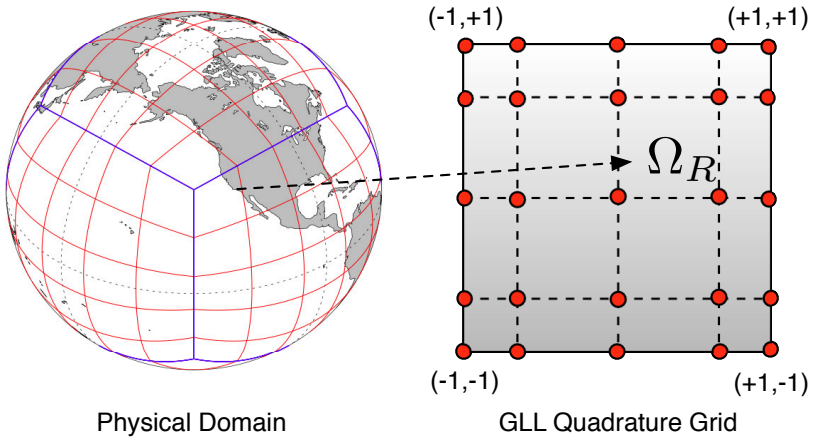

Figure 2.1: A schematic of a cubed-sphere grid with quadilateral elements is shown in the left panel. The right panel shows a reference element Ω_e with 5×5 GLL quadrature grid points. Each element Ω_{ij} on the cube face of the physical domain is mapped onto a unique reference element Ω_R. The mapping from the physical domain to the reference element is given in (2.5).

The corresponding metric tensor G_{ij} is

$$G_{ij} = \frac{R^2 \sec^2 x^1 \sec^2 x^2}{1 + \tan^2 x^1 + \tan^2 x^2} \begin{pmatrix} 1 + \tan^2 x^1 & -\tan x^2 \tan x^1 \\ -\tan x^1 \tan x^2 & 1 + \tan^2 x^2 \end{pmatrix} = A^T A,$$

where $i, j \in \{1, 2\}$, and the Jacobian of the transformation is $\sqrt{G} = [\det(G_{ij})]^{1/2}$. Details of the local transformation can be found in [56], and we will not further discuss herein.

The transformation of the horizontal wind vector $\mathbf{v} = (u, v)$ to local cubed-sphere contravariant components (u^1, u^2) and covariant components (u_1, u_2), respectively, can be written as:

$$\begin{bmatrix} u \\ v \end{bmatrix} = A \begin{bmatrix} u^1 \\ u^2 \end{bmatrix}, A^T \begin{bmatrix} u \\ v \end{bmatrix} = \begin{bmatrix} u_1 \\ u_2 \end{bmatrix},$$

and the covariant components and contravariant components are related via $u_i = G_{ij} u^j, u^i = G^{ij} u_j$, and $G^{ij} = G_{ij}^{-1}$.

2.2 Nodal Discontinuous Galerkin Discretization

The DG method is usually termed as a hybrid scheme, combining the best properties of spectral element and FV methods. The application of DG methods in the atmospheric community is a vigorous research field (see, [53] for details), and we only provide a brief outline of the DG discretization process herein.

Without loss of generality, DG discretization to a generic form of conservation laws is illustrated here for the purpose of simplicity:

$$\frac{\partial}{\partial t}U + \nabla \cdot \mathbf{F}(U) = S(U), \text{ in } \mathbf{D} \times (0, t_T], \tag{2.1}$$

where U is a scalar variable, which may include the metric term $\sqrt{G}$, $\mathbf{F} = (F_1, F_2)$ is the flux function, $S(U)$ is the source term, t_T is the total time period, and $\nabla = (\partial/\partial x^1, \partial/\partial x^2)$ is the gradient operator [56], which is not constrained to a particular grid system. Initially, $U_0(x, z) = U(x^1, x^2, t = 0)$ and suitable boundary conditions are imposed.

The DG spatial discretization procedure consists of partitioning the domain $\mathcal{D}$ into non-overlapping $N_{x^1} \times N_{x^2}$ regular elements Ω_{ij}, such that

$$\Omega_{ij} = [x^1_{i-1/2}, x^1_{i+1/2}] \otimes [x^2_{j-1/2}, x^2_{j+1/2}],$$

$i = 1, \ldots, N_{x^1}$, $j = 1, \ldots, N_{x^2}$. In a DG method, we seek for an approximate solution U_h, which belongs to a finite-dimensional space $\mathcal{V}_h$ consisting of polynomials of degree up to N:

$$\mathcal{V}_h = \mathcal{V}_h^N = \{\varphi : \varphi|_{\Omega_e} \in P^N(\Omega_e), \quad \forall \quad \Omega_e \in \mathbf{D}\}, \tag{2.2}$$

where

$$P^N(\Omega) = \text{span}\{(x^1)^l (x^2)^m : 0 \le l, m \le N, \quad \forall \quad (x^1, x^2) \in \Omega\},$$

denotes the space of all polynomials over Ω with degree at most N. The aforementioned process is identical on each element, so we consider a generic element Ω_e herein.

The semidiscretized weak Galerkin formulation for (2.1) on each element Ω_e is given by [13]:

$$\frac{d}{dt}\int_{\Omega_e} U_h \phi_h d\Omega - \int_{\Omega_e} \mathbf{F}(U_h) \cdot \nabla \varphi_h d\Omega + \int_{\Gamma_e} \hat{\mathbf{F}} \cdot \mathbf{n} \varphi_h d\Gamma = \int_{\Omega_e} S(U_h) \varphi_h d\Omega, \tag{2.3}$$

where φ_h is a test function from test space $\mathcal{V}_h$, and $\mathbf{n}$ is the outward unit normal vector along the element boundary Γ_e. $\hat{\mathbf{F}}$ is the numerical flux as defined below, which is crucial to resolve the discontinuity of the inter-element solutions. In general, high-order DG schemes employing polynomials of degree up to N are often referred to as P^N-DG methods.

For simplicity, we choose Lax-Friedrichs numerical flux here:

$$\hat{\mathbf{F}}(U_h) = \frac{1}{2}\{[\mathbf{F}(U_h^-) + \mathbf{F}(U_h^+)] \cdot \mathbf{n} - \alpha(U_h^+ - U_h^-)\}, \tag{2.4}$$

where U_h^- and U_h^+ are the left and right limits of U_h evaluated along Γ_e such that U_h^- is inside the element Ω_e and U_h^+ is outside of Ω_e, α is the maximum of the absolute value of eigenvalues of the flux Jacobian in the direction $\mathbf{n}$.

The choice of a suitable set of basis functions for $\mathcal{V}_h$ is also vital for an accurate and efficient evaluation of the integrals in the weak form (2.3). An orthogonal polynomial basis set, such as Lagrange-Legendre polynomial, is highly preferred for efficiency. Levy et al. [46] has shown that the nodal DG exhibits better computational efficiency than the modal version, therefore, we consider the nodal DG version in the present study.

2.2.1 Nodal Basis Functions and Numerical Integration

The integral equation (2.3) plays a central role in the DG discretization. The accuracy and efficiency of the scheme are greatly dependent on the particular choice for $\mathcal{V}_h^N$ and the quadrature rules chosen for the surface and line integrals. To make use of an efficient quadrature rule, consider a one-to-one mapping (2.5) from an element Ω_{ij} to a reference element $\Omega_R = [-1, 1] \times [-1, 1]$, as shown in Fig. 2.1.:

$$\begin{aligned} \xi &= \frac{2(x^1 - x_i^1)}{\Delta x_i^1},\ x_i^1 = (x_{i+1/2}^1 + x_{i-1/2}^1)/2, \\ \eta &= \frac{2(x^2 - x_j^2)}{\Delta x_j^2},\ x_j^2 = (x_{j+1/2}^2 + x_{j-1/2}^2)/2, \end{aligned} \tag{2.5}$$

where $(\xi, \eta) \in \Omega_R$ are local independent variables.

For the computational efficiency, the nodal DG discretization is considered in the present work. For the nodal DG discretization, the Lagrange polynomials $\{h_l(\xi)\}_{l=0}^{N}$ are adopted as the basis functions, and they satisfy the discrete orthogonal properties,

$$\begin{aligned} h_l(\xi_m) &= \delta_{lm}, \\ \int_{-1}^{1} h_l(\xi)\, h_m(\xi)\, d\xi &\simeq w_l\, \delta_{lm}, \end{aligned}$$

where w_l are the weights associated with the underlying quadrature rule and δ_{lm} is the Kronecker function ($\delta_{lm} = 0$ if $l \neq m$, $\delta_{lm} = 1$ if $l = m$). There are a range of choices for the quadrature rules,

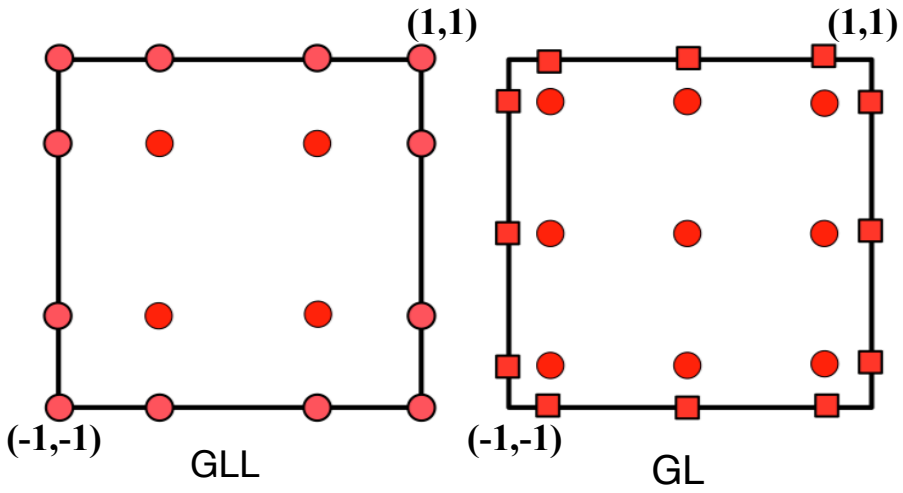

Figure 2.2: The reference element and the corresponding Lagrange polynomials with roots at 4×4 GLL grid (left) and 3×3 Gauss-Legendre (GL) grid (right). For GL grid, values at the flux-points (filled square) are computed from the interior points by 1D interpolation along the ξ or η coordinate direction.

among which Gauss-Legrendre (GL) and Gauss-Lobatto-Legrendre (GLL) quadrature rules are the most popular. For the GL grid with the quadrature points $\{\xi_m\}_{m=0}^{N}$, the Lagrange polynomial $\{h_l(\xi)\}_{l=0}^{N}$ and the corresponding weight are given as,

$$h_l(\xi)\,|_{GL} = \frac{P_{N+1}(\xi)}{P'_{N+1}(\xi_l)\,(\xi - \xi_l)}, \quad w_l\,|_{GL} = \frac{2}{(1-\xi_l^2)[P'_{N+1}(\xi_l)]^2}, \tag{2.6}$$

while for the GLL grid,

$$h_l(\xi)\,|_{GLL} = \frac{(\xi-1)(\xi+1)P'_N(\xi)}{N(N+1)P_N(\xi_l)(\xi-\xi_l)}, \quad w_l\,|_{GLL} = \frac{2}{N(N+1)[P_N(\xi_l)]^2}, \tag{2.7}$$

where $P_N(\xi)$ is the N^{th} degree Legendre polynomial and $P'_N(\xi)$ is its derivative. Fig. 2.2 shows schematic plots for 4×4 GLL grid and 3×3 GL grid.

For P^N-DG methods, the GL quadrature rule provides the exact integration of (2.3) while GLL does not. The GL quadrature rule is accurate up to $(2N+1)$-order, while GLL is accurate up to $(2N-1)$-order for a given degrees of freedom. Thus, GL is more suitable when a moderate order of approximation is used. However, in terms of the computational efficiency and implementation simplicity, a GLL grid is more beneficial than a GL grid. GL grid excludes the end points ± 1 and requires additional extrapolation process to obtain the flux values at the edges $(\xi, \eta = \pm 1)$, while in the case of GLL grid, the solution points coincide with the flux points. Thus, for high-order (N>5) approximations, GLL might be a better candidate because the loss of accuracy from the inexact integration may not significantly impact the solution. As a consequence, the GLL grid is used for the horizontal grid, whereas the GL grid is used for the vertical grid. The corresponding approximate resolution on GL and GLL grids are computed as:

$$\begin{aligned} \Delta\hbar\,|_{GL} &= \frac{x_{j+1/2} - x_{j-1/2}}{N+1} \\ \Delta\hbar\,|_{GLL} &= \frac{x_{j+1/2} - x_{j-1/2}}{N} \end{aligned}$$

For 2D problems, as in the case of the DG-NH model, we use a tensor product of the Lagrange functions to form the basis set $\{h_l(\xi)h_m(\eta)\}$ which spans $P^N(\Omega_e)$ in (2.2), where $l, m = 0, 1, \ldots, N$. In this way, the approximate solution $U_h(\xi, \eta, t)$ and the test function $\varphi_h(\xi, \eta)$ are expressed as,

$$U_h(\xi, \eta, t) = \sum_{l=0}^{N} \sum_{m=0}^{N} U_{lm}(t)\, h_l(\xi) h_m(\eta), \tag{2.8}$$

$$\varphi_h(\xi, \eta) = h_l(\xi) h_m(\eta). \tag{2.9}$$

where $-1 \leq \xi, \eta \leq 1$ and $U_{lm}(t)$ denotes the nodal (gridpoint) values of the approximate solution U_h at time t.

In the current study, we are focusing only on **moderate** order P^N-DG discretization for the DG-NH model with $N \leq 4$. Note that a major limitation of the DG scheme is the stringent CFL stability constraint associated with the explicit time stepping. Reducing the order of accuracy

significantly improves the CFL stability restriction with explicit time stepping and therefore allows for implementation of limiting (positivity-preserving) algorithms, based on those designed for FV methods [101].

The same order of quadrature rule is adopted both for the internal surface integrals in Ω_e and for the boundary flux integrals along the boundary Γ_e. Because, this setting is significantly efficient at the cost of negligible inaccuracy due to the inexact integration [58]. Substituting (2.9), (2.8) into the weak formulation (2.3) and simplifying the resulting equation lead to an ODE system in time,

$$\frac{dU_{mn}}{dt} = \mathcal{L}(U_{mn}), \text{ in } (0, t_T], \tag{2.10}$$

where $\{U_{mn}\}$ are time-dependent values of U_h at the grid points (x_m^1, x_n^2).

2.2.2 Artificial diffusion effects

The design of the diffusion scheme is primarily based on the model's spatial discretization. There are various approaches to invoke diffusivity in atmospheric models, and the most popular choice is the second-order explicit diffusion (∇^2). The Local Discontinuous Galerkin (LDG) method [15], which takes inter-element contributions into account when treating the diffusion term (Laplacians), shows better consistency in addressing the discontinuous nature of the discretization [6, 51]. In order to suppress these spurious accumulation, horizontal diffusion is usually preferred and added in the discrete model [58]. In [58], the LDG approach [15] is implemented for the vector-invariant form of SWEs, where the LDG scheme used is based on a simple Bassi-Rebay scheme [7]. Consider the scalar component of conservation laws,

$$\frac{\partial}{\partial t}U + \nabla \cdot \mathbf{F}(U) = S(U) + \nu\Delta^2(U). \tag{2.11}$$

Introduce a new variable $\mathbf{q} = \nu\nabla U$, and rewrite the above problem as a first-order system on $\mathbf{D}$:

$$\mathbf{q} - \nu\nabla U = 0, \tag{2.12}$$

$$\frac{\partial U}{\partial t} + \nabla \cdot \mathbf{F}(U) - \nabla \cdot \mathbf{q} = S(U). \tag{2.13}$$

On each element Ω_e with the boundary Γ_e, multiplying (2.12) by a vector test function $\mathbf{w}$, applying Green's method twice, and with the central flux for the evaluation of the flux associated with U_h along Γ_e (see (13)-(14) in [58] for details), the weak formulation of (2.12) leads to:

$$\int_{\Omega_e} \mathbf{q}_h \cdot \mathbf{w}\, d\Omega = \int_{\Gamma_e} \frac{1}{2}(U_h^+ - U_h^-)\mathbf{w} \cdot \mathbf{n}\, d\Gamma + \int_{\Omega_e} \nabla U_h \cdot \mathbf{w}\, d\Omega, \tag{2.14}$$

where $\frac{1}{2}(U_h^+ - U_h^-)$ is called jump flux.

The semidiscretized weak formulation of (2.13) takes the form:

$$\begin{aligned} \frac{d}{dt}\int_{\Omega_e} U_h \varphi_h d\Omega - \int_{\Omega_e} \mathbf{F}(U_h) \cdot \nabla \varphi_h d\Omega + \int_{\Gamma_e} [\mathbf{F}(U_h)] \cdot \mathbf{n} \varphi_h d\Gamma \\ + \quad \left(\int_{\Omega_e} \mathbf{q}_h \cdot \nabla \varphi_h d\Omega - \int_{\Gamma_e} [\mathbf{q}_h] \cdot \mathbf{n} \varphi_h d\Gamma \right) \\ = \int_{\Omega_e} S(U_h) \varphi_h d\Omega, \end{aligned} \tag{2.15}$$

where $[\mathbf{q}_h]$ is evaluated through the central flux $(\mathbf{q}_h^+ + \mathbf{q}_h^-)/2$. Although various options for the numerical fluxes are available as listed in [4], for simplicity [58], we choose the combination of jump flux and central flux here for the evaluation of (2.14) and (2.15).

The DG methods, like many other high-order methods, such as RBFs [20] and spectral element methods, often require an artificial diffusion effect to stabilize the fields and obtain a high-quality solution. For an artificial diffusion term (or a numerical diffusion), ν depends not only on the problem itself but also the grid resolution $\Delta\hbar$. ν is chosen in a way that the diffusion effect can, to some extent, eliminate the noise in the numerical solution, but not too large to destroy the physical features of the problem. Furthermore, it is required that as $\Delta\hbar \to 0$, $\nu \to 0$. This is different from a physical diffusion (as in a viscous flow problem), where ν relies entirely on the viscosity of the flow and is irrelevant of $\Delta\hbar$. In terms of the artificial diffusion, a rigorous selection of ν can be made by studying the kinetic spectra [19], which is beyond the scope of the present study. Artificial diffusion is especially important when constructing dynamic core for atmosphere modeling [35, 85]. In the current paper, we consider the influence of an artificial diffusion effect on our DG flux-form model. For a benchmark advection-diffusion problem, usually the analytic solution is available to test the convergence of the diffused solution. Although the convergence

study of DG with artificial diffusion effect can hardly be performed, a deviation of the diffused solution from the non-diffused solution can be shown by fixing ν when varying $\Delta\hbar$.

2.3 Time integration schemes

Strong stability-preserving (SSP) Runge-Kutta schemes are widely used in practice because they preserve stability and are flexible to increase temporal accuracy [29]. We employ a third-order accuracate SSP Runge-Kutta scheme for the time integration in the present study:

$$\begin{aligned} U^{(1)} &= U^n + \Delta t L(U^n), \\ U^{(2)} &= \tfrac{3}{4}U^n + \tfrac{1}{4}[U^{(1)} + \Delta t L(U^{(1)})], \\ U^{n+1} &= \tfrac{1}{3}U^n + \tfrac{2}{3}[U^{(2)} + \Delta t L(U^{(2)})]. \end{aligned} \tag{2.16}$$

Although efficient time stepping schemes, such as the implicit and semi-implicit time integration approaches, are available for DG methods, for simplicity, we consider only explicit SSP-RK method. The explicit time stepping method has a stringent CFL stability restriction for the DG methods, nevertheless, it offers high-order temporal accuracy. Note that, we use relatively small time steps for the numerical experiments for minimizing the possible temporal error associated with the numerical integration. However, for practical applications employing high-order DG methods, this may be suboptimal or computationally prohibitive.

Let h be the smallest possible diameter of grid element Ω_{ij}. LeSaint and Raviart [44] have proved that the convergence order $\mathcal{O}(h^N)$ on general grids and $\mathcal{O}(h^{N+1})$ on Cartesian grids for the steady state conservation law. Various numerical experiments show that, in general, a P^N-DG method can achieve $\mathcal{O}(h^{N+1})$ order of convergence. However, the CFL condition for RK-DG methods is much more stringent. For a system of conservation laws,

$$\frac{\partial U}{\partial t} + \nabla \cdot F(U) = S(U), \tag{2.17}$$

the CFL condition for P^N-DG methods is available based on numerical experiments [14]

$$\frac{c\Delta t}{h} \leq \frac{1}{2N+1} \tag{2.18}$$

where c is maximum speed of the system. In general, the CFL condition is limited by the minimum grid spacing, and in the NH regime, due to the large aspect ratio between horizontal and vertical grid spacing, the minimum grid spacing would be the vertical resolution, which is usually several orders smaller than the horizontal resolution. The maximum allowed time step size of the explicit time integration schemes would make the long-term simulation computationally ineffective. The design of the time integration schemes needs relax the strict CFL condition to permit a reasonable time-step size. It is also desired that the chosen time integration schemes do not introduce excessive additional communication overhead to the existing HOMME framework and the resulting NH models can still achieve nearly optimal scalability on massive parallel machines.

Chapter 3

Horizontal Aspect: Shallow-water System

Several forms of equation sets are available to characterize the idealized NH air flow. We would like to determine the most suitable form of the equation sets in the NH regime. The performance of different forms of the equation sets in terms of conserving integral invariants will be of particular interest. To answer this question, the global Shallow water framework will be used as it contains the horizontal operators found in the full 3D global NH models and can be simulated as a cheaper computational cost. The global shallow water framework is usually the starting point to construct a numerical framework for full global atmospheric models. In addition, several numerical aspects for the horizontal component of the full 3D model will be explored in this chapter, such as the grid system and artificial viscosity to stabilize the flow field.

3.1 Shallow-water equations on the rotating sphere

The system of SWEs consists of the continuity and momentum equations. The continuity equation is accountable for the conservation of mass, and is formulated as follows,

$$\frac{\partial h}{\partial t} + \nabla \cdot (h\mathbf{v}) = 0. \tag{3.1}$$

Usually, the momentum equations are written in vector form [95]. In the context of numerical modeling, two forms of momentum equations are widely used. They are the conservative form (3.2)

and the vector-invariant form (3.3),

$$\frac{\partial h\mathbf{v}}{\partial t} + \nabla \cdot (\mathbf{v}h\mathbf{v} + \frac{1}{2}gh^2\mathbf{I}) = -f\hat{\mathbf{k}} \times h\mathbf{v} - gh\nabla h_s, \tag{3.2}$$

$$\frac{\partial \mathbf{v}}{\partial t} + \nabla(\frac{\mathbf{v} \cdot \mathbf{v}}{2}) = -(\zeta + f)\hat{\mathbf{k}} \cdot \mathbf{v} - \nabla\Phi. \tag{3.3}$$

Here, h is the depth of the fluid above the solid surface, h_s is the height of the bottom topography, which may be a river bed or an underlying mountain. $\mathbf{v}$ is the horizontal wind vector, f is the Coriolis parameter, $\hat{\mathbf{k}}$ is the unit vector along the outward radial direction, and $\mathbf{I}$ is the 2×2 identity matrix. $\Phi = g(h_s + h)$ is the geopotential height at the free surface of the fluid (above sea level). $\zeta = \hat{\mathbf{k}} \cdot (\nabla \times \mathbf{v})$ denotes the relative vorticity. Note that, divergence $(\nabla\cdot)$ and gradient (∇) operators are defined in general cases. In other words, they are not specific to a particular grid system.

The flux-form of SWEs consists of (3.1) and (3.2), while the vector-invariant form of SWEs is composed of (3.1) and (3.3). In the continuous sense, both forms are mathematically equivalent for smooth waves, while in the discrete settings, they are not identical and they have their own focuses. For the flux-form, the rigorous form of momentum appears in the momentum equations. It states the conservation of momentum physically. The state variables for the momentum equations in the conservative form and the vector-invariant form are $h\mathbf{v}$ and $\mathbf{v}$, respectively. The advantage of choosing $h\mathbf{v}$ as a prognostic variable is that, if letting $h \to 0$, the prognostic variable goes to zero as long as $\mathbf{v}$ stays bounded. Note that $h \to 0$ corresponds to a massless layer in numerical modeling. By employing the conservative form of momentum equations, the discrete system is still well-behaved even we evacuate the mass of a given layer [66].

Moreover, since (3.3) expresses the conservation of particle velocity $\mathbf{v}$, which is physically meaningless, the vector-invariant form is, in some sense, mathematically conservative but not physically conservative [88]. In the presence of shock waves, the two forms can lead to two different solutions. The flux-form tends to be a better shock capturing method, whereas numerical solution from vector-invariant form will still produce shocks but with wrong propagation speed, even employing conservative numerical methods [88].

On the other hand, the vector-invariant form is a popular choice in climate modeling. It is

very difficult to find the shortcomings of this form in numerical computing [66]. In addition, if we take $\nabla\times$ of momentum equation (3.3), we can immediately obtain a vorticity equation while the same manipulation on (3.2) does not. In other words, discrete systems based on the conservative form of the momentum equation (3.2) do not guarantee the conservation of vorticity. Every term in (3.2) tends to introduce spurious vorticity into the system [66]. If no treatment is applied to suppress the noise, the flux-form may eventually produce an inaccurate and unacceptable numerical solution [66].

3.1.1 SWEs on the cubed-sphere

Two forms of SWEs on the cubed-sphere are expressed in the curvilinear equiangular (x^1, x^2) coordinate system.

3.1.1.1 Flux-form of SWEs on the cubed-sphere

In the curvilinear coordinates generated by cubed-sphere geometry, the flux-form of SWEs can be written in terms of contravariant components [68] as follows,

$$\frac{\partial}{\partial t}\begin{bmatrix} h \\ hu^1 \\ hu^2 \end{bmatrix} + \frac{1}{\sqrt{G}}\frac{\partial}{\partial x^1}\begin{bmatrix} \sqrt{G}hu^1 \\ \sqrt{G}\tau^{11} \\ \sqrt{G}\tau^{21} \end{bmatrix} + \frac{1}{\sqrt{G}}\frac{\partial}{\partial x^2}\begin{bmatrix} \sqrt{G}hu^2 \\ \sqrt{G}\tau^{12} \\ \sqrt{G}\tau^{22} \end{bmatrix} = \Phi_C + \Phi_T + \begin{bmatrix} 0 \\ -\Gamma^1_{ij}\tau^{ji} \\ -\Gamma^2_{ij}\tau^{ji} \end{bmatrix}. \quad (3.4)$$

where the tensor $\tau^{ij} = hu^i u^j + 1/2gh^2G^{ij}$, with $i, j, k \in \{1, 2\}$.

The last term on the right hand side of (4) can be viewed as the source term due to the curvature of the chosen coordinate system. Here, the Christoffel symbols Γ^k_{ij} are needed to define the differential operators of contravariant vectors in curvilinear coordinates [68, 98], noting that under the gnomonic mapping $G^{ij}\Gamma^k_{ij} = 0$ [92]:

$$\Gamma^1_{11} = \frac{2\tan x^1 \tan^2 x^2}{1+\tan^2 x^1+\tan^2 x^2},\ \Gamma^1_{12} = -\frac{\tan x^2 \sec^2 x^2}{1+\tan^2 x^1+\tan^2 x^2},\ \Gamma^1_{22} = 0,$$

$$\Gamma^2_{22} = \frac{2\tan^2 x^1 \tan x^2}{1+\tan^2 x^1+\tan^2 x^2},\ \Gamma^2_{12} = -\frac{\tan x^1 \sec^2 x^1}{1+\tan^2 x^1+\tan^2 x^2},\ \Gamma^2_{11} = 0.$$

Φ_C and Φ_T denote the source term due to Coriolis force and the source term due to bottom topography, respectively,

$$\Phi_C = -\begin{bmatrix} 0 \\ f\sqrt{G}(G^{12}hu^1 - G^{11}hu^2) \\ f\sqrt{G}(G^{22}hu^1 - G^{12}hu^2) \end{bmatrix}, \tag{3.5}$$

$$\Phi_T = -\begin{bmatrix} 0 \\ gh(G^{11}\frac{\partial h_s}{\partial x^1} + G^{12}\frac{\partial h_s}{\partial x^2}) \\ gh(G^{12}\frac{\partial h_s}{\partial x^1} + G^{22}\frac{\partial h_s}{\partial x^2}) \end{bmatrix}. \tag{3.6}$$

3.1.1.2 Vector-invariant form of SWEs on the cubed-sphere

The vector-invariant form of SWEs is cast in terms of covariant components, which is in the following simple form [59],

$$\frac{\partial}{\partial t}\begin{bmatrix} \sqrt{G}h \\ u_1 \\ u_2 \end{bmatrix} + \frac{\partial}{\partial x^1}\begin{bmatrix} \sqrt{G}hu^1 \\ E \\ 0 \end{bmatrix} + \frac{\partial}{\partial x^2}\begin{bmatrix} \sqrt{G}hu^2 \\ 0 \\ E \end{bmatrix} = \begin{bmatrix} 0 \\ \sqrt{G}u^2(f+\zeta) \\ -\sqrt{G}u^1(f+\zeta) \end{bmatrix}. \tag{3.7}$$

The energy term E and relative vorticity ζ on $\mathbf{S}$ are defined as

$$E = \Phi + \frac{1}{2}(u_1u^1 + u_2u^2), \tag{3.8}$$

$$\zeta = \frac{1}{\sqrt{G}}\left[\frac{\partial u_2}{\partial x^1} - \frac{\partial u_1}{\partial x^2}\right]. \tag{3.9}$$

Note that for the vector-invariant form, the fluxes used are the energy fluxes not the momentum fluxes.

Both (3.4) and (3.7) can be generalized in the following compact form:

$$\frac{\partial}{\partial t}\mathbf{U} + \frac{\partial}{\partial x^1}\mathbf{F_1}(\mathbf{U}) + \frac{\partial}{\partial x^2}\mathbf{F_2}(\mathbf{U}) = \mathbf{S}(\mathbf{U}). \tag{3.10}$$

3.1.2 DG spatial discretization to SWEs on the cubed-sphere grid

Let the computational domain $\mathbf{D}$ be the surface of the inscribed (logical) cube $\mathbf{C}$, which consists of six identical non-overlapping patches, i.e. $\mathbf{D} = \cup_{p=1}^{6}\Omega^p$. The discretization for each patch is identical and thus we only consider the discretization for a single face, denoted by Ω. The square subdomain Ω is divided into $N_e \times N_e$ non-overlapping rectangular elements Ω_{ij} such that,

$$\Omega_{ij} = [(x^1, x^2)|x^1 \in (x^1_{i-1/2}, x^1_{i+1/2}), x^2 \in (x^2_{j-1/2}, x^2_{j+1/2})], \text{ where } i, j = 1, 2, \ldots, N_e.$$

So, $M = 6N_e^2$ elements in total which span the whole spherical domain $\mathbf{S}$. There are $N_v \times N_v$ GLL points on Ω_R, and the total degrees of freedom on $\mathbf{D}$ are $6N_e^2N_v^2$ with this configuration.

For the numerical flux, α is identical for both flux-form and vector-invariant form of SWEs. The formulations of α in x^1 and x^2 directions are given by (detailed deriviation can be found in [59]),

$$\begin{aligned}\alpha|_{x^1} &= \max\{|u^1| + \sqrt{G^{11}gh}\},\\ \alpha|_{x^2} &= \max\{|u^2| + \sqrt{G^{22}gh}\}.\end{aligned} \tag{3.11}$$

Similar to the idea of [58], we introduce a uniform second-order diffusion to the flux form of SWEs. The viscous SW model can be written in a compact form as follows:

$$\frac{\partial}{\partial t}\mathbf{U} + \nabla \cdot \mathbf{F}(\mathbf{U}) = \mathbf{S}(\mathbf{U}) + \mathbf{D}(\mathbf{U}). \tag{3.12}$$

The viscous flux $\mathbf{D}(\mathbf{U})$ is expressed as:

$$\mathbf{D}(\mathbf{U}) = \begin{bmatrix} 0 \\ \nu\sqrt{G}\nabla_s \cdot (h\nabla_s u^1) \\ \nu\sqrt{G}\nabla_s \cdot (h\nabla_s u^2) \end{bmatrix},$$

where $\nabla_s = (\mathbf{a^1}\partial/\partial x^1, \mathbf{a^2}\partial/\partial x^2)$.

$$\sqrt{G}\nabla_s \cdot (h\nabla_s u^i) = \frac{\partial}{\partial x^1}\left[h\sqrt{G}G^{11}\frac{\partial u^i}{\partial x^1} + h\sqrt{G}G^{12}\frac{\partial u^i}{\partial x^2}\right] + \frac{\partial}{\partial x^2}\left[h\sqrt{G}G^{21}\frac{\partial u^i}{\partial x^1} + h\sqrt{G}G^{22}\frac{\partial u^i}{\partial x^2}\right],$$

where $i \in \{1, 2\}$, and ν is the constant diffusion coefficient. Therefore, the auxiliary variables $\tilde{\mathbf{q}}$ should be modified correspondingly,

$$\mathbf{q} = \left[\frac{\partial U}{\partial x^1}, \frac{\partial U}{\partial x^2}\right], \mathbf{M} = \begin{bmatrix} \sqrt{G}G^{11} & \sqrt{G}G^{12} \\ \sqrt{G}G^{21} & \sqrt{G}G^{22} \end{bmatrix}, \text{ and } \tilde{\mathbf{q}} = h\,\mathbf{q}\,\mathbf{M}^T.$$

Note that, in the curvilinear coordinates, the vector Laplacian has a different formulation from the Laplacian of the components. Curvilinear vector Laplacian has a complex form and is computationally expensive. However, for simplicity, the Laplacian is treated component wise for each momentum equation.

The bottom topography function h_s is also projected into the same space $\mathcal{V}_h$ and is defined to be

$$h_s(\xi^1, \xi^2) = \sum_{m=0}^{N} \sum_{n=0}^{N} h_s(\xi_m^1, \xi_n^2) h_m(\xi^1) h_n(\xi^2). \tag{3.13}$$

The discretization of the source term bottom topography Φ_T requires special treatment and is discussed in Section 3.1.3 in detail.

3.1.3 Discretization of source term due to bottom topography

Bermudez and Vazquez [8] proposed the idea of the "exact C-property", which stands for the ability of the numerical scheme to exactly preserve the steady-state equilibrium solution for the still water at rest:

$$\mathbf{v} = 0, \text{ and } H = h + h_s = \text{constant}. \tag{3.14}$$

The numerical approaches which satisfy "exact C-property" are often referred as the well-balanced methods. When a non-smooth bottom topography is present in the flux-form of SWEs (3.4), the spatial discretization must obey the well-balanced property to avoid spurious oscillations into the flow near the non-smooth region of the bottom topography. For non-smoothness, we refer to non-differentiable function, which can also be discontinuous. The traditional DG method (**??**) is well-balanced for smooth bottom topography but not for the non-smooth bottom topography [96]. Well-balanced DG schemes for the SWEs are an active research area and a detailed discussion can

be found in [60]. As observed in [96], a small modification on the flux term can make the traditional DG scheme well-balanced. Inspired by [96, 97], we consider a well-balanced DG scheme for our flux-form SW model with a minor change in the flux term.

We define the numerical flux as $\tilde{\mathbf{F}}(\mathbf{U_h})$, and the modification in the flux term is carried out in the following steps:

- After computing the boundary value of $U_h|_{\Gamma_e}$, define:

$$h^{*,\pm}|_{\Gamma_e} = H^{\pm}|_{\Gamma_e} - \max\left(h_s^+|_{\Gamma_e}, h_s^-|_{\Gamma_e}\right) \tag{3.15}$$

- Modify the prognostic variable $\mathbf{U}$ along the boundary Γ_e:

$$U_h^{*,\pm}|_{\Gamma_e} = \begin{bmatrix} h^{*,\pm} \\ h^{*,\pm}\, u^{1,\pm} \\ h^{*,\pm}\, u^{2,\pm} \end{bmatrix}_{\Gamma_e}. \tag{3.16}$$

- Define the notations:

$$\delta^*_{x^1} = \begin{bmatrix} 0 \\ G^{11}[\frac{g}{2}(h^-)^2 - \frac{g}{2}(h^{*,-})^2] \\ G^{21}[\frac{g}{2}(h^-)^2 - \frac{g}{2}(h^{*,-})^2] \end{bmatrix}_{\Gamma_e}, \; \delta^*_{x^2} = \begin{bmatrix} 0 \\ G^{12}[\frac{g}{2}(h^-)^2 - \frac{g}{2}(h^{*,-})^2] \\ G^{22}[\frac{g}{2}(h^-)^2 - \frac{g}{2}(h^{*,-})^2] \end{bmatrix}_{\Gamma_e},$$

  where $\delta^*_{x^1}$ and $\delta^*_{x^2}$ may be interpreted as the hydrostatic reconstruction under the curvilinear coordinate system.

  Thus, we give the new well-balanced numerical flux:

$$\tilde{\mathbf{F}}(U_h) = \hat{\mathbf{F}}(U_h^*) + \boldsymbol{\delta} \cdot \mathbf{n}, \tag{3.17}$$

  where $\boldsymbol{\delta} = (\delta^*_{x^1}, \delta^*_{x^2})$. As shown in [96], the resulting scheme is $(N+1)$-order convergence in space and converges to the weak solution.

In order to capture the non-smoothness of the bottom topography in the simulation, the initial solution is computed from the modal expression of h_s at the $N_v \times N_v$ Gauss-Legendre (GL)

points, and then interpolating it on to the corresponding GLL points. In the interpolation process, we only keep the 0-th order term, and the higher order terms are dropped in the GL quadrature.

Note that, if the bottom topography is flat or smooth, the well-balanced numerical flux is equivalent to the original numerical flux. In other words, for smooth bottom topography, the traditional DG scheme is already well-balanced. The well-balanced correction in the flux term only takes effect when there is a non-smooth bottom topography [96].

3.2 Numerical experiments and results

To test the accuracy and the performance of our flux-form DG SW models (**??**, 2.15), we consider three standard test-cases here. They are the steady-state geostropic flow, the zonal flow over an isolated mountain as suggested in Williamson et al. [95], and the barotropic instability proposed by Galewsky et al. [22]. The first two test-cases are often referred as the SW test-case 2 and 5, respectively [95]. Comparisons of two forms of inviscid DG SW models using these test-cases are shown, and the conservation of global invariants are monitored as a function of time.

In order to compare the resolution of cubed-sphere grids associated with GLL points with that of the regular latitude-longitude grid, we use an "average" resolution at the equator of the sphere [52]:

$$\text{approximate resolution} = \triangle\hbar = \frac{90^\circ}{N_e(N_v - 1)} = \frac{90^\circ}{N_e N}.$$

For most of the test-cases considered, the analytic solution is unknown. When the analytic solution is not available, a reference solution is chosen to be the numerical result produced by the inviscid vector-invariant SW model at the same resolution. In terms of the convergence studies of inviscid flux-form of SWEs, we measure the L_1, L_2 and L_∞ errors of the approximate solution, as suggested in [95]. For the convergence behavior, when including the diffusion effect, we use only the L_1 error of the simulated solution, because the other two have similar convergence performances.

In order to monitor the numerical conservation of the global invariants, we define the nor-

malized integral $\bar{\Psi}(t)$ as:

$$\bar{\Psi}(t) = \frac{I_g[\Psi(\lambda,\theta,t)] - I_g[\Psi(\lambda,\theta,0)]}{I_g[\Psi(\lambda,\theta,0)]}, \tag{3.18}$$

where I_g is the global surface integral. I_g is evaluated on the cubed-sphere by GLL quadrature rule as follows:

$$I_g(\Psi(\lambda,\theta,t)) \approx \sum_{p=1}^{6}\sum_{k=1}^{N_e}\sum_{l=1}^{N_e}\sum_{i=1}^{N_v}\sum_{j=1}^{N_v}\sqrt{G_{ijkl}}\,\Psi_p(x^1_{i,k,l}, x^2_{j,k,l}, t)w_i w_j,$$

where p indicates the panel index.

For the conservation of mass, $\Psi = h$, and for the conservation of total energy, $\Psi = \{h(u^2 + v^2) + g[(h+h_s)^2 - h_s^2]\}/2$. For the conservation of potential enstrophy, $\Psi = (\zeta + f)^2/(2h)$, where ζ is defined in (3.9). For the conservation of zonal angular momentum, $\Psi = (u + \omega R\cos\theta)R\cos\theta$ (for thin atmosphere [73]), where ω is the angular velocity. Time traces of these integral invariants are shown for the comparison of different numerical experiments.

Note that, the SSP-RK time integration schemes impose a stringent CFL stability restriction for the DG discretizations. The presence of the diffusion terms further confine the explicit time-step size [58]. Besides, in order to carry out a fair comparison of the two sets of SWEs, it would be beneficial to avoid possible temporal errors. Due to these facts, we choose a moderate time stepping which is suboptimal. It is well-known that the communication expenses are the major limiting factor for parallel efficiency [46]. The extra cost of the flux calculations in the LDG scheme (2.11) is time-consuming and reduces the scalability [58]. We test two options: one is to update diffusion terms in every stage of SSP-RK3 (2.16), and the other is to compute it at the beginning of (2.16) and use the same value of diffusion terms for every inner stage of (2.16). For small $\triangle t$, numerical results show that there is no significant difference in the quality of solutions between these two choices, while the latter one is more efficient than the former one. We should emphasize that, the second treatment of the diffusion terms may not apply to general cases with relatively large $\triangle t$. The motivation for us to consider this setup is simplicity and efficiency. Therefore, in the numerical experiments, we adopt the second option for the LDG diffusion process.

The physical parameters used in the numerical tests are: radius of Earth $R = 6.37122 \times$

$10^6\,m$, angular velocity of Earth $\omega = 7.292 \times 10^{-5}\,rad\,s^{-1}$, and gravitational acceleration $g = 9.80616\ m\,s^{-2}$.

3.2.1 Geostrophic flow

The first test is SW test-case 2, which describes a zonal geostrophic balanced flow [95]. It is a steady-state test for the global SWEs with a uniform wind field. The initial (also analytic) geopotential and the velocity are given as,

$$gh = gh_0 - \frac{u_0}{2}(2R\omega + u_0) \times (\sin\theta\cos\alpha_0 - \cos\lambda\cos\theta\sin\alpha_0)^2, \tag{3.19}$$

$$u = u_0(\cos\alpha_0\cos\theta + \sin\alpha_0\cos\lambda\sin\theta), \tag{3.20}$$

$$v = -u_0\sin\alpha_0\sin\lambda, \tag{3.21}$$

where $u_0 = 2\pi R/(12 \text{ days})$, $gh_0 = 2.94 \times 10^4 m^2 s^{-2}$ and α_0 is the flow orientation angle.

It is a challenging test for the cubed-sphere geometry when α_0 is set to be $\pi/4$. Since the analytic solution is known, SW test-case 2 is usually used for validating the accuracy and studying the convergence of the numerical models. Williamson et al. [95] suggested at least 5 model days of time integration for this test. Therefore, SW models considered here are integrated for 5 model days with time step size $\triangle t = 90\,s$, for all the experiments, regardless of the resolution. The resolution for the calculation is chosen as $N_e = 12, N = 3$, which corresponds to approximately 2.5° at the equator.

3.2.1.1 DG for flux-form inviscid SWEs

The initial condition is shown in Fig. (3.1a). Relative errors of the height difference field for two forms of SWEs are displayed in Fig. (3.1b) and (3.1c). The maximum relative errors are $O(10^{-6})$ for both forms. As seen from Fig. (3.1b) and (3.1c), the height field in the vector-invariant form is less noisy than that of the flux-form.

To get the notion of the numerical convergence of our flux-form SW model (3.4), we organize the experiments in two ways. Firstly, we fix $N_e = 3$ and increase the order of polynomial N from

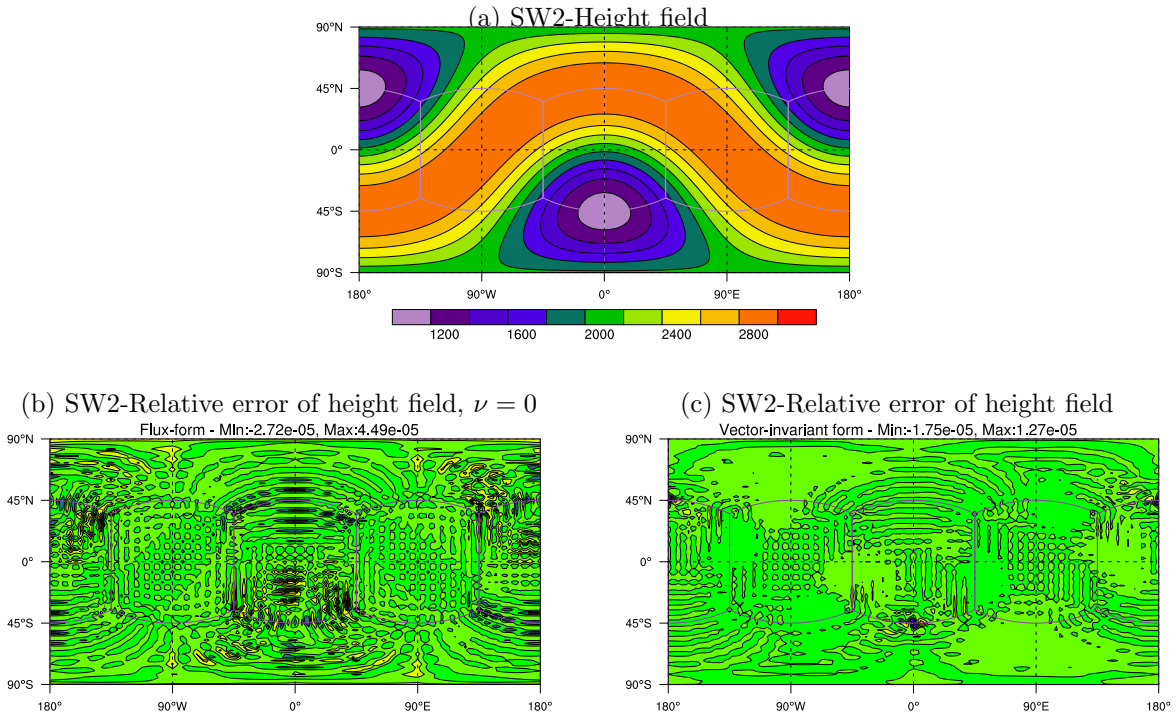

Figure 3.1: The geostrophic flow (SW test-case 2) in the resolution $\approx 2.5°$ at the equator ($N_e = 12, N = 3$) and $\triangle t = 90\,s$. (a) is the reference solution. Relative errors of height field at day 5 are shown in (b) for the flux-form of SWEs and (c) for the vector-invariant form. The contour varies from -3×10^{-5} to 4×10^{-5} with an increment of 5×10^{-6}.

4 to 10. The results are shown in Fig. (3.2a), which shows an exponential convergence. Then, we perform an $h-$convergence study, by varying N_e from 5 to 15 with a fixed order of polynomial $N = 3$, and it is displayed in Fig. (3.2b). It is observed that the nodal DG scheme attains at least 4-th order convergence. Both $p-$convergence and $h-$convergence performances are similar to those of the vector-invariant form [59].

Time traces of normalized errors of the global invariants are shown in Fig. 3.3. The results from the vector-invariant form are also displayed for reference and comparison. We can see that both forms preserve mass to the machine precision. The flux-form tends to have better conservation of total energy, while the vector-invariant form has a nicer control of potential enstrophy. This is consistent with the potential weakness of the flux-form of SWEs discussed in Section 3.1. However, for both sets of SWEs, the potential enstrophy is conserved up to a small constant at the same

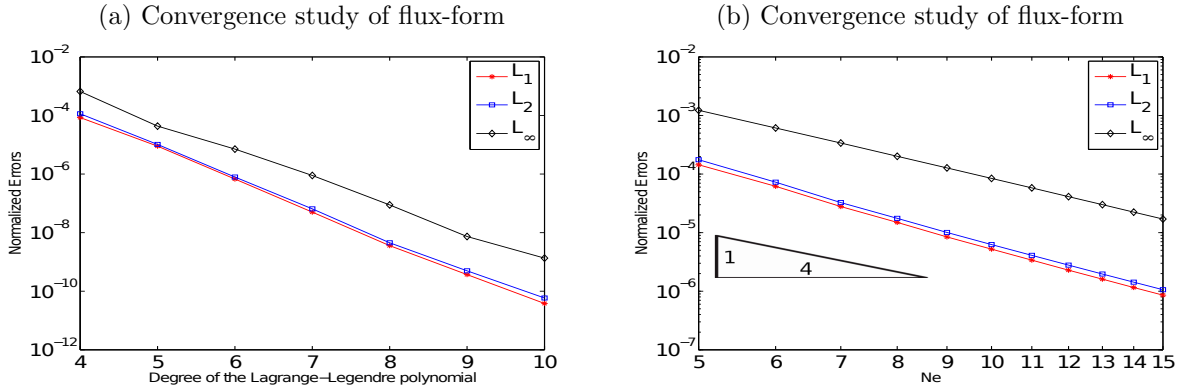

Figure 3.2: Normalized errors of the height field for the geostrophic flow (SW test-case 2) at day 5 for the inviscid flux-form SW model. (a) is computed with $N_e = 3$ and varying N from 4 to 10. (b) is computed with $N = 3$ and varying N_e from 5 to 15.

order.

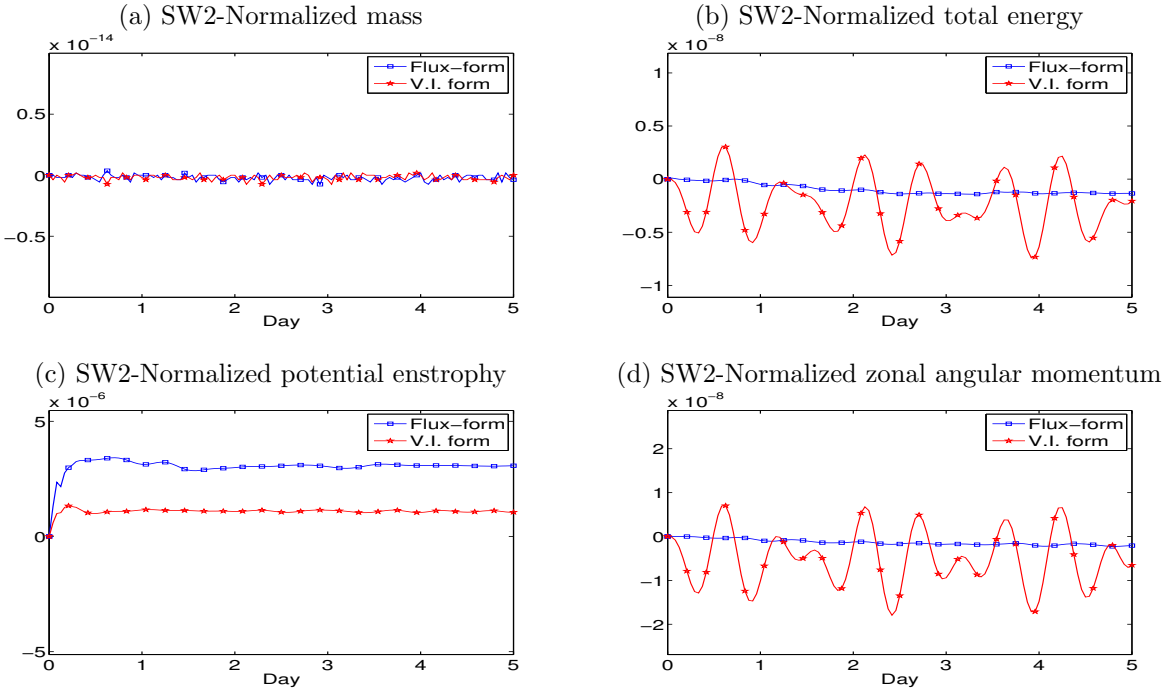

Figure 3.3: Time traces of normalized errors of mass (a), total energy (b), potential enstrophy (c) and zonal angular momentum (d) of the flux-form and the vector-invariant form for the geostrophic flow (SW test-case 2) in the resolution $\approx 2.5^\circ$ at the equator ($N_e = 12, N = 3$). Both tests are integrated for 5 days with $\triangle t = 90\,s$.

3.2.1.2 LDG for viscous flux-form of SWEs

As discussed in Section 2.2.2, a convergence study of the flux-form SWEs with artificial diffusion, namely as $\triangle\hbar \to 0$, $\nu \to 0$, is not feasible, given the fact that neither the analytic solution for viscous SWEs nor a rigorous choice of ν is available. Therefore, we demonstrate the influence of the artificial diffusion by showing how the diffused solution deviates from the non-diffused solution. This is achieved by keeping ν fixed and varying the resolution.

Fig. 3.4 shows the normalized L_1 errors of the height field with various choices of the diffusion coefficients ν when refining the grid resolution. Fig. (3.4a) displays the L_1 errors of the height field at day 5 when $N_e = 3$, and N varies from 4 to 10. As we increase the resolution, the non-diffused version exhibits an exponential convergence to the exact solution, while the LDG solution evolves to a "diffused state", which depends on the magnitude of the diffusion coefficient ν. Similar trends can be found in Fig. (3.4b), which shows the normalized L_1 errors of the height field at day 5 when $N = 3$ and N_e varies from 5 to 15. The results in Fig. 3.4 reveal that when a stronger numerical diffusion is added, the diffused solution reaches a "diffused equilibrium" at a lower resolution. The "diffused equilibrium" corresponds to the flattened lines in Fig. (3.4a). This implies that the diffusion effect becomes dominant, and as a result, the fine physical features due to the high-order nature of the solution are smeared or erased when a stronger numerical diffusion is used. Comparing Fig. (3.4a) and (3.4b), the magnitude of the diffusion coefficient plays a predominant role on the evolution of the viscous solution over the resolution or the polynomial degree.

To study the influence of the diffusion effect on the effectiveness of the scheme in conserving global invariants, time traces of the normalized errors are exhibited in Fig. 3.5. For all the global invariants considered here, the normalized errors grow at a higher rate when increasing the strength of the diffusion effect. The convergence behaviors of the viscous flux-form SWEs are similar to those of viscous vector-invariant form [58].

(a) Evolution trend of LDG Flux-form of SW2

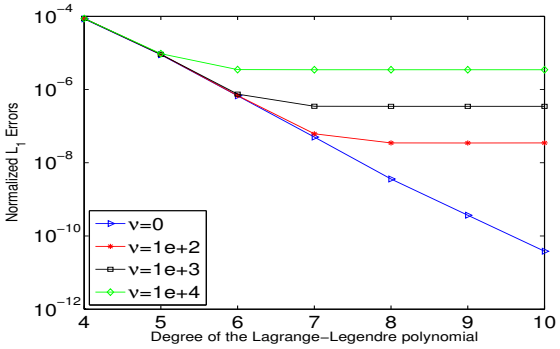

(b) Evolution trend of LDG Flux-form of SW2

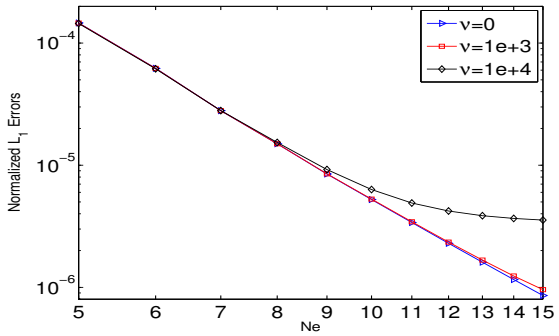

Figure 3.4: Normalized L_1 errors in the height field for SW test-case 2 at day 5 for flux-form of SWEs with diffusion for $\nu = 0$, $\nu = 10^2\, m^2 s^{-1}, \nu = 10^3\, m^2 s^{-1}, \nu = 10^4\, m^2 s^{-1}$ respectively. (a) is computed with $N_e = 3$ and varying N from 4 to 10. (b) is computed with $N = 3$ and varying N_e from 5 to 15.

(a) SW2-Normalized mass

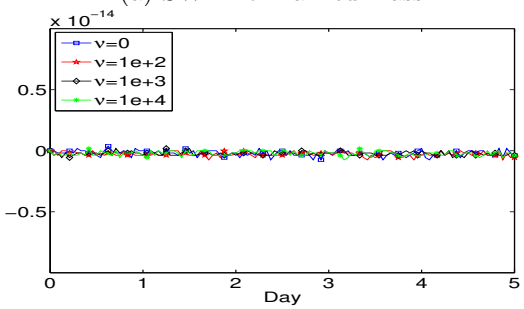

(b) SW2-Normalized total energy

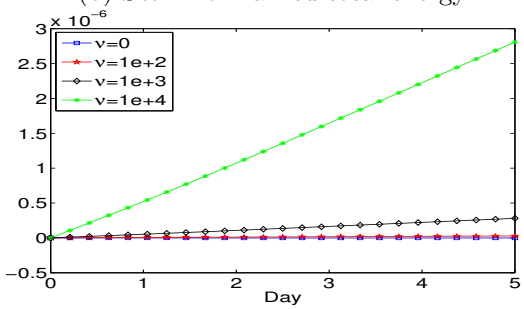

(c) SW2-Normalized potential enstrophy

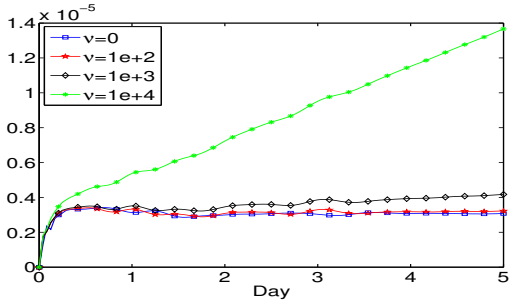

(d) SW2-Normalized zonal angular momentum

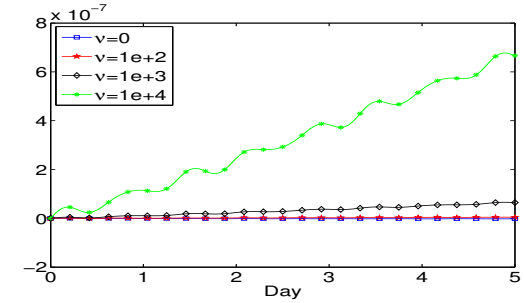

Figure 3.5: Time traces of the normalized errors of mass (a), total energy (b), potential enstrophy (c) and zonal angular momentum (d) of viscous flux-form SWEs for the geostrophic flow (SW test-case 2) in the resolution $\approx 2.5^\circ$ at the equator ($N_e = 12, N = 3$). The diffusion coefficient varies from $\nu(\, m^2 s^{-1}) = 0, 10^2, 10^3, 10^4$. All tests are integrated for 5 days with $\triangle t = 90\, s$

3.2.2 Barotropic instability (Galewsky test)

The barotropic instability test of [22] simulates a midlatitude jet generated by adding a small amount of perturbation to the barotropic balanced flow. This test is particularly challenging on the cubed-sphere grid, because the barotropic instability activities are presented at the discontinuous edges of the top panel of cubed-sphere grid, as observed by St-Cyr et al. [81]. A 6-day time integration is recommended for this test both for with and without diffusion. We are particularly interested in the relative vorticity field for this test-case. As shown in [81], nice features of the vorticity fields can be captured at a resolution higher than 1.25°.

For this experiment, we choose the grid resolution at $N_e = 30, N = 7$, which is approximately 0.43° at the equator. We choose the time step size $\triangle t = 5\,s$ for all the simulated runs, which is suboptimal, and integrate the model for 6 model days.

The relative vorticity fields at day 6 are shown in Fig. 3.6 for the inviscid and viscid flux-form of the SWEs. Fig. (3.6a) shows the inviscid run and it can be seen that the non-diffused flux-form is able to well capture the dynamics and the solution is smooth and comparable to that in [22, 58]. Usually, high-order methods, such as RBF [20], require strong diffusion to stabilize the result for this test-case. From various numerical experiments, we observe that the inviscid flux-form can produce a smooth relative vorticity field as long as the grid resolution is greater than 0.5°. However, the vector-invariant form without diffusion is very sensitive to the resolution parameters N_e, N.

In order to consider the diffusion effect, Fig. (3.6b), (3.6c) show the viscous tests with the diffusion coefficients ν $(m^2 s^{-1})$ equals to 10^4 and 10^5 respectively. The viscid version successfully eliminates the small-scale noise appearing in Fig. (3.6a) with a proper choice of diffusion coefficient value ν (here, $\nu = 10^4$ for instance). However, here the choice of the diffusion coefficient is heuristic, and somewhat arbitrary.

Time traces of the normalized errors of conservative integrals are shown in Fig. 3.7 with the diffusive effect. Similar to SW test-case 2, the error growth is at a noticeable faster rate and is strongly influenced by the magnitude of the value of ν.

(a) Barotropic instability-Day 6: Flux-form, $\nu = 0$

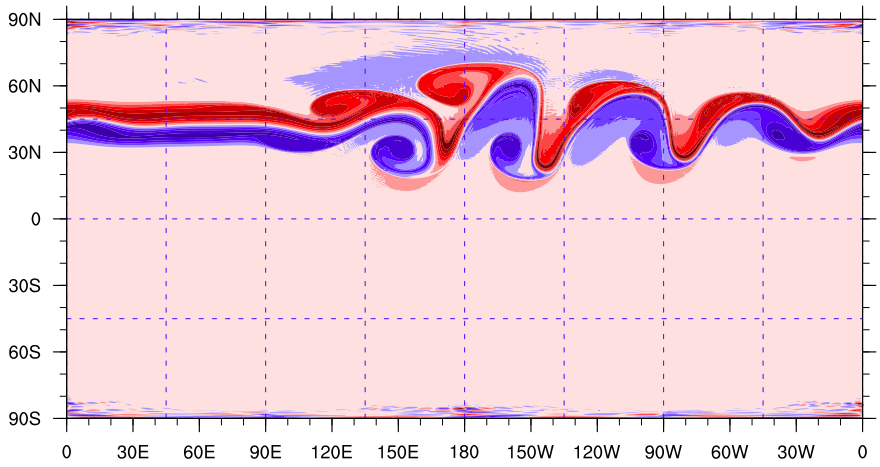

(b) Barotropic instability-Day 6: Flux-form, $\nu = 10^4$

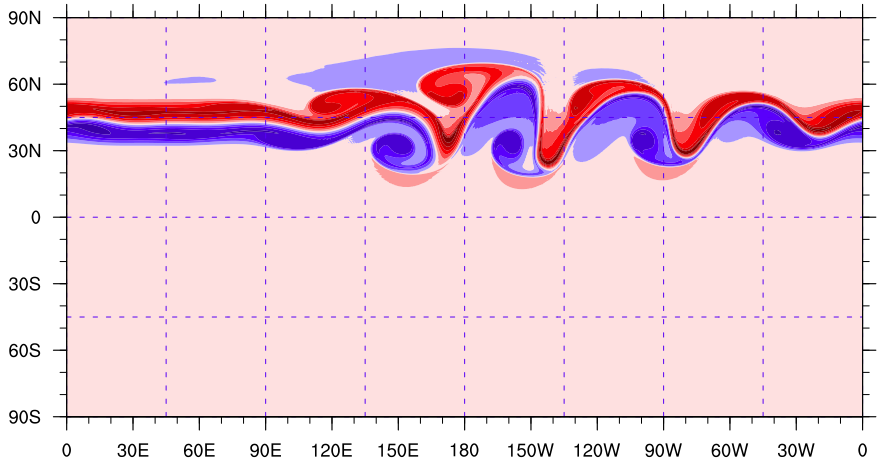

(c) Barotropic instability-Day 6: Flux-form, $\nu = 10^5$

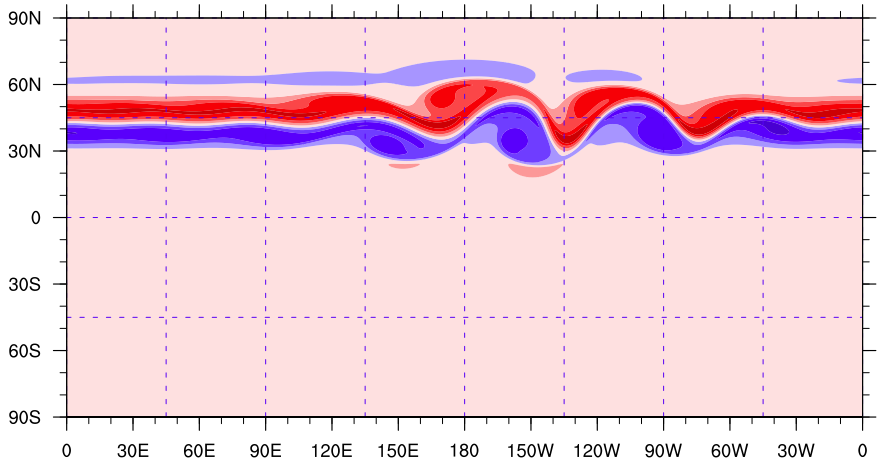

Figure 3.6: Relative vorticity field of the barotropic instability test at day 6 in the resolution $\approx 0.43°$ at the equator ($N_e = 30, N = 7$). (a) is using the inviscid flux-form. (b) is using the LDG flux-form with $\nu = 10^4\, m^2 s^{-1}$. (c) is using the LDG flux-form with $\nu = 10^5\, m^2 s^{-1}$. $\triangle t = 5\, s$ for all runs. The contour varies from $-1.1 \times 10^{-4}\, s^{-1}$ to $1.1 \times 10^{-4}\, s^{-1}$ with an increment of $2 \times 10^{-5}\, s^{-1}$.

(a) Barotropic instability-Normalized mass

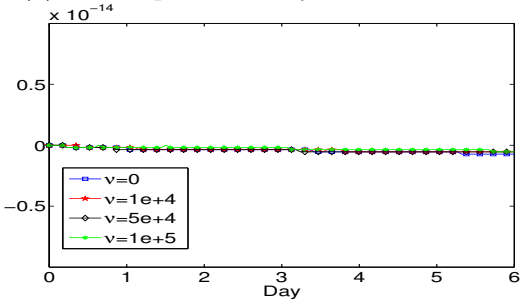

(b) Barotropic instability-Normalized total energy

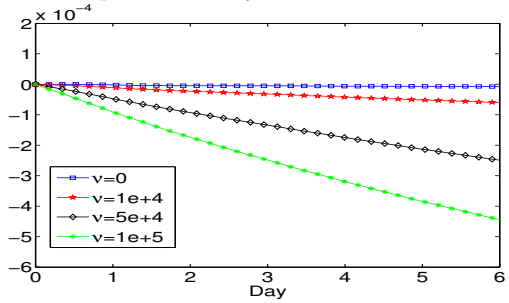

(c) Barotropic instability-Normalized potential enstrophy

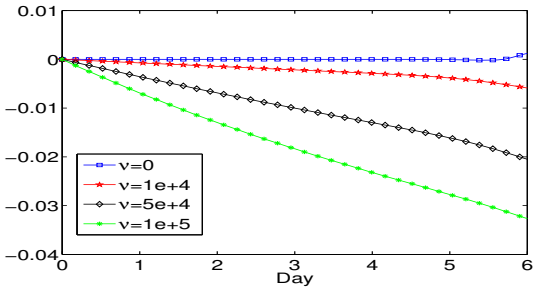

(d) Barotropic instability-Normalized zonal angular momentum

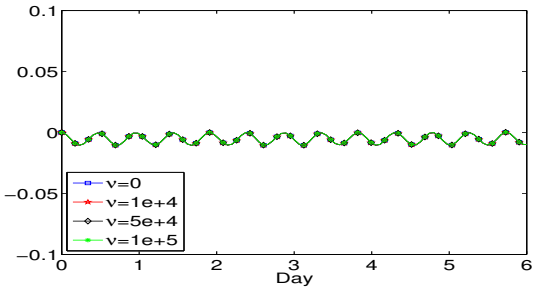

Figure 3.7: Time traces of the normalized errors of mass (a), total energy (b), potential enstrophy (c) and zonal angular momentum (d) of LDG flux-form SW model for the barotropic instability test-case in the resolution $\approx 1.5^\circ$ at the equator ($N_e = 30, N = 7$). The diffusion coefficient ν ($m^2\, s^{-1}$) varies from $0, 10^4, 5 \times 10^4, 10^5$. The tests are integrated for 6 days with $\triangle t = 5\, s$.

3.2.3 Zonal flow over an isolated mountain

The last test-case we consider in this study is the SW test-case 5 in [95]. This test-case describes a zonal flow over an isolated *mountain*. It is the only test considered here in which the bottom topography is non-flat. The bottom topography is a conical mountain centered at $(\lambda_c, \theta_c) = (3\pi/2, \pi/6)$, which is also non-smooth. So, the well-balanced DG scheme takes effect on this test-case. The initial wind field and height field are identical to the SW test-case 2, except that $\alpha_0 = 0, h_0 = 5960\, m$ and $u_0 = 20\, m/s$. The underlying mountain is defined as:

$$h_s = h_s^0(1 - \frac{r}{a}) \tag{3.22}$$

where $h_s^0 = 2000\, m, a = \pi/9$, and $r^2 = \min[a^2, (\lambda - \lambda_c)^2 + (\theta - \theta_c)^2]$.

3.2.3.1 To test the maintenance of well-balanced property

In order to verify that the models indeed maintain well-balanced property, we use a steady atmosphere over a smooth mountain (a Gaussian-hill), and a non-smooth mountain (a conical mountain, as (3.22)) respectively as a test case. To be specific, the steady atmosphere is given as,

$$u = 0, v = 0, h = h_0.$$

The Gaussian hill is chosen as [46],

$$h_s = h_s^0 \times exp\{-5.0[(x - x_c)^2 + (y - y_c)^2 + (z - z_c)^2]\},$$

where (x, y, z) is the any point on the sphere and (x_c, y_c, z_c) is the point at $(\lambda_c, \theta_c) = (3\pi/2, \pi/6)$.

Table 3.1 and 3.2 show L_1 and L_∞ error of the components of momentum of hu and hv under double precision for smooth bottom and nonsmooth bottom, respectively. All numerical runs are integrated for 1 model day with $N_e = 20, N = 3, \triangle t = 30\,sec$. We can see that for the smooth mountain, both vector-invariant form and flux-form reach the roundoff error, which indicates the maintenance of the well-balanced property. However, for the nonsmooth mountain, the vector-invariant form still preserves well-balanced property while the flux-form DG loses this property. After making the well-balanced correction to the flux-form, we can see that the flux-form DG keeps well-balanced property for the steady atmosphere.

Table 3.1: Well-balanced check for a steady flow field with a Gaussian smooth mountain

SW DG model	L^1 error		L^∞ error	
	hu	hv	hu	hv
V.I. form	1.61E-15	1.64E-15	1.74E-15	1.87E-15
flux-form	1.57E-13	1.58E-13	1.75E-12	1.74E-12

3.2.3.2 Inviscid DG of flux-form SWEs to SW test-case 5

This test-case is mainly designed for conservation check for the global invariants. Spectral elements and spectral transform suffer from the generation of spurious oscillations at all scales

Table 3.2: Well-balanced check for a steady flow field with a conical non-smooth mountain

SW DG model	L^1 error		L^∞ error	
	hu	hv	hu	hv
V.I. form	1.36E-15	1.42E-15	1.61E-15	1.61E-15
flux-form	1.54E-10	1.06E-10	3.32E-09	3.03E-09
well-balanced flux-form	1.99E-14	2.27E-14	4.44E-14	4.68E-14

for this test problem, which leads to spectral ringings [59]. A 15 model days' time integration is performed for the zonal flow over an isolated mountain. The modal resolution is chosen to be $N_e = 20, N = 3$, which is approximately 1.5° at the equator. The time step size is $\triangle t = 30\,s$ for all the numerical experiments. The height field at day 7 is shown in Fig. (3.8a), and the result from vector-invariant form is plotted in Fig. (3.8b) for reference. The results are visually indistinguishable and similar to the results in [59].

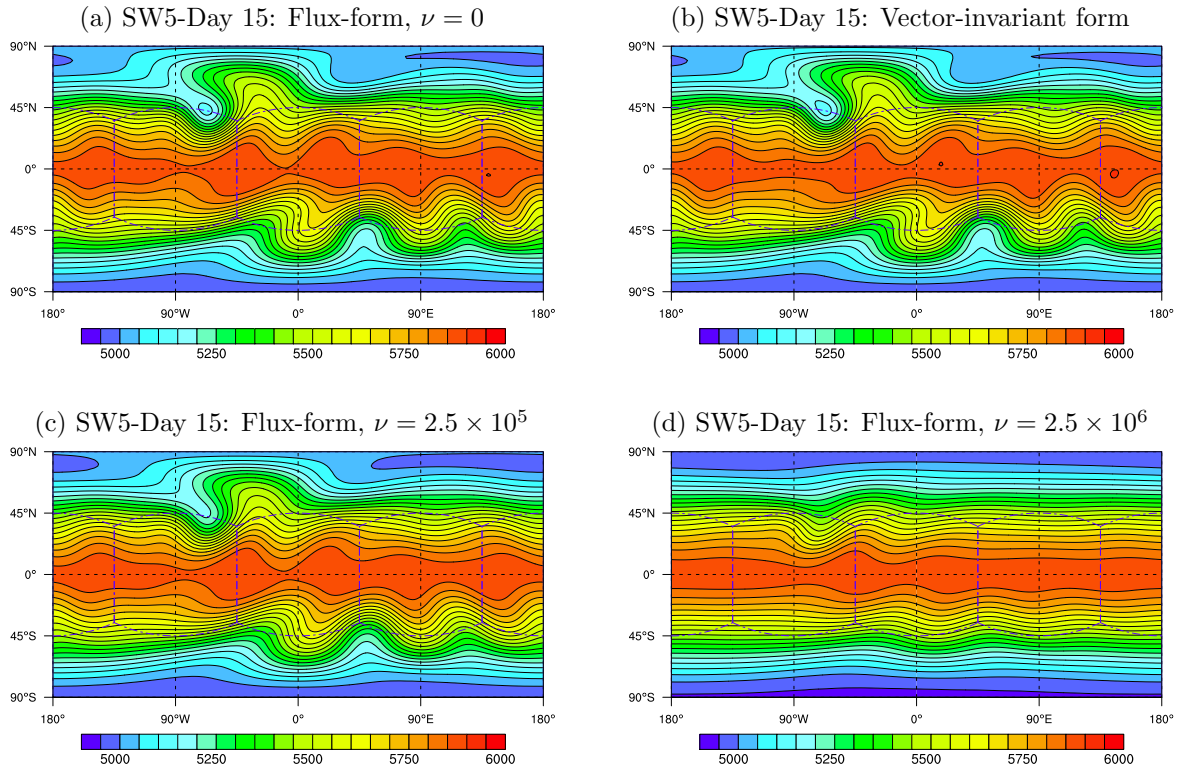

Figure 3.8: Height field of the zonal flow over an isolated mountain wave (SW test-case 5) at day 15 in the resolution $\approx 1.5^\circ$ at the equator ($N_e = 20, N = 3$). (a) is using flux-form. (b) is using vector-invariant form. (c) is using LDG flux-form with $\nu = 2.5 \times 10^5\, m^2\, s^{-1}$. (d) is using LDG flux-form with $\nu = 2.5 \times 10^6\, m^2\, s^{-1}$. $\triangle t = 30\,s$ for all tests.

Time traces of the normalized errors of the conservative quantities: mass, total energy, potential enstrophy and angular momentum are shown in Fig. 3.9. In the non-diffusive case, both forms exhibit comparable performances on preserving the global invariants. In particular, the flux-form has a slightly better conservation of total energy and vector-invariant form shows a better conservation of potential enstrophy.

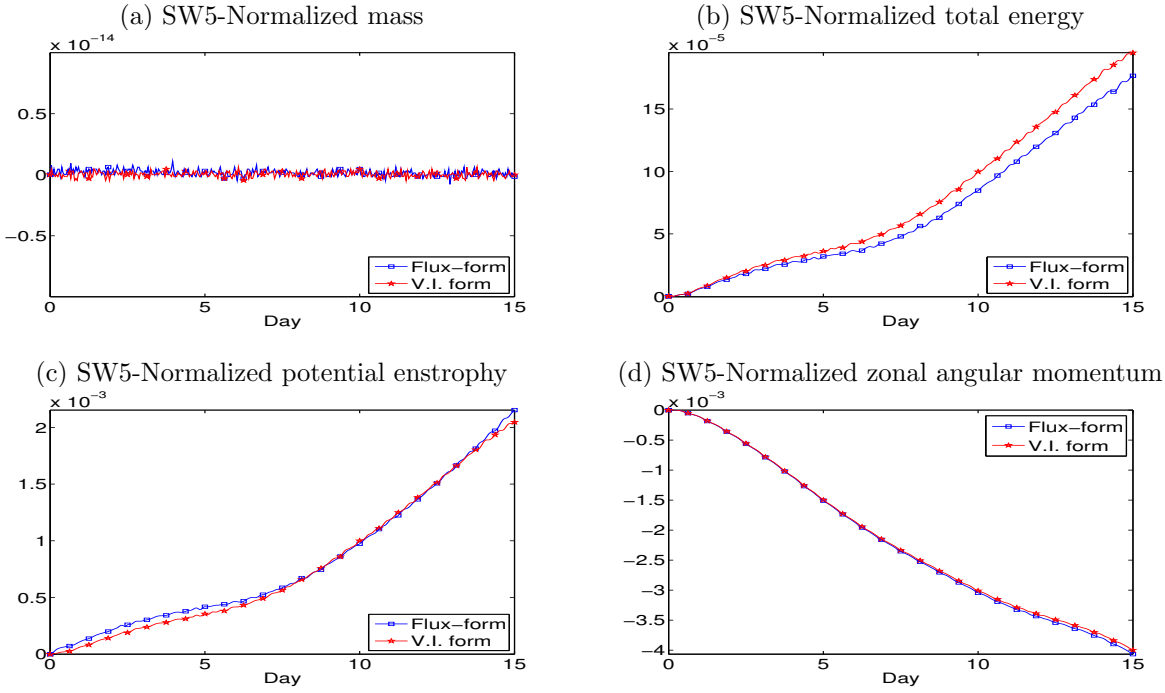

Figure 3.9: Time traces of the normalized errors of (a) mass, (b) total energy, (c) potential enstrophy and (d) zonal angular momentum of two forms of SWEs for the zonal flow over an isolated mountain wave (SW test-case 5) in the resolution $\approx 1.5°$ at the equator ($N_e = 20, N = 3$). Both tests are integrated for 15 days with $\triangle t = 30\,s$.

For the flux-form formulation, the influence of source term involving the non-smooth mountain can be readily seen in the vorticity fields. Although there are several global flux-form SW models [24, 68, 92, 99] use this test-case, unfortunately, the vorticity fields are not available for a comparison. However, we examine the influence of diffusion mechanism in the evolution of relative vorticity fields, by comparing the vorticity fields at day 7 shown in Fig. 3.10. For the well-balanced DG without diffusion, as shown in Fig. (3.8a), there exists some noise in the region where the mountain is located. Compared to the inviscid flux-form, the vector-invariant form produces a

smooth relative vorticity field because the source term in (3.7) does not include the oscillatory gradient terms corresponding to the representation of the mountain h_s. The bottom mountain only exists in the flux term (3.6) and the discontinuity can be partially resolved by the numerical flux. However, it can be observed in Fig. (3.10c), that the appropriate amount of diffusion effect can, to a great extent, eliminate the noise and the resulting vorticity field is very similar to the reference solution shown in Fig. (3.10a). Fig. (3.10d) shows an even smoother vorticity field at the cost of a higher diffusion, however, the corresponding height field shown in Fig. (3.8d) is over-diffused.

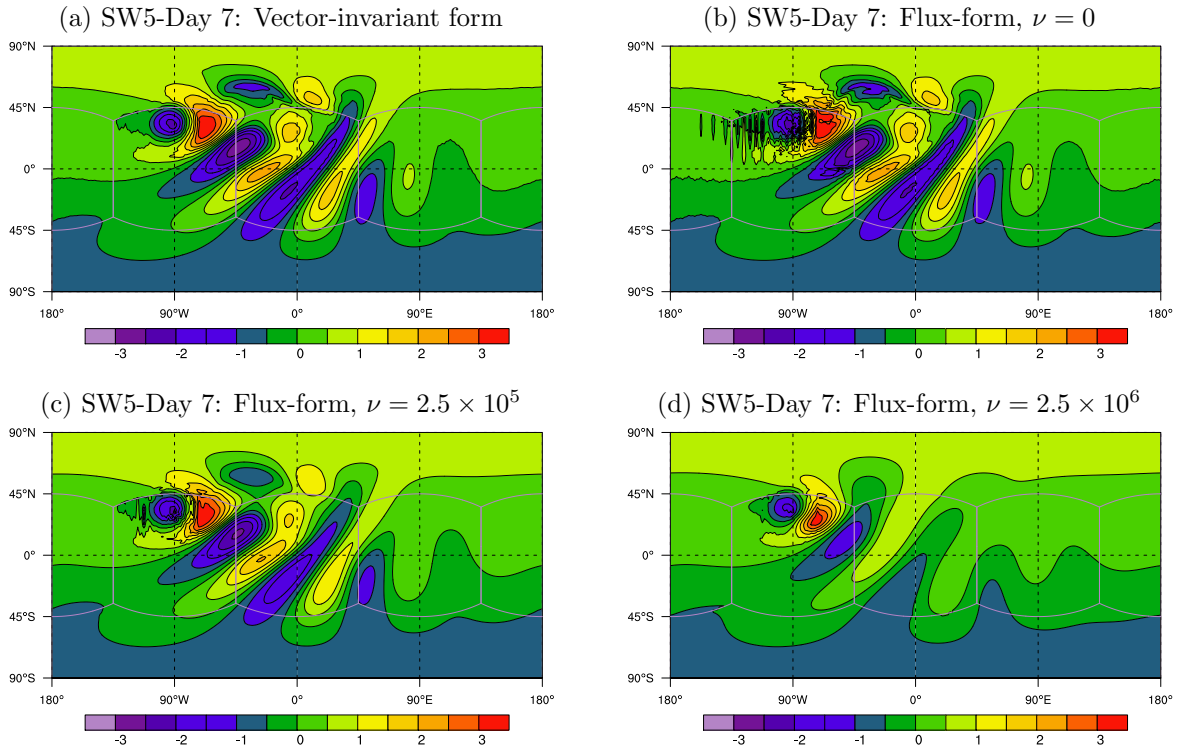

Figure 3.10: Relative vorticity field of the zonal flow over an isolated mountain wave (SW test-case 5) at day 7 in the resolution $\approx 1.5°$ at the equator ($N_e = 20, N = 3$). (a) is using inviscid flux-form and (b) is using vector-invariant form. (c) is using viscid flux-form with $\nu = 2.5 \times 10^5\, m^2\, s^{-1}$. (d) is using viscid flux-form with $\nu = 2.5 \times 10^6\, m^2\, s^{-1}$. $\triangle t = 30\, s$ for all tests. The contour varies from $-3 \times 10^{-5}\, s^{-1}$ to $3 \times 10^{-5}\, s^{-1}$ with an increment of $5 \times 10^{-6}\, s^{-1}$.

3.2.3.3 Well-balanced DG with numerical diffusion

To examine the influence of the diffusion effect on the maintenance of the conservative integrals, time traces of the normalized errors of mass, total energy, potential enstrophy and zonal angular momentum are shown in Fig. 3.11. Unlike the previous cases, the magnitude of normalized errors first decreases and then increases as the magnitude of the diffusion coefficient grows. This is mainly due to the fact that the inviscid flux-form generates some spurious vorticity near the mountain region and proper diffusion effect (here choose $\nu = 2.5 \times 10^5\, m^2 s^{-1}$) can suppress the noise in the relative vorticity field, as shown in Fig. (3.10c). Further increase in the diffusion effect leads to an over-diffused state, which is not acceptable. So the conservative properties are further destroyed besides the effect from the numerical scheme itself. As the diffusion coefficient increases to $2.5 \times 10^6\, m^2\, s^{-1}$, the magnitude of the normalized error grows. However, a high-order diffusion (∇^{2n}) can more efficiently remove the noise without adversely affecting the flow field [23], which is not considered here.

3.3 Summary and Conclusion

A full flux-form discontinuous Galerkin (DG) shallow-water (SW) model on the cubed-sphere has been developed. The cubed-sphere is based on non-orthogonal curvilinear coordinates and uses equiangular central projection. To address the explicit non-smooth source terms in the momentum equations, the well-balanced DG scheme proposed by Xing et al. has been extended to the global SW model. The resulting DG discretization uses a high-order nodal basis set consisting of Lagrange-Legendre polynomials and adopts the Lax-Friedriches numerical flux combined with the well-balanced flux modification. Time integration relies on a strong stability-preserving (SSP) explicit Runge-Kutta scheme. The viscous variant of the SW model employs a second-order diffusion scheme, which is based on the local discontinuous Galerkin (LDG) method. The diffusion terms (Laplacians) of the model involving curvilinear metric terms are solved via a first-order system. In order to demonstrate accuracy and conservation properties, we have tested the proposed model

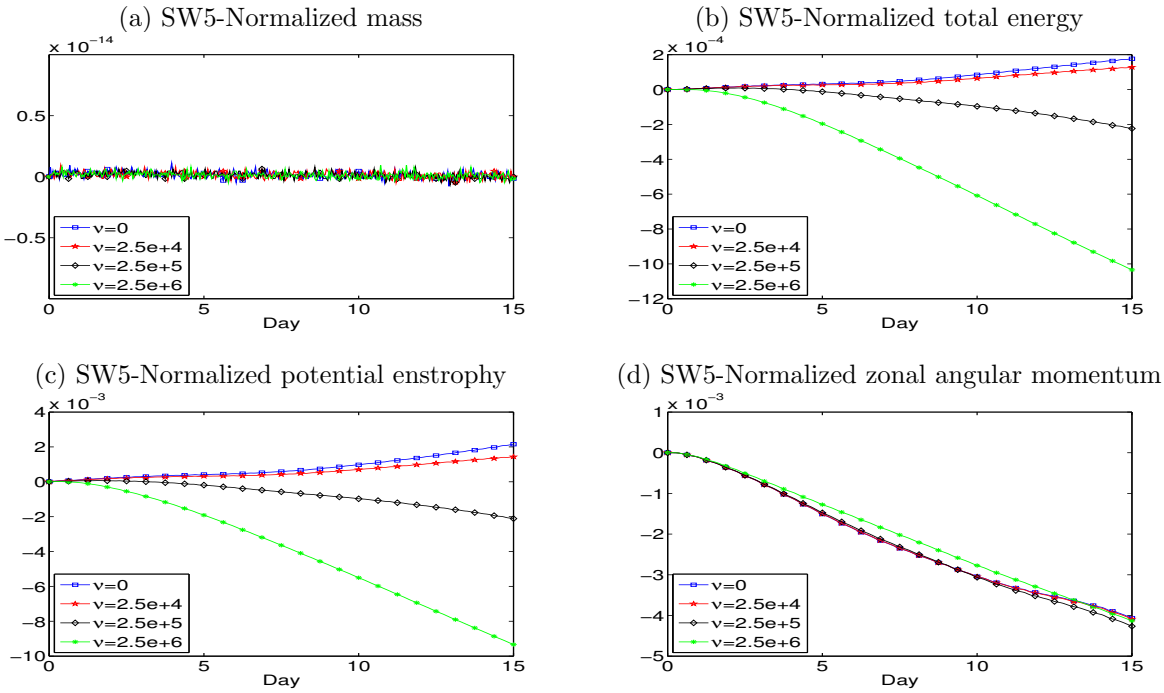

Figure 3.11: Time traces of normalized errors of mass (a), total energy (b), potential enstrophy (c) and zonal angular momentum (d) of LDG flux-form SW model for the flow over a mountain (SW test-case 5) in the resolution $\approx 1.5^\circ$ at the equator ($N_e = 20, N = 3$). The diffusion coefficient varies from $\nu(m^2 s^{-1}) = 0, 2.5 \times 10^4, 2.5 \times 10^5, 2.5 \times 10^6$. All tests are integrated for 15 days with $\triangle t = 30\, s$

with a suite of SW test-cases, including two benchmark test-cases from Williamson et al. [95] and a barotropic instability test from Galewsky et al. [22]. The inviscid vector-invariant form SW model is used here as a reference. Our goal is to make a rigorous comparison of the two formulations of the SWEs, in terms of physical features such as conservation, for identifying a formulation that would be suitable for a global 3D dynamical-core development.

The accuracy of the inviscid flux-form DG SW model can be demonstrated by the exponential convergence of the SW steady state test-case (SW test-case 2, above). The numerical results are similar to the reference solution obtained via the vector-invariant form DG SW model. For the flux-form SW model, in the presence of a nonflat bottom topography, a special approach which preserves the "well-balanced property" is required. This essentially prevents the source terms in the DG discretization of the flux-form SWEs from exciting spurious modes. The results with a benchmark test, flow over an isolated mountain (SW test-case 5), show that the vector-invariant formulation is well-balanced for both smooth and non-smooth mountains. The flux-form DG SW model is well-balanced for the smooth mountain case. But in the presence of non-smooth mountains, the well-balanced correction is necessary to admit the solution and prevent the spurious numerical behaviors. While monitoring the vorticity field, it is observed that the flux-form SW model generates spurious noise in the vicinity of the mountain, but this is not the case for the vector-invariant form. For the conservation of global invariants, the inviscid flux-form SW model shows better conservation of total energy and angular momentum while the vector-invariant form has a better control on the potential enstrophy.

The LDG scheme for the flux-form SWEs evolves to a diffused state for SW test-case 2, and this process is dependent on the magnitude of the diffusion coefficient ν. For the barotropic instability test, the flux-form SW model combined with the LDG diffusion process produces a result which agrees well with the reference solution shown in Galewsky et al. [22]. This scheme successfully removes the spurious oscillations, and captures the dynamics of the mid-latitude stream. The resulting numerical solutions are smooth and comparable to other published results. The quality of the diffused solution is also influenced by the value of ν. When considering the effectiveness of

the LDG schemes in preserving globally conservative quantities, the normalized errors of the global invariants grow at a faster rate than the inviscid situation and the error growth rates are dependent on the choice of the diffusion coefficient. However, the choice of the diffusion coefficient is mesh-size and problem dependent, and our choice is arbitrary and heuristic.

The SW model has been implemented in the highly parallel efficient HOMME framework [52]. As far as the computational complexity is concerned, the vector-invariant form is simpler and more efficient. The explicit SSP-RK time integration used for our DG SW models has a restrictive time-step size limit. An implicit or semi-implicit time integration would be an effective candidate, and we are considering this option for future application. The flux-form SW model requires additional efforts to discretize the source terms due to the non-smooth mountains, although it may not be an issue for a 3D atmosphere model. This is because the mountains (topography) can be incorporated into the vertical coordinate system, such as the terrain-following coordinate system. This set of equations will probably avoid the requirement of the well-balanced DG discretization for the conservative form of the momentum equations, and that is an interesting topic for future study. In addition, with an appropriate value for ν, high-order (or hyper-) diffusion might better preserve global invariants. A rigorous selection for ν is possible by looking at the kinetic energy spectra, and this may be considered for future research.

As a consequence of the study of the horizontal component, the flux-form of the equation sets will be used for the NH modeling for the following study.

Chapter 4

HEVI for Euler system in two-dimensional framework

4.1 Introduction

With an increased amount of supercomputing resources available to present-day modelers, it is possible to develop global atmospheric models with horizontal grid resolution of the order of a few kilometers. At this fine resolution, the models require a set of non-hydrostatic (NH) governing equations in order to resolve clouds at a global scale [86]. However, this necessitates the development of spatial and temporal discretization schemes which are capable of facilitating excellent parallel efficiency on peta-scale computers. Numerical schemes that can address these challenges should have computationally desirable **local** properties such as compact computational stencils, high on-processor operations and minimal communication footprints. There is a renewed interest in developing new NH models based on finite-volume (FV) [2, 47, 61, 79, 91] and Galerkin methods [10, 25, 27], which are designed to address these computational challenges to a great extent.

Among the emerging approaches for spatial discretization, the discontinuous Galerkin (DG) method stands out as a strong candidate, owing to its several computationally attractive features such as local and global conservation, high-order accuracy, high parallel efficiency and geometric flexibility. The DG method may be viewed as a hybrid approach combining the desirable features of two standard numerical discretization approaches: FV and the finite-element (spectral-element) methods. The DG spatial discretization combined with Runge-Kutta (RK) time integration provides a class of robust algorithms known as the RKDG method for solving conservation laws [13].

The application of DG methods in atmospheric modeling is becoming increasingly popular in both hydrostatic [52] and NH modeling [10, 27]. A recent review by [53] presents various DG applications in atmospheric science with an extensive list of references. By virtue of the aforementioned advantages, we employ a DG method for the spatial discretization for a NH model based on the compressible Euler system in two dimensions (2D) on the x-z plane, under the terrain-following height-based coordinate system [21]; hereafter this is referred to as the DG-NH model.

The advantage of explicit time-stepping schemes is their simplicity and high parallel efficiency, namely the minimal inter-processor communication, when evaluating the equations of motion (see for example, [16]). Explicit Strong Stability-Preserving (SSP)-RK time integration is typically used together with P^k-DG methods, which employs a set of polynomials of degree up to k, but results in a severe Courant-Friedrichs-Lewy (CFL) stability limit of $1/(2k+1)$; note that this is exact only when $k \leq 1$ (see [13]). The penalizing drawback of this combination is that a numerical method which is high-order in space requires a smaller timestep size than the corresponding low-order variant with the same grid spacing. Besides, for the compressible NH system, the physically insignificant fast-moving sound waves dictate the explicit timestep size, which imposes a stringent stability constraint on the whole system and impedes the computational efficiency. To make matters worse, the vertical grid spacing is several magnitudes smaller than the horizontal grid spacing ($\approx$ 1:1000) in a typical global atmospheric model. The vertical discretization with small grid-spacing permits only a tiny explicit timestep size, and atmospheric models based on this option have only a limited practical value. There are established models based on the anelastic or sound-proof system of equations, which eliminates sound waves from the continuous system [63]. Nevertheless, the solution process of such models involves expensive elliptic solvers, and the ultimate efficiency of the model is tied up with that of the elliptic solvers and associated pre-conditioners. A fully implicit time-stepping approach might be devised to solve the compressible NH model [82], but this again requires expensive implicit solvers. In general, the cost-effectiveness (parallel efficiency) of models that rely upon global elliptic solvers, is not clear in a peta-scale computing environment.

The split-explicit and semi-implicit time-stepping schemes are two possible alternatives that

are widely used in many operational weather forecasting centers. Split-explicit methods fall into the sub-cycling category, where the shorter sub-steps are used for the faster-moving acoustic and gravity terms of the governing equations [86]. In semi-implicit models, acoustic and gravity waves are usually treated implicitly while the advection parts are solved explicitly [17, 76]. Consequently, the timestep size is relaxed from the speed of sound and the gravity waves, which shows relatively better efficiency at the cost of a Helmholtz solver. Implicit-explicit (IMEX) schemes, a variant of semi-implicit schemes, treat the fast time-scale terms implicitly and the slow time-scale terms explicitly. [65] studied IMEX time integrators used with the DG spatial discretization to improve the efficiency of the scheme by rewriting the problem in the form of a pseudo-Helmholtz operator.

The Horizontal Explicit and Vertical Implicit (HEVI) schemes are another type of splitting approach in which the terms responsible for the horizontal dynamics are solved explicitly while treating the vertical terms implicitly [72]. Note that the HEVI scheme may be viewed as a framework where the IMEX time integration schemes can be incorporated. In a recent work, [93] give a detailed comparison of popular options of HEVI time-stepping schemes. For HEVI scheme the maximum timestep size is only limited by the horizontal grid spacing and, this choice of timestep is usually acceptable in the real application as shown in [78, 86]. A linear analysis of various RK HEVI schemes can be found in [49]. Recently, there is a renewed interest on the applications of the HEVI schemes for high-order methods as used in NH modeling. [91] examined three RK IMEX schemes for HEVI splitting of non-hydrostatic solutions using a FV spatial discretization, which includes the crude-splitting, Strang-carryover splitting and ARS(2,3,3) of [5]. A novelty of [91] is the recycling of the solution of the previous timestep as the solution for the first implicit solution for the Strang-carryover scheme. The computational expense due to the implicit solver is optimized by using a Rosenbrock-type solver, which is essentially one Newton iteration. [25] studied the accuracy and efficiency of IMEX methods, when discretized with continuous Galerkin methods, in semi-implicit and HEVI form in non-hydrostatic 3D flows (both on the globe and in the limited area).

In the present work, we investigate the performance of HEVI time-stepping method with the

DG-NH model (hereafter referred to as HEVI-DG) using an operator-split approach. We also use the explicit SSP-RK method without time-splitting for the DG-NH model to provide results for comparison. In order to extend the timestep size with explicit RK methods, we employ moderate order P^k-DG where $k \leq 4$, with exact integration using Gauss-Legendre quadratures, which is different from the high-order formulation considered in [27]. The parallel version of the model is implemented with a horizontal domain decomposition which assumes that the vertical column (z-direction) of data is not distributed across the processors. In this way, the vertical implicit solver does not need any inter-processor communication. Furthermore, we can take advantage of the existing knowledge of the IMEX-RK schemes to generate HEVI-DG schemes with the desired properties and temporal accuracy.

The organization of the paper is as follows. The governing equations and the computational forms are described in Section 2. The DG spatial discretization is discussed in Section 3, followed by the time integration schemes in Section 4. The numerical results for several benchmark test-cases are presented in Section 5. Conclusions and some future work are described in Section 6. The implementation of the diffusion process is detailed in Appendix A.

4.2 The Idealized Non-Hydrostatic model

The model is designed to simulate two-dimensional (2D) airflow over a (x, z) Cartesian domain. The compressible non-hydrostatic Euler system of equations can be written in the following vector form, without specifying the coordinate system:

$$\frac{\partial \rho}{\partial t} + \nabla \cdot (\rho \mathbf{u}) = 0 \tag{4.1}$$

$$\frac{\partial \rho \mathbf{u}}{\partial t} + \nabla \cdot (\rho\, \mathbf{u} \otimes \mathbf{u} + p\, \mathbf{I}) = -\rho g\, \mathbf{k} \tag{4.2}$$

$$\frac{\partial \rho \theta}{\partial t} + \nabla \cdot (\rho \theta\, \mathbf{u}) = 0 \tag{4.3}$$

where ρ is the air density, $\otimes$ is the tensor (outer) product and $\mathbf{k}$ is the basis vector in the z-direction with unit length. $\mathbf{u} = (u, w)^T$ is the velocity vector with the vertical component $w = \mathbf{u} \cdot \mathbf{k}$, p is the pressure, and g is the acceleration due to gravity. $\mathbf{I}$ represents the 2×2 identity matrix, and

$\nabla\cdot$ is the divergence operator. The potential temperature θ is related to the real temperature T by $\theta = T(p_0/p)^{R_d/c_p}$. The above system is closed by the equation of state, $p = C_0(\rho\theta)^\gamma$ where $C_0 = R_d^\gamma p_0^{-R_d/c_v}$. The reference surface pressure $p_0 = 10^5$ Pa, and the other thermodynamic constants are given by $\gamma = c_p/c_v$, R_d =287 J kg^{-1} K^{-1}, c_p = 1004 J kg^{-1} K^{-1}, c_v = 717 J kg^{-1} K^{-1}.

4.2.1 Terrain-following height-based coordinate

Accurate representation of terrain is very important for practical NH modeling where mountain lee waves are forced by the irregularities (topography) of the earth's surface. The height-based vertical coordinate is popular in many non-hydrostatic global models [63, 79, 86]. The terrain following height-based coordinate offers more flexibility and accuracy compared to pressure-based coordinates, and is free from time-dependent terrain metrics [89]. Although the DG method is capable of handling complex domain [27], we prefer to use the classical terrain-following height coordinates introduced by [21]. Recently, more sophisticated terrain-following coordinate systems were developed [41, 75] and will be considered for future development.

If $h = h(x)$ is the prescribed mountain profile and z_T is the top of the model domain, then the vertical z height coordinate can be transformed to the monotonic ζ coordinate using the following mapping:

$$\zeta = z_T\frac{z - h(x)}{z_T - h(x)}, \quad z(\zeta) = h(x) + \zeta\frac{z_T - h(x)}{z_T}; \quad h(x) \le z \le z_T. \tag{4.4}$$

This coordinate transformation invariably introduces tensor quantities and metric terms associated with mapping as described in [12, 21, 72]. Following the standard notations [72], the Jacobian of the transformation is given by $\sqrt{G}$ and defined as

$$\sqrt{G} = \left(\frac{\partial z}{\partial \zeta}\right)_{x=\text{const.}}, \quad G^{13} = \left(\frac{\partial \zeta}{\partial x}\right)_{z=\text{const.}}, \tag{4.5}$$

where the Jacobian and the metric term G^{13} are independent of time. For an arbitrary scalar ψ,

we have the following relation connecting (x, z) and (x, ζ) coordinate systems [12],

$$\sqrt{G}\frac{\partial \psi}{\partial z} = \frac{\partial \psi}{\partial \zeta} \tag{4.6}$$

$$\sqrt{G}\left[\frac{\partial \psi}{\partial x}\right]_{z=\text{const.}} = \left[\frac{\partial}{\partial x}(\sqrt{G}\psi)|_{\zeta=\text{const.}} + \frac{\partial}{\partial \zeta}(\sqrt{G}G^{13}\psi)\right]. \tag{4.7}$$

The vertical velocity in the transformed system (x, ζ) is $\tilde{w}$ and defined as

$$\tilde{w} = \frac{d\zeta}{dt} = \frac{1}{\sqrt{G}}(w + \sqrt{G}G^{13}\, u). \tag{4.8}$$

The divergence operation for a vector field $\mathbf{F} = (F^x, F^z)$ under the coordinate transformation takes the following form,

$$\nabla \cdot \mathbf{F} = \frac{1}{\sqrt{G}}\left[\frac{\partial}{\partial x}(\sqrt{G}F^x) + \frac{\partial}{\partial \zeta}(F^z + \sqrt{G}G^{13}F^x)\right]. \tag{4.9}$$

4.2.2 Removal of the hydrostatic balanced state

In the context of atmospheric modeling, it is common to write the thermodynamic variables as the sum of the mean-state (reference state) $\overline{(.)}$ and perturbation $(.)'$ [78],

$$\rho(x, z, t) = \overline{\rho}(z) + \rho'(x, z, t) \tag{4.10}$$

$$\theta(x, z, t) = \overline{\theta}(z) + \theta'(x, z, t) \tag{4.11}$$

$$p(x, z, t) = \overline{p}(z) + p'(x, z, t) \tag{4.12}$$

$$(\rho\theta)(x, z, t) = \overline{\rho\theta}(z) + (\rho\theta)'(x, z, t) \tag{4.13}$$

where the mean-state satisfies the hydrostatic balance,

$$\frac{d\overline{p}}{dz} = -\overline{\rho}g. \tag{4.14}$$

The mean-state part of the thermodynamic variables is in hydrostatic balance and makes no contribution to drive the dynamics. In contrast, the dynamic processes, or the accelerations, are triggered and influenced by the the perturbation part [12]. Besides, the deviations due to the non-hydrostatic effect from the hydrostatic balance are relatively small, except certain extreme cases such as tornadoes. Embodying the mean-state in the whole system may introduce some errors in

approximating the hydrostatic equilibrium numerically, which may generate some spurious vertical momentum. Therefore, the hydrostatically balanced mean-state is removed from the Euler system.

4.2.3 Governing Equations

Combining the relations (4.5)-(4.9) and substituting in the Euler system (4.1)-(4.3) results in the following general 2D Euler system in the transformed (x, ζ) coordinates:

$$\frac{\partial \mathbf{U}}{\partial t} + \frac{\partial \mathbf{F}^x(\mathbf{U})}{\partial x} + \frac{\partial \mathbf{F}^\zeta(\mathbf{U})}{\partial \zeta} = \mathbf{S}(\mathbf{U}) \quad \Rightarrow \quad \frac{\partial \mathbf{U}}{\partial t} + \nabla \cdot \mathbf{F}(\mathbf{U}) = \mathbf{S}(\mathbf{U}) \tag{4.15}$$

where $\mathbf{U}$ is the state vector and $\mathbf{U} = [\sqrt{G}\rho', \sqrt{G}\rho u, \sqrt{G}\rho w, \sqrt{G}(\rho\theta)']^T$, $\mathbf{S}$ is the source term and $\mathbf{S} = [0, 0, -\sqrt{G}\rho' g, 0]^T$. $\mathbf{F}^x$, $\mathbf{F}^\zeta$ are the flux vectors along x and ζ directions respectively, which have the following forms

$$\mathbf{F}^x = \begin{bmatrix} \sqrt{G}\rho u \\ \sqrt{G}(\rho u^2 + p') \\ \sqrt{G}\rho u w \\ \sqrt{G}\rho u \theta \end{bmatrix}, \quad \mathbf{F}^\zeta = \begin{bmatrix} \rho\tilde{w} \\ \rho u\tilde{w} + \sqrt{G}G^{13}p' \\ \rho w\tilde{w} + p' \\ \rho\tilde{w}\theta \end{bmatrix}, \quad \mathbf{S} = \begin{bmatrix} 0 \\ 0 \\ -\sqrt{G}\rho' g \\ 0 \end{bmatrix} \tag{4.16}$$

and $\mathbf{F} = (\mathbf{F}^x, \mathbf{F}^\zeta)$. The compressible 2D Euler system (4.15) is the basis for the DG-NH model. Note that in the absence of topography ($h(x) = 0, \zeta = z$), we have $\sqrt{G} = 1, G^{13} = 0$ and $w = \tilde{w}$.

4.2.4 Final form after DG spatial discretization

For the Euler system, $\lambda_{\max}$ is the upper bound on the absolute value of eigenvalues of the flux Jacobian $\mathbf{F}'(U)$, which is a function of the wind speed $\mathbf{u}$ and speed of sound waves c, evaluated at the interface:

$$\lambda_{\max} = \max\{|v^-| + c, |v^+| + c\}, c = \sqrt{\gamma R_d T}, \quad v^\pm = \mathbf{u}^\pm \cdot \vec{n}. \tag{4.17}$$

The final form of the spatial discretization, starting from the conservation law (4.15) via the weak form (2.3), leads to an ODE for each $U_{lm}(t)$,

$$\frac{d}{dt}U_{lm}(t) = \frac{4}{\Delta x_i \Delta z_j \, w_i w_j} \left[I_{Grad} + I_{Flux} + I_{Source} \right], \tag{4.18}$$

where the coefficients $4/(\Delta x_i \Delta z_j \, w_i w_j)$ constitute the inverted mass matrix for an element Ω_{ij}. I_{Flux} is the line integral and, I_{Grad}, I_{Source} are the surface integrals corresponding to the discretization of the weak form (2.3). Explicit definitions of these terms are given in [53]. Therefore, the ODE in time corresponding to system (4.15) is,

$$\frac{d}{dt}\mathbf{U}_h(t) = \mathbf{L}(\mathbf{U}_h), \tag{4.19}$$

where $\mathbf{L}$ indicates the spatial DG discretization.

4.3 Time Integration Procedure

In the construction of high-order Runge-Kutta (RK) DG methods (hereafter, we call DG for RK-DG in short), the spatial terms are discretized first, and the resulting ODE system for the prognostic variables is solved by a proper time integration scheme. The DG spatial discretization of the Euler system is fairly standard, which is elaborated in Section **??**, however, the design of an efficient time integrator is of predominant importance, especially when we reach the non-hydrostatic scale.

We discuss the time integrator for an ODE system in the following general form,

$$\mathbf{U}'(t) = f(\mathbf{U}(t), t) \quad \text{in} \quad (0, t_T], \tag{4.20}$$

where $\mathbf{U}(t)$ are the coefficients to the DG solution $\mathbf{U}_h(t)$. For the Euler's system (4.19), the right hand side function f is given by

$$f(\mathbf{U}(t), t) \quad = \quad \mathbf{L}(\mathbf{U}_h(t)) \tag{4.21}$$

In this paper, we investigate a HEVI-type splitting approach and compare it with commonly used explicit time stepping methods. All the time integrators considered in our development may be characterized as RK type methods.

4.3.1 RK methods

Given the solution U^n at time t^n, we use an s-stage RK method to obtain the solution at the next time level t^{n+1}. For a given U^n and some integer $s > 0$, the coefficients $A \in \mathbb{R}^{s\times s}$, $b \in \mathbb{R}^s$, and $c \in \mathbb{R}^s$ define the s-stage RK method:

$$\begin{aligned} K_i &= f\big(t^n + c_i\Delta t, U^n + \Delta t \textstyle\sum_{j=1}^{s} A_{ij}K_j\big), \quad i = 1, ..., s \\ U^{n+1} &= U^n + \Delta t \textstyle\sum_{i=1}^{s} b_i K_i. \end{aligned} \tag{4.22}$$

The coefficients $\mathbf{A} = [A_{ij}]$, $\mathbf{b} = [b_i]$, and $\mathbf{c} = [c_j]$ form the so-called Butcher tableau[11]:

$$\begin{array}{c|c} \mathbf{c} & \mathbf{A} \\ \hline & \mathbf{b}^T \end{array} \quad .$$

For an explicit RK method, $A_{ij} = 0$ for all $j \geq i$, which corresponds to all entries of $\mathbf{A}$ on and above the diagonal being zero. Some popular examples of explicit SSP-RK methods [28], which are widely used with the DG discretization [53], are as follows:

Heun's method(SSP-RK2)

(2-stage 2^{nd} order)

$$\begin{array}{c|cc} 0 & 0 & \\ 1 & 1 & 0 \\ \hline & \frac{1}{2} & \frac{1}{2} \end{array}$$

Explicit Runge-Kutta (SSP-RK3)

(3-stage 3^{rd} order)

$$\begin{array}{c|ccc} 0 & 0 & & \\ 1 & 1 & 0 & \\ \frac{1}{2} & \frac{1}{4} & \frac{1}{4} & 0 \\ \hline & \frac{1}{6} & \frac{1}{6} & \frac{2}{3} \end{array}$$

For implicit RK methods, we consider Diagonally Implicit RK (DIRK) [3] methods. DIRK methods are characterized by the fact that the coefficients $A_{ij} = 0$ for $j > i$, in which case, all entries of $\mathbf{A}$ above the diagonal are zero. DIRK methods have the advantage that the resulting non-linear systems can be solved one-by-one. A popular DIRK method is given below [3]:

Heun's method (DIRK2)

(1-stage 2^{nd} order)

$$\begin{array}{c|c} \frac{1}{2} & \frac{1}{2} \\ \hline & 1 \end{array}$$

For the solution of the non-linear system for each RK stage, which arises due to the non-zero diagonal entries of $\mathbf{A}$ in (4.22), we apply a Jacobian-free Newton-Krylov (JFNK) method [43]. A GMRES [69] solver is applied for the linear system in each Newton step and the application of the right-hand-side operator f in each GMRES iteration is accomplished in a matrix-free fashion.

Explicit time integrators are relatively easy to implement and usually possess excellent parallel scalability. However, the general drawback with the application of explicit SSP-RK methods in DG methods is the severe timestep restrictions, i.e. a CFL number much smaller then 1 has to be used. For the P^k-DG algorithm, a heuristic estimation of the CFL number is given by [13],

$$\frac{C\Delta t}{h} < \frac{1}{2k+1}. \tag{4.23}$$

where $h = \min\{\Delta x, \Delta z\}$, where Δz denotes the grid spacing in vertical direction and Δx the grid spacing in horizontal direction, and $C = \max\{|u| + c, |w| + c\}$, $c = \sqrt{\gamma R_d T}$ is the speed of sound. The resulting timestep size for an explicit time integration scheme is usually very tiny. In contrast, the implicit ODE solver has a large stability region, which admits a large timestep size, but is expensive to solve in general. The construction of the implicit solver for multi-dimensional problems is usually complicated and requires complex non-linear solvers. The overall efficiency may not be competitive with the explicit solver and the computational scalability may even be degraded if the nonlinear solver is not designed properly. The hope of an efficient time integrator, which enables a large timestep size and excellent computational efficiency, has triggered a vast research effort into implicit and semi-implicit time integration methods.

4.3.2 Horizontally Explicit and Vertically Implicit (HEVI) Scheme via Strang-splitting

A popular approach in atmospheric applications is the "horizontally explicit and vertically implicit" (HEVI) approach. This is justified by the relatively large difference of scales in the horizontal and vertical directions, i.e. $\Delta z \ll \Delta x$. Although a large Δx still results in an acceptable CFL restriction for the present study, the small Δz introduces noticeable difficulties due to the severe CFL restriction in the vertical direction. As a result, a splitting approach with an implicit treatment in the vertical direction stands out as a suitable alternative. The horizontal direction is still treated explicitly, allowing the usage of the excellent scaling behavior of explicit methods. For the practical atmospheric applications, the horizontal CFL condition can be further relaxed by sub-cycling or multi-rate integrations [86], which is beyond the scope of the present work.

In our development, the domain decomposition for parallel computations is carried out in the horizontal direction only, which is broadly embraced in the atmospheric community [**?**]. Therefore, all data is locally accessible in the vertical direction and an implicit treatment in the vertical direction does not require any communication. As a consequence, we expect the excellent scaling performance on today's many core systems to be maintained.

We split the DG spatial operator $\mathbf{L}$ (4.19) into a horizontal (x) and a vertical (z) part such that

$$\mathbf{L}(\mathbf{U}_h) = \mathbf{L}^x(\mathbf{U}_h) + \mathbf{L}^z(\mathbf{U}_h), \tag{4.24}$$

where $\mathbf{L}^x$ and $\mathbf{L}^z$ are the DG 1D discretization to (4.25)-(4.26), respectively:

$$\frac{\partial \mathbf{U}_h}{\partial t} = -\frac{\partial \mathbf{F}^x(\mathbf{U}_h)}{\partial x} + \mathbf{S}^x \tag{4.25}$$

$$\frac{\partial \mathbf{U}_h}{\partial t} = -\frac{\partial \mathbf{F}^z(\mathbf{U}_h)}{\partial z} + \mathbf{S}^z \tag{4.26}$$

Note that, for the dimensional splitting used here, the source term is decomposed as $\mathbf{S}^x = 0$ and $\mathbf{S}^z = \mathbf{S}$. The definitions of $\mathbf{F}^x$, $\mathbf{F}^z$, and $\mathbf{S}$ are given in (4.16). Instead of solving the full system (6.14), we solve the system in the horizontal direction (4.25) and the system in the vertical

direction (4.26) separately in a sequence, via the Strang-type splitting [84]. Strang-type splitting has been successfully applied in FV methods [61, 91] and it also shows promising performances when applied to semi-Lagrangian DG methods for different geometries by [30]. Given a time interval of size Δt and the solution $\mathbf{U}_h^n$ at t_n, the corresponding Strang-splitting scheme has the following steps:

$$\mathbf{U}_0 = \mathbf{U}_h^n \tag{4.27}$$

$$\frac{d}{dt}\mathbf{U}_1 = \mathbf{L}^x(\mathbf{U}_1) \quad \text{in} \quad (t^n, t^n + \Delta t/2], \qquad \mathbf{U}_1(t^n) = \mathbf{U}_0, \tag{4.28}$$

$$\frac{d}{dt}\mathbf{U}_2 = \mathbf{L}^z(\mathbf{U}_2) \quad \text{in} \quad (t^n, t^{n+1}], \qquad \mathbf{U}_2(t^n) = \mathbf{U}_1(t^n + \Delta t/2), \tag{4.29}$$

$$\frac{d}{dt}\mathbf{U}_3 = \mathbf{L}^x(\mathbf{U}_3) \quad \text{in} \quad (t^n + \Delta t/2, t^{n+1}], \qquad \mathbf{U}_3(t^n + \Delta t/2) = \mathbf{U}_2(t^{n+1}), \tag{4.30}$$

$$\mathbf{U}_h^{n+1} = \mathbf{U}_3(t^{n+1}). \tag{4.31}$$

This approach requires the solution of the three equations (4.28)-(4.30), which means that the horizontal part is solved for twice and the vertical part once (H-V-H). It would also be possible to solve the system in V-H-V form, but ideally the more expensive system should only be solved once. In our choice, we only solve the vertical system once. We also tested the Strang-carryover scheme [91], which is essentially V-H-V, with the first stage in the vertical is recycled from the previous timestep, however, the solution is found to be degraded, even for a smooth test case.

Since we usually prefer higher order in the DG spatial discretization, the time integrator will be the dominant factor in the numerical error. Strang-type splitting permits second-order temporal accuracy [87], therefore we choose SSP-RK3 as the explicit time integrator for the horizontal direction (4.25) and we solve the vertical direction (4.26) either with the explicit RK method SSP-RK2, which leads to an Horizontal Explicit and Vertical Explicit (HEVE) method, for comparison studies, or with an implicit time stepping method DIRK2, which is our HEVI scheme. Therefore, the time integration schemes studied in the present paper are given as follows,

HEVI (or HEVE) Time integrator

(1) Solve (4.28) via SSP-RK3,

(2) Solve (4.29) via DIRK2 (or SSP-RK2),

(3) Solve (4.30) via SSP-RK3.

The introduction of the HEVE time integration scheme is solely for the purpose of validating the idea of dimensional splitting for DG methods and, in practice, we would adopt the HEVI scheme for practical applications. When using an implicit method for the vertical direction (4.26), it is observed that the CFL condition for the whole system may be relaxed to the CFL condition for the horizontal part only. In other words, Δt for the Strang-splitting can be chosen as the largest possible Δt of (4.25). In this way, the overall performance can be greatly accelerated. Nevertheless, the necessity of solving an implicit system introduces an additional overhead. In terms of the performance of the DIRK methods, usually the number of Newton iterations is very small. i.e. 1 or 2 and usually not higher than 5. Therefore, the performance of the implicit solver is closely related to the number of iterations of the linear solver. This can be reduced by proper preconditioning. However, in the current implementation, no preconditioning is applied. The construction of a proper preconditioning method is ongoing work. In addition, due to our domain decomposition, we obtain an implicit system for each vertical column which is decoupled for the other column systems. Therefore, no communication is needed for the implicit solvers. Even a direct solver could be applied since the system for one column is not that large. This will overcome the need for preconditioning the iterative solvers used otherwise.

The existing IMEX schemes [5, 25] can be easily incorporated into the HEVI-DG framework, which may yield some beneficial properties. In order to apply an IMEX time integrator, we first rewrite our problem such that we distinguish between a part that should be treated implicitly, here $\mathbf{L}^{\text{im}}$, and a part that should be treated explicitly, here $\mathbf{L}^{\text{ex}}$, such that

$$\frac{d}{dt}\,\mathbf{U}_h = \mathbf{L}^{\text{im}}(\mathbf{U}_h) + \mathbf{L}^{\text{ex}}(\mathbf{U}_h) \quad \text{in} \quad (t_n, t_{n+1}]. \tag{4.32}$$

For the IMEX RK method, we define $f^{\text{im}}(\mathbf{U}(t), t) = \mathbf{L}^{\text{im}}(\mathbf{U}(t))$ and $f^{\text{ex}}(\mathbf{U}(t), t) = \mathbf{L}^{\text{ex}}(\mathbf{U}(t))$. The

performance of IMEX schemes combined with DG spatial discretization may be revisited in a future study.

4.4 Numerical Experiments

In order to demonstrate and evaluate the HEVI time integration scheme in the DG-NH model, we choose several standard benchmark tests from the literature. Before detailing with each test case, we briefly discuss some common features such as the grid resolution, boundary conditions, and the initialization process used in the DG-NH model.

4.4.1 Numerical Experiments Setup

The spatial resolution should take account of the grid-spacing within each element for the nodal DG (RK-DG) method. For the GL case, the edge points of each element are not included as solution points (see Fig. 2.2), therefore we use an approximate procedure to define the minimum grid-spacing for the P^k-DG method, which has $k+1$ degrees-of-freedom (**dof**) in each direction. The **average** grid spacing is defined in terms of **dof** as

$$\Delta x = \Delta x_i/(k+1), \Delta z = \Delta z_j/(k+1), \tag{4.33}$$

where Δx_i and Δz_j are the element width in the x-direction and z-direction respectively. We employ uniform elements over the whole domain, and use this convention(4.33) as the grid resolution in our DG-NH model. Note that, our definition of grid spacing is similar to [10] but different from that of [27], where they use the GLL grid. The DG-NH model, designed for a rectangular domain, requires suitable boundary conditions for various test cases. These include no-flux, periodic, and non-reflecting type boundary specifications.

4.4.1.1 No-flux boundary conditions

Essentially, the no-flux (or reflecting) boundary conditions eliminate the normal velocity component to the boundary and only keeps the tangential component. For an arbitrary velocity

vector $\mathbf{v}$, the no-flux boundary condition results in $\mathbf{v} \cdot \mathbf{n} = 0$, where $\mathbf{n}$ is the outdrawn normal vector from the boundary. We denote $(v^{\parallel}, v^{\perp})$ as the parallel (tangential) and perpendicular (normal) components, respectively, of $\mathbf{v}$ along the boundary wall; let the left and right values at the element edge of $\mathbf{v}$ along the boundary be v_L and v_R, respectively. Then the no-flux boundary conditions can be written in the following form,

$$v_R^{\perp} = -v_L^{\perp}, \quad v_R^{\parallel} = v_L^{\parallel}. \tag{4.34}$$

The same idea is used for the flux vectors along the boundary.

4.4.1.2 Non-reflecting boundary conditions

The non-reflecting (or transparent) boundary conditions are used to prevent the reflected waves from reentering the domain, which may interfere or pollute the flow structure. For the mountain test cases, non-reflecting boundary conditions are commonly imposed at the top (z_T) and the lateral boundaries, by introducing the sponge (absorbing) layers of finite width as discussed in [18]. A schematic plot of the non-reflecting boundary conditions is shown in Fig. 4.1.

We use a simple damping function as given below, and the damping terms will act as an additional forcing to the governing equations (4.15). The prognostic vector $\mathbf{U}$ is then damped by relaxing to its initial state $\mathbf{U}_0$.

In the presence of orography, the governing equations become

$$\frac{\partial \mathbf{U}}{\partial t} = \cdots - \tau(x, z)\,(\mathbf{U} - \mathbf{U}_0) \tag{4.35}$$

where $\tau(x, z)$ is the sponge function, and at the upper boundary it is defined as [50]

$$\tau(x, z) = \begin{cases} 0, & \text{if } z_T - z \geq z_D, \\ \tau_{top} \left[\sin\left(\frac{\pi}{2} \frac{|z_T - z| - z_D}{z_D}\right) \right]^4 & \text{otherwise}, \end{cases} \tag{4.36}$$

where τ_{top} is the specified sponge coefficient, z_D is the thickness of the sponge zone from the domain boundary z_T in z-direction. The sponge function is accountable for the strength of damping over the zone. Similarly, for the lateral boundaries sponge functions can be defined with sponge coefficient

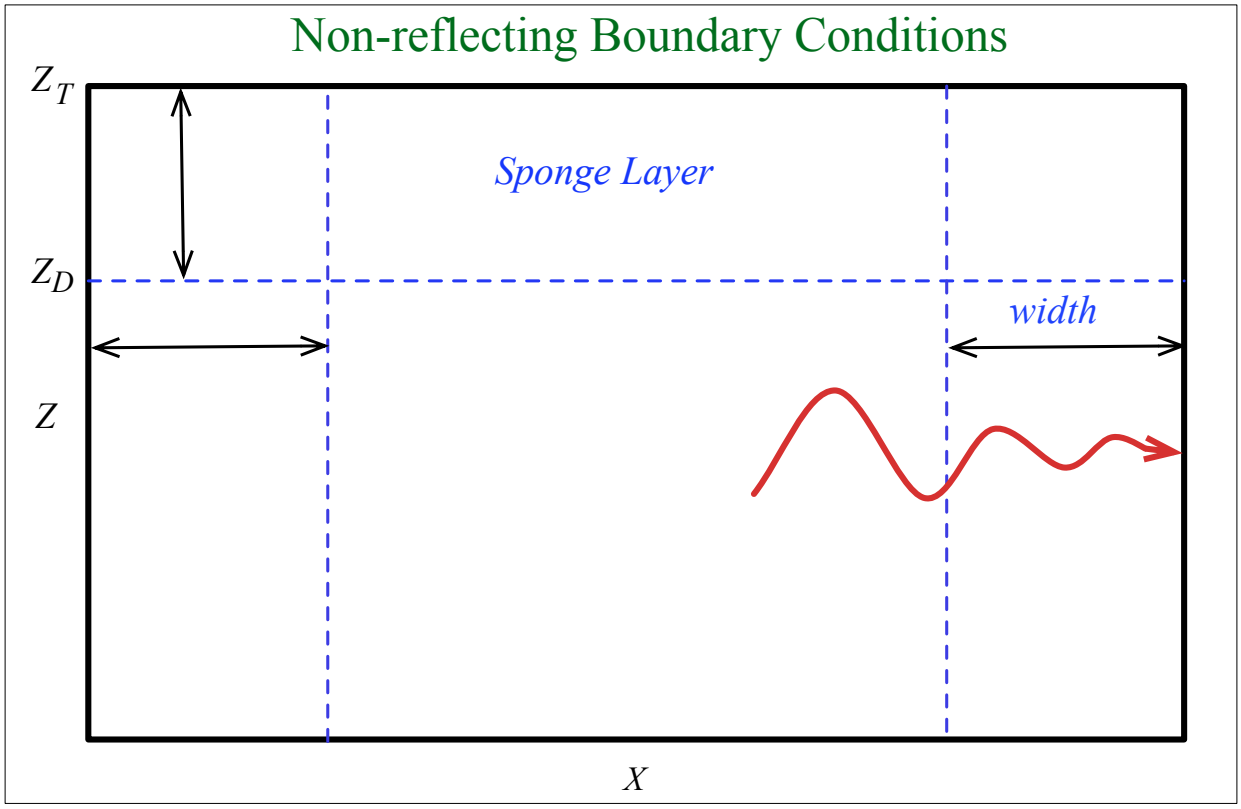

Figure 4.1: A schematic plot of the non-reflecting boundary conditions

τ_{lat}. In the overlap region (upper corners), we use the maximum of the coefficients in the x and z directions. The damping term in (4.36) has no effect on the interior part of the domain. Note that the magnitude of sponge thickness z_D, τ_{top} and τ_{lat} is model-dependent, a choice of which is in fact a trade-off between computational expense and the quality of the solution.

4.4.1.3 Initial conditions

For the DG-NH model, we use several standard conversion formulas for model initialization and maintain the hydrostatic balance. To initialize the hydrostatic balance, we obtain a vertical profile for the Exner pressure π which is a function of pressure, given as:

$$\pi = \left(\frac{p}{p_0}\right)^{R_d/c_p}, \tag{4.37}$$

which follows the hydrostatic balance

$$\frac{d\pi}{dz} = -\frac{g}{c_p\,\theta}. \tag{4.38}$$

For some of the tests, a constant Brunt-Väisälä frequency N_f is specified and therefore $\bar{\theta}(z)$ can be computed from the following formula:

$$N_f^2 = g\frac{d}{dz}(\ln\overline{\theta}) \quad \Rightarrow \quad \overline{\theta}(z) = \theta_0\,\exp\left(\frac{N_f^2}{g}z\right), \tag{4.39}$$

where θ_0 is a given constant. Once $\overline{\theta}(z)$ is known, the hydrostatically balanced Exner pressure (4.37) can be derived as below:

$$\overline{\pi}(z) = 1 + \frac{g^2}{c_p\theta_0 N_f^2}\left[\exp\left(-z\frac{N_f^2}{g}\right) - 1\right] = 1 - \frac{g^2}{c_p N_f^2}\left[\frac{\overline{\theta}(z) - \theta_0}{\overline{\theta}(z)\,\theta_0}\right]. \tag{4.40}$$

Another useful formula for computing $\overline{\rho}$ from $\overline{\pi}$ by using the conversion $\overline{T} = \overline{\theta}(z)/\overline{\pi}(z)$ is

$$\overline{\rho} = \frac{p_0}{R_d\,\overline{T}}\,\overline{\pi}^{(c_p/R_d)}. \tag{4.41}$$

For better visualization, the numerical results obtained from the DG-NH model simulations on the GL grid are bilinearly interpolated onto a high-resolution uniform grid.

4.4.2 Idealized NH test cases

We consider several NH benchmark test cases with varying complexities for validating the DG-NH model with HEVI time stepping. Except for the first test, all other test cases have no analytical solution and will therefore be evaluated qualitatively.

4.4.2.1 Traveling Sine-Wave Test

In order to study the convergence of the HEVI scheme, we consider a test-case where an analytical solution is available for the Euler equations. This test case is described in [48], but we use a slight modification for the velocity and pressure suitable for our application. This test-case simulates the traveling of sine waves at a non-hydrostatic scale on a square domain $[0,1]\times[0,1]$ m^2,

where the waves march along the diagonal direction. The constant wind fields $\mathbf{u} = (u_0, w_0)$ are defined as,

$$u_0(x,z,t) = \sin\frac{\pi}{5}, \quad w_0(x,z,t) = \cos\frac{\pi}{5}. \tag{4.42}$$

The pressure p is set to be a constant 0.3 Pa, and the density is given as follows:

$$\rho(x,z,t) = \begin{cases} 0.5 & \text{if } R > 1.0, \\ 0.25[\cos\big(\pi R(x,z,t)\big) + 1.0]^2 + 0.5 & \text{else}, \end{cases} \tag{4.43}$$

where $R(x,z,t) = 16[(x-0.5-ut)^2 + (z-0.5-wt)^2]$. The initial condition can be obtained by setting $t = 0$ s. Periodic boundary conditions are imposed for all four boundaries, and the simulation time is $t_T = 0.1$ s. To fit the governing equations (4.15), the hydrostatically balanced variables $(\bar{\rho}, \bar{p}, \bar{\theta})$ are all set to zero. We neglect the influence of gravity and set the source term S in (4.16) to zero.

This test case mainly serves as a tool for the convergence study for the HEVI (or HEVE) scheme. For the tests a uniform grid with $\Delta x = \Delta z$ is chosen, regardless of the resolution. The L_2 error norms of HEVI, HEVE and SSP-RK3 schemes are presented in Fig. 4.2, to show spatial errors (left panel) and temporal errors (right panel). In order to obtain the spatial convergence of the P^2-DG with respect to different time integration schemes, a reference solution is computed from the analytical solution at 0.1 s. The grid-spacing Δz is halved (i.e., by doubling N_x and N_z) from 3.33×10^{-2} m ($N_x = 10, N_z = 10$) until 4.17×10^{-3} m ($N_x = 80, N_z = 80$); and Δt is set to 5.0×10^{-4} s for $\Delta z = 3.33 \times 10^{-2}$ m initially, and decreased linearly with Δz. It is observed that HEVI, HEVE and SSP-RK3 show $\mathcal{O}(\Delta z^3)$ convergence, which is in line with the theoretical analysis for the DG spatial discretization.

In order to obtain the temporal convergence, we choose high-order P^6-DG to make the temporal error dominant over spatial errors. The grid resolution is set to 7.143×10^{-3} m ($N_x = 20, N_z = 20$), and Δt decreased to obtain the trend of temporal errors. The reference solution is computed from $\Delta t = 3.125 \times 10^{-4}$ s and Δt is halved from 5×10^{-4} s until 6.25×10^{-5} s. The L_2 error norms of all three time integrators are plotted in the right panel of Fig. 4.2. We observe that

SSP-RK3 shows third-order temporal convergence. Both HEVI and HEVE only achieve second-order temporal convergence because the numerical errors of HEVI and HEVE are controlled by the second-order splitting errors.

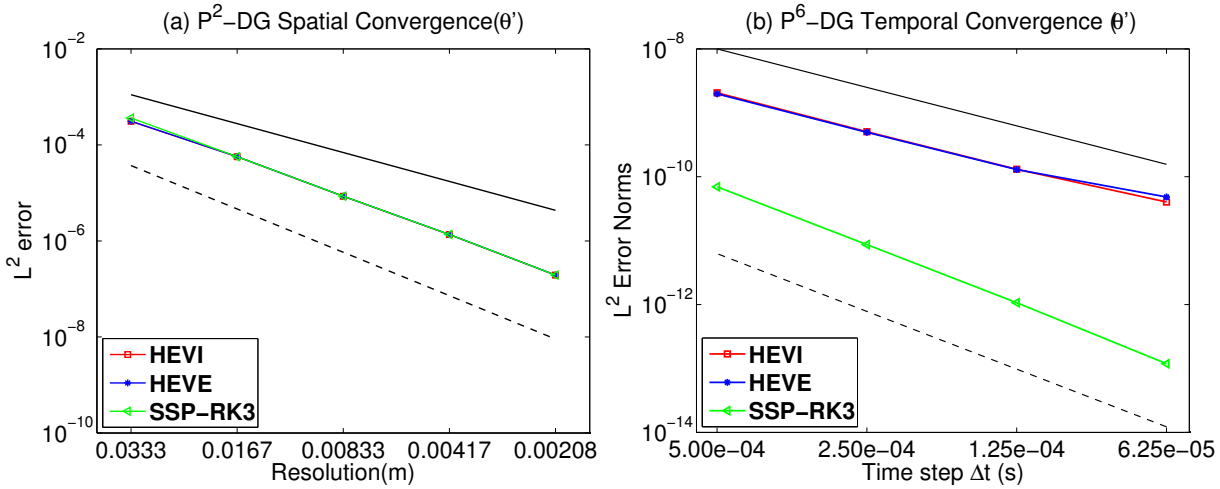

Figure 4.2: The convergence plots for traveling sine-wave test with grid-spacing $\Delta x = \Delta z$. (a) The h-convergence of P^2-DG, with the SSP-RK3, HEVI and HEVE integrators. (b) The t-convergence of P^6-DG, with SSP-RK3, HEVI and HEVE integrators. For both plots, the top solid line corresponds to the slope of second-order convergence and the bottom dash line denotes the slope of third-order convergence (see the text for the grid-spacing details).

4.4.2.2 Inertia-Gravity Wave Test

The non-hydrostatic inertia-gravity wave (IGW) test introduced by [80] serves as a useful tool to check the accuracy of various time-stepping schemes in a more realistic non-hydrostatic setting. This test case obtains the grid-converged solution without the need of a numerical diffusion. We use this experiment to test the accuracy of the HEVI schemes for our DG-NH model under different aspect ratio of grid resolutions. This test examines the evolution of a potential temperature perturbation θ', in a channel with periodic boundary conditions on the lateral boundaries. The initial perturbation (shown in Fig. 4.3(a)) radiates to the left and right symmetrically, while being advected to the right with a prescribed mean horizontal flow.

The parameters for the test are the same as the NH test reported in [80]. The Brunt-Väisälä

frequency is given as $N_f = 0.01$ s^{-1}, the upper boundary is placed at $z_T = 10$ km, the perturbation half-width is $a_m = 5$ km and the initial horizontal velocity is $u = 20$ m/s. The inertia-gravity waves are produced by an initial potential temperature perturbation (θ') of the form:

$$\theta' = \theta_c \frac{a_m^2 \sin(\pi z/h_c)}{a_m^2 + (x - x_c)^2}, \tag{4.44}$$

where $\theta_c = 0.01^\circ$ K, $h_c = 10$ km, $x_c = 100$ km. The (x, z) domain is defined to be $[0, 300] \times [0, 10]$ km^2, with no-flux boundary conditions at the top and bottom of the domain and periodic on the left and right sides. The IGW simulation is performed for $t_T = 3000$ s. For a moderate aspect ratio $\Delta x/\Delta z = 10$, the numerical solution after 3000 s is shown in Fig. 4.3(b), where the P^2 DG-NH model is integrated with SSP-RK3 time integrator for $\Delta t = 0.14$ s and $\Delta z = 160$ m. We have experimented with DG-NH model for various polynomial orders ($P^k, k = 2, 3, 4$) while fixing the resolution, however the simulated results are found to be very comparable.

To perform a qualitative comparison of the HEVI scheme versus the SSP-RK3 scheme, we test P^2-DG under two options of aspect ratio $\Delta x/\Delta z = 10, 100$, while fixing $\Delta x = 1600$ m. For SSP-RK3, the CFL stability is constrained by the $\min\{\Delta x, \Delta z\}$, which only allows $\Delta t = 0.14$ s for $\Delta z = 160$ m ($N_x = 63, N_z = 21$) and $\Delta t = 0.014$ s for $\Delta z = 16$ m ($N_x = 60, N_z = 200$). However, for the HEVI simulation, the CFL condition for the whole system is not dominated by the smaller grid-spacing Δz, permitting a larger timestep $\Delta t = 1.4$ s, regardless of the choice of Δz. In other words, the timestep of HEVI is 10 times the timestep of SSP-RK3 when $\Delta x/\Delta z = 10$ and 100 times when $\Delta x/\Delta z = 100$. Figure 4.3(c,d) show the difference field of the solution (i.e., SSP-RK3 solution minus HEVI solution), when $\Delta x/\Delta z = 10, 100$, respectively. It is observed that the difference is two orders of magnitude smaller than that of θ', and the difference field of $\Delta x/\Delta z = 10$ (Fig. 4.3(c)) is slightly less noisy than that of $\Delta x/\Delta z = 100$ (Fig. 4.3(d)). For both horizontal-vertical aspect ratios, the range of the potential temperature perturbation is $\theta' \in [-1.52 \times 10^{-3}, 2.79 \times 10^{-3}]$ (K), which is fairly close to the results of [27, 47].

In order to capture the spatial convergence of the HEVI scheme, we test P^2-DG under two options of aspect ratio $\Delta x/\Delta z = 10, 100$. Since there is no analytic solution available for this test-

case, the reference solution is chosen from the high-resolution solution of SSP-RK3 with $\Delta x = 200$ m and $\Delta t = 0.0175$ s when $\Delta x = 10\Delta z$ or $\Delta t = 0.00175$ s when $\Delta x = 100\Delta z$. Figure 4.4(a,c) show the convergence rate of the HEVI scheme as well as SSP-RK3 scheme in a range of horizontal resolutions $\{400, 800, 1600, 3200\}$ (m) for $\Delta x = 10\Delta z$ and $\Delta x = 100\Delta z$ respectively. For SSP-RK3 scheme, $\Delta t = 0.035$ s when $\Delta x = 10\Delta z$ and $\Delta t = 0.0035$ s when $\Delta x = 100\Delta z$ for $\Delta x = 400$ m. For HEVI scheme, since the timestep for HEVI is only limited by the horizontal grid-spacing, $\Delta t = 0.35$ s when $\Delta x = 400$ m, irrelevant of the vertical resolution. For other choices of Δx, Δt scales with Δx linearly. Both Fig. 4.4(a,c) show third-order convergence of both schemes at a relatively lower resolution, which is anticipated for a P^2-DG scheme, but the HEVI scheme shows gradually degraded convergence rate at a relatively higher resolution ($\Delta z = 40$ m in Fig. 4.4(a) and $\Delta z = 4$ m in Fig. 4.4(c)), which may result from the splitting error.

We sample θ' (K) horizontally along $z = 5$ km, as displayed in Fig. 4.4(b) for $\Delta x = 10\Delta z$ and Fig. 4.4(d) for $\Delta x = 100\Delta z$. In both plots, the distribution is symmetric with respect to the point ($x = 160$ km), which agrees well with the theory, since the horizontal wind ($u = 20$m/s) moves the whole field 60 km to the right after 3000 s. It is observed that the HEVI scheme captures fine features of the IGW as the resolution goes higher, while allowing relatively larger Δt, as compared to the SSP-RK3 scheme. This result is also consistent with those reported in [27], where a high-order ($k = 8$) DG model was used, and by other recent FV results given in [2, 47, 61]. In addition, there is no visible difference in the convergence rate and the horizontal sampling of θ' for different aspect ratios of horizontal resolution and vertical resolution. This validates our dimensional splitting and assures us that the choice of a higher aspect ratio of grid resolutions does not sacrifice the quality of the numerical solution.

4.4.2.3 Rising convective thermal bubble

The convective bubble test-case embodies a phenomenon of great interest to mesoscale type flows, and is widely used to validate the ability of numerical models for simulating the atmospheric motions due to thermodynamic effects [94]. The thermal bubble is warmer than the ambient air

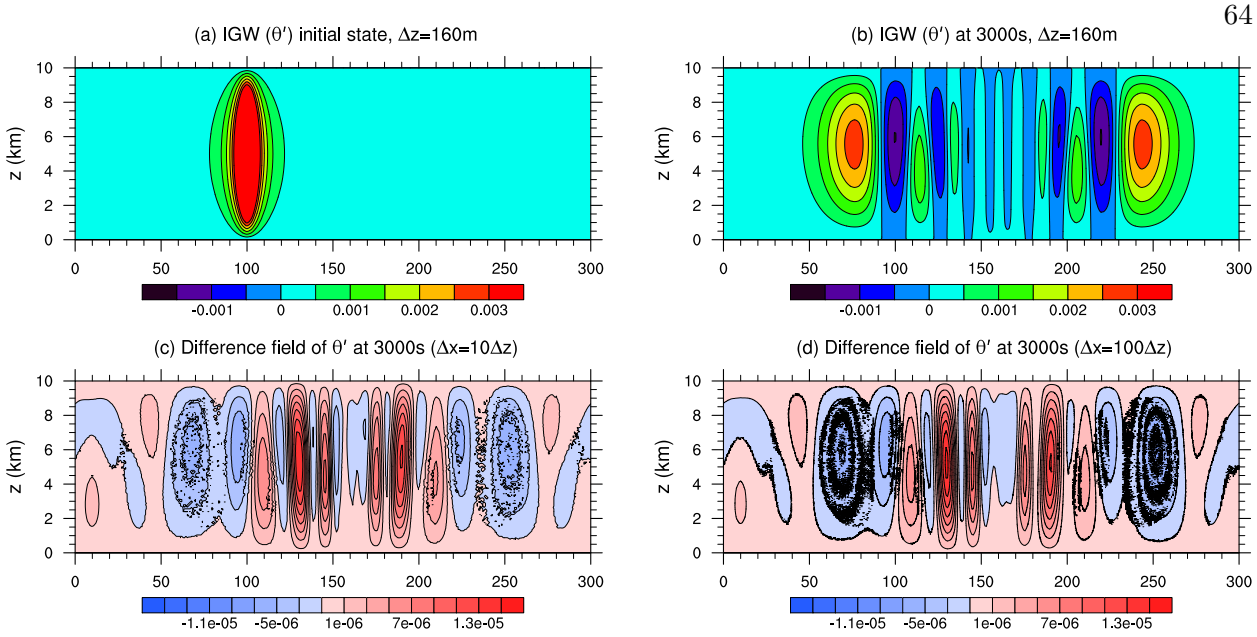

Figure 4.3: Numerical solutions (potential temperature perturbation θ') with the IGW test at different aspect ratios $\Delta x/\Delta z = 10$, 100. The P^2-DG scheme with time integrators SSP-RK3 and HEVI schemes are used for the simulation, where Δx is fixed at 1600 m. (a) Initial state of θ' (K) when $\Delta x/\Delta z = 10$, (b) contour plots of θ' (K) at 3000 s, using SSP-RK3 with $\Delta t = 0.14$ s and $\Delta x/\Delta z = 10$. (c) The difference fields of θ' between SSP-RK3 and HEVI with $\Delta x/\Delta z = 10$, $\Delta t = 0.14$ s using SSP-RK3, $\Delta t = 1.4$ s using HEVI. (d) Same as in (c) but for $\Delta x/\Delta z = 100$ and $\Delta t = 0.014$ s using SSP-RK3.

and thus it rises while deforming as a result of the shearing motion, caused by the velocity field gradients until it forms into the shape of a mushroom cloud. The convective thermal bubble uses a hydrostatic balance with a uniform potential temperature, $\theta_0 = 300$ K. The following perturbation is added to hydrostatic background θ_0:

$$\theta'(x,z) = \Delta\theta \max(0, 1 - d/r), \quad d(x,z) = \sqrt{(x-x_0)^2 + (z-z_0)^2}, \tag{4.45}$$

where d is the distance from the center to the bubble. Other parameters for this test are the radius of the bubble $r = 2$ km, $x_0 = 10$ km, $z_0 = 2$ km, and $\Delta\theta = 2$ K. The model domain is $[0, 20] \times [0, 10]$ km^2, and the horizontal and vertical wind are both initialized to zero. No-flux boundary conditions are used along all boundaries. The numerical simulation is performed for $t_T = 1000$ s.

The evolution process in the bubble convection test is more vigorous as opposed to IGW

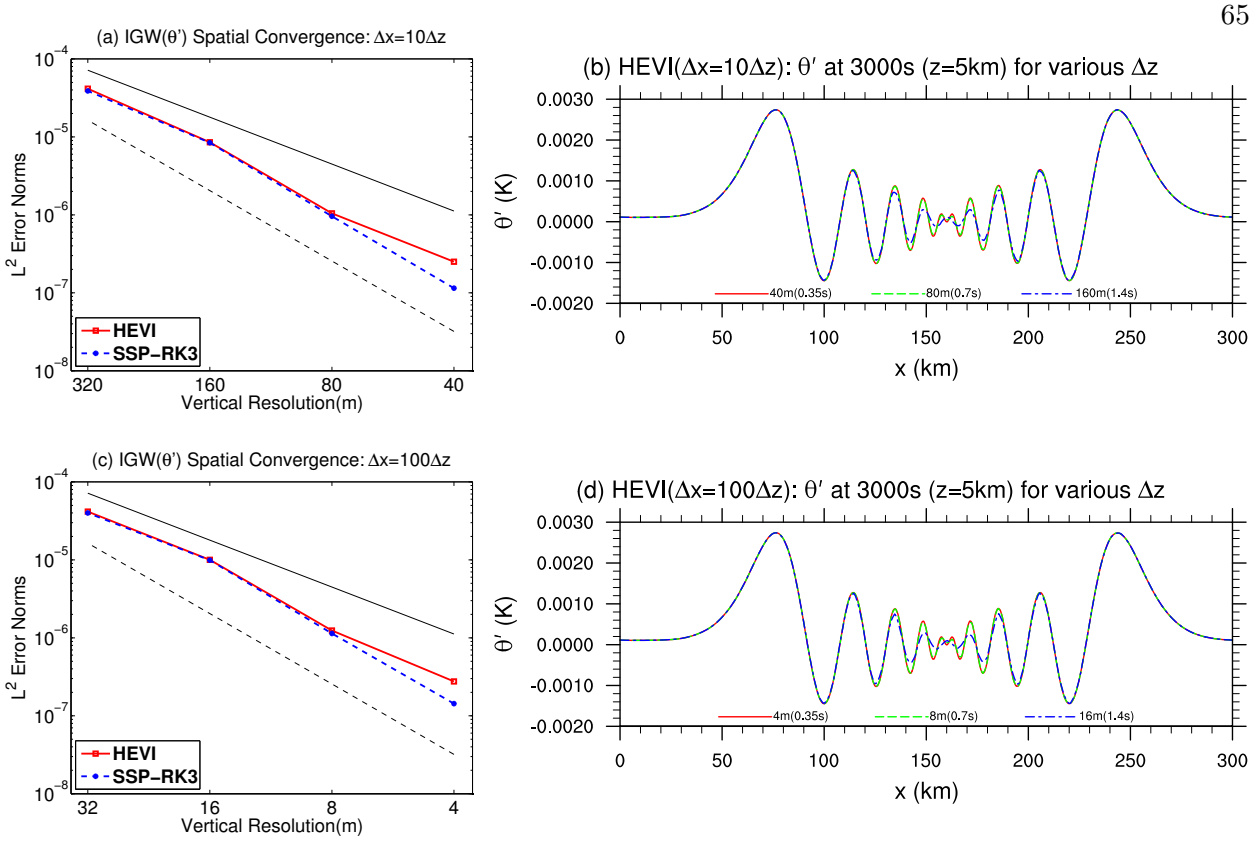

Figure 4.4: Spatial convergence of L^2 error for the P^2-DG model employing IGW test with the time integrators HEVI and SSP-RK3, using the aspect ratios $\Delta x/\Delta z = 10$ and 100. Panels (a) and (c) show the spatial convergence when $\Delta x/\Delta z = 10$ and 100, respectively. The top solid-line and the bottom dashed-line correspond to slopes of second- and third-order convergence, respectively. Panels (b) and (d) show the potential temperature perturbation θ' (K) sampled at $z = 5$ km, at various vertical resolutions for the HEVI simulations. The timestep size for each resolution is shown in the parenthesis.

test. A uniform grid $\Delta x = \Delta z$ is chosen for this test-case, irrelevant of the grid resolution. There is no obvious benefit for HEVI-DG over RK-DG since the same Δt is used for both schemes. The motivation of experimenting on this test-case is to validate the robustness of the dimensional splitting, when there are strong evolutions and vigorous interactions throughout the whole domain. We tested the accuracy of the HEVI time-stepping scheme in the P^3 DG-NH model with a grid-spacing of $\Delta z = 125$ m, employing 20×10 elements. The potential temperature perturbations at 1000 s are contoured in the upper panel of Fig. 4.5. The time step $\Delta t = 0.04$ s used for the simulation with the P^3 DG-NH model. Minor oscillations can be observed, which is typical for

any high-order method without a diffusive or dissipative mechanism [47]. However, when an LDG type second-order diffusion is switched on with a diffusion coefficient $\nu = 12$ m^2 s^{-1}, the small scale noises are greatly reduced, and the fine-scale structures of the mushroom cloud and the sharp gradient are captured, as seen in the lower panel of Fig. 4.5. Figure **??** shows the wind field with the same test without numerical diffusion. The right columns shows the difference field and we observe that the difference between RK-DG and HEVI-DG solutions. The magnitude of the difference field is small ($\mathcal{O}(10^{-3})$) and is only about 0.25% of the original wind field, which is fairly small.

HEVI-DG can adequately capture the nice features of the strenuous evolving thermal dynamics and reproduce comparable results of RK-DG for 2D Euler system.

4.4.2.4 Density current test (Straka test)

The density current benchmark introduced by [83] is often used to evaluate numerical schemes developed for atmospheric models. The Straka density current mimics the cold outflow from a convective system and tests a model's ability to control oscillations when run with numerical viscosity. This test involves evolution of a density flow generated by a cold bubble in a neutrally stratified atmosphere. The cold bubble descends to the ground and spreads out in the horizontal direction, forming three Kelvin-Helmholtz shear instability rotors along the cold front surface. This is a test-case suitable for testing the LDG diffusion option in our DG-NH model.

The test case uses a hydrostatically balanced basic state on a uniform potential temperature, $\theta_0 = 300$ K, and adds the following perturbation in potential temperature:

$$\theta(x,z) = \begin{cases} \theta_0, & \text{if} \quad L(x,z) > 1, \\ \theta_0 + \Delta\theta \left[\cos\left(\pi L(x,z)\right) + 1\right]/2 & \text{otherwise}, \end{cases} \tag{4.46}$$

where $L(x,z) = \sqrt{\left(\frac{x-x_0}{x_r}\right)^2 + \left(\frac{z-z_0}{z_r}\right)^2}$, $\Delta\theta = -15$ K, $(x_r, z_r) = (4, 2)$ km, and $(x_0, z_0) = (0, 3)$ km. Non-flux boundary conditions are applied for all four boundaries. A dynamic viscosity of $\nu = 75$ m^2 s^{-1} is used for the diffusion [83]. The diffusion terms are treated with the LDG approach. The model is integrated for 900 s on a domain $[-26.5, 26.5] \times [0, 6.4]$ km^2.

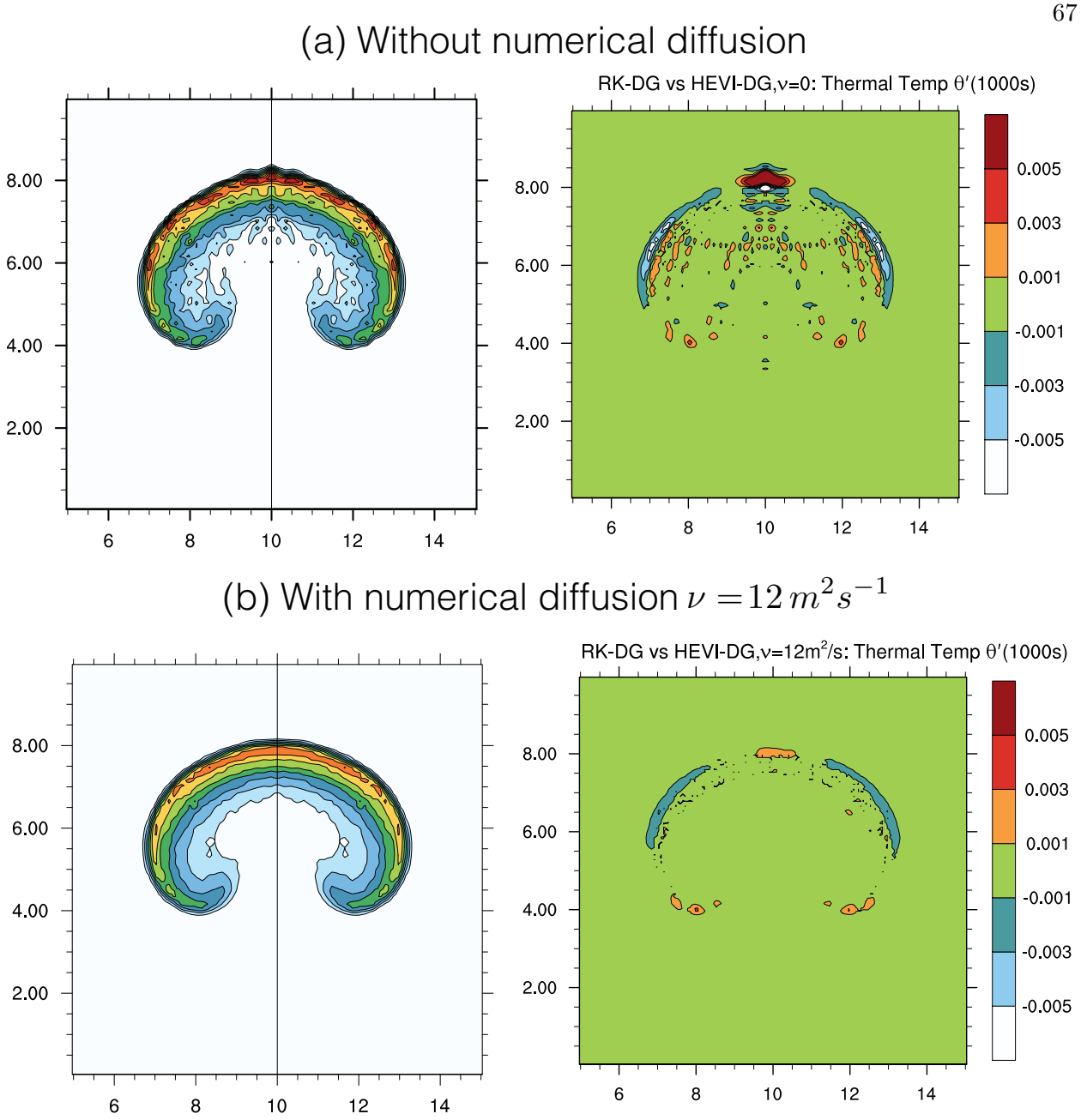

Figure 4.5: Potential temperature perturbations θ' (K) at a uniform resolution 125 m (left column) for convective thermal bubble test after 1000s using RK-DG model. The right column shows the difference field (RK-DG solution minus HEVI-DG solution), produced with the P^3 DG-NH model. The result shown in the upper panel is without any numerical diffusion, and the lower panel is that with a numerical diffusion $\nu = 12\,m^2 s^{-1}$.

For an equidistant grid ($\Delta x = \Delta z$) there is no particular advantage for HEVI-DG over RK-DG in terms of efficiency, unless $w > u$. The simulated potential temperature θ' (K) after 900 s for

the Straka density current is shown in Fig. 4.6(a-d), with the grid resolution successively halved from 200 m to 25 m. The timestep is $\Delta t = 0.16$ s for 200 m grid resolution and decreases linearly with the grid spacing. The results shown are with the P^2 version of the DG-NH model. This test was repeated with the high-order ($P^k, k = 3, 4$) spatial discretization with a similar resolution, and the results were visually indistinguishable, showing an acceptable grid convergence. It is observed that three Kelvin-Helmholtz rotors develop as the grid resolution is refined. The numerical results are comparable to other published results [2, 47, 61], despite different contour values. This test verifies the LDG second-order diffusion in an operator-split configuration.

Figure 4.6(e) gives the horizontal profile of the potential temperature perturbation θ' sampled along $z = 1.2$ km at the same set of the grid spacings as in Fig. 4.6(a-d). The three valleys in the right panel of Fig. 4.6(e) correspond to the three Kelvin-Helmholtz rotors in Fig. 4.6(a-d). As the resolution goes higher, more fine features of the current are captured reflecting the multi-scale nature of the flow. Our results agree well with the multimoment FV method [47] and high-order DG method [27]. In order to compare the performance of HEVI and SSP-RK3, the profile of potential temperature perturbation along $z = 1.2$ km for $\Delta z = 100$ m is shown in Fig. 4.6(f). The result of the HEVI scheme is visually in line with that of SSP-RK3, which demonstrates the robustness of the HEVI-DG combined with the LDG diffusion.

4.4.2.5 Schär mountain test

We consider the Schär mountain test [75] to evaluate the performance of our HEVI scheme in handling complex topography. The Schär mountain test simulates the generation of gravity waves by a constant horizontal flow field in a uniform stratified atmosphere impinging on a non-uniform mountain range. The profile of the mountain range is given as,

$$h(x) = h_0 \exp\left(-\frac{x^2}{a_0^2}\right) \cos^2\left(\frac{\pi x}{\lambda}\right), \tag{4.47}$$

where $h_0 = 250$ m, $a_0 = 5000$ m, and $\lambda = 4000$ m. The terrain-following, height-based coordinate (A.7) takes effect in this test case and is shown in Fig. 4.7(a). The gravity waves are

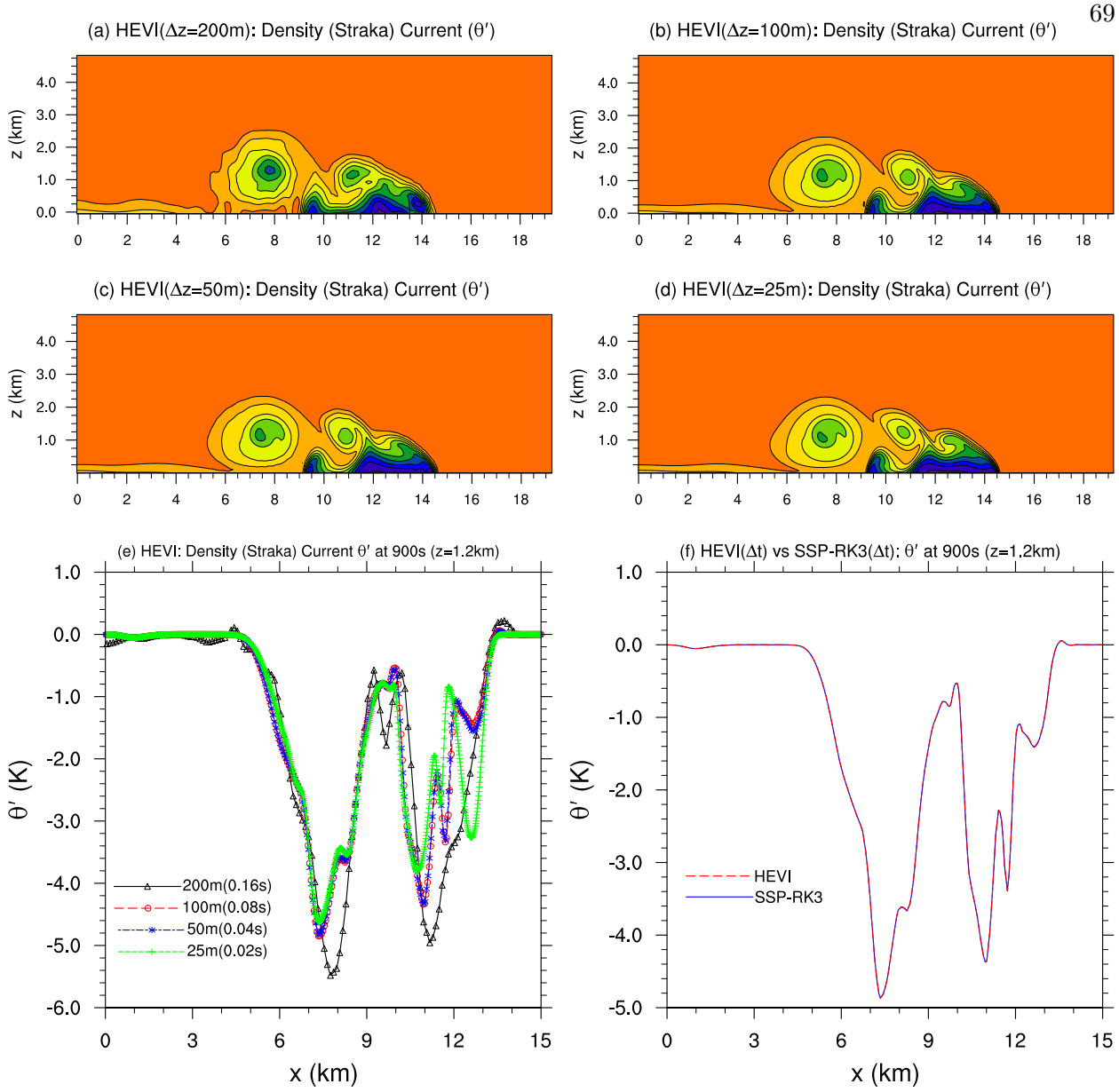

Figure 4.6: The plots of potential temperature perturbation θ' (K) for the Straka density current test on a uniform grid $\Delta x = \Delta z$ with P^2-DG schemes for 900 s integration. (a-d) display the contour plots of θ' using HEVI in a range of resolutions from 200 m to 25 m. Timestep $\Delta t = 0.16$ s for 200 m grid resolution, and is otherwise proportional with the grid resolution. The contour values (K) are in the range of $[-9.5, 0.5]$ with an increment 1.0. The sampling of θ' at $z = 1.2$ km are shown in the bottom panels, where (e) shows the plots corresponding to the resolutions as used in (a-d), and the associated timestep is given in the parenthesis. (f) compares HEVI and SSP-RK3 schemes at a resolution of 100 m.

composed of two major spectral components: the large-scale hydrostatic waves propagate deeply

in the vertical, while the small-scale non-hydrostatic waves decay rapidly as the altitude increases.

The initial state of the atmosphere has a constant horizontal flow of $u_0 = 10$ m/s and the Brunt-Väisälä frequency is $N_f = 0.01$ s^{-1}. The reference potential temperature $\overline{\theta}$ can be computed from (4.39) using $\theta_0 = 280$ K. The simulation is carried out in the domain of $[-25, 25] \times [0, 21]$ km^2. No-flux boundary conditions are imposed at the bottom boundary and non-reflecting boundary conditions are used along the top, left and right boundaries. The sponge-layers are placed in the region of $\zeta \geq 9$ km with $\tau_{top} = 0.28$ for the top boundary and $|x| \geq 15$ km with $\tau_{lat} = 0.18$ for the lateral outflow boundaries. P^3-DG is used and the grid resolution is chosen as $\Delta x = 250$ m and $\Delta\zeta = 105$ m ($N_x = 50, N_z = 50$), which leads to $\Delta x/\Delta\zeta \approx 2$. We used a different aspect ratio as the one used in [27, 47, 91] where $\Delta x/\Delta\zeta \approx 1$), because this makes HEVI scheme more challenging. The simulation time is $t_T = 10$ h (36000 s) with $\Delta t = 0.125$ s for the HEVI scheme and $\Delta t = 0.065$ s for the SSP-RK3 scheme. Figure 4.7(b,c) show the contours of the horizontal and vertical wind fields at 10 h in the region $[-10, 10] \times [0, 10]$ km^2 for visualization. No visually distinguishable difference is observed between the results of SSP-RK3 scheme and HEVI scheme. There is no unphysical distorted wave pattern shown in the upper level of the domain, and our results comparable to the other publications [27, 47, 91]. In addition, our handling of the complex domain does not introduce spurious noise, as discussed in [42].

To increase the the orographic effects, the height of the mountain in the Schär test is increased to $h_0 = 750$ m, so that the maximum slope for the mountain is about 55% [76]. The purpose of this test is make a close comparison between HEVI and SSP-RK3 in a relatively extreme case. The grid resolution and boundary conditions for this experiment remain the same as in the Schär test, and the model is integrated for a short period of $t_T = 1800$ s, with HEVI as well as SSP-RK3 schemes. The terrain-following coordinate is shown in Fig. 4.7(d), which is more curved (with sharp gradients) than the case shown in Fig. 4.7(a). For the HEVI scheme $\Delta t = 0.125$ s, which is twice the Δt used for SSP-RK3 scheme. The vertical wind field is shown in Fig. 4.7(e,f) for the HEVI and SSP-RK3 schemes respectively. The vertical wind field is virtually indistinguishable between the HEVI and SSP-RK3 schemes, with maximum absolute vertical velocities of 6.45 m/s and 6.44

m/s, respectively. This again shows that the HEVI type dimensional splitting scheme permits a larger timestep and it does not introduce additional noise, even in an extreme case, and the results are comparable to that with SSP-RK3 scheme. Although our experimental setup including the boundary conditions and grid resolution are different, the vertical wind fields shown in Fig. 4.7(e,f) is similar to the corresponding Fig.3 of [76].

4.5 Summary and Conclusions

We have proposed a **moderate order** discontinuous Galerkin non-hydrostatic (DG-NH) model based on the compressible Euler equations in a 2D (x, z) Cartesian plane, with a simple operator-splitting time integration scheme. The model uses a terrain-following height-based coordinate to handle the orography. For the atmospheric simulation on the non-hydrostatic scale, a high aspect ratio between the horizontal and vertical spatial discretization imposes a stringent restriction on the explicit timestep size for the Euler system. To alleviate the dominant effect due to large horizontal-vertical aspect ratio, the so-called **horizontally explicit and vertically implicit** (HEVI) scheme via the Strang-splitting is proposed and studied in our DG-NH model. The HEVI time-integration scheme avoids the tiny timestep limitations, inflicted by the vertical grid spacing ($\Delta z \ll \Delta x$), and therefore the overall CFL restriction on the timestep is mainly determined by the horizontal grid spacing (Δx).

The accuracy of our HEVI DG-NH model is tested under a suite of NH benchmark test cases. The numerical results, which are in agreement with those in literature, show that the HEVI scheme is robust and capable of relaxing the CFL constraint to the horizontal grid spacing and yields accurate simulations, even though the vertical grid spacing is greatly smaller than the horizontal ($\Delta x/\Delta z = 10, 100$). As expected, a second-order temporal convergence is observed with the HEVI scheme, and a third-order spatial convergence is obtained with the HEVI scheme as well as the SSP-RK3 scheme, which is consistent with the P^2-DG discretization. We have also implemented an LDG-type second-order diffusion in a dimension-split manner to be consistent with the HEVI formulation. The LDG diffusion effectively eliminates the small-scale noise for the model and

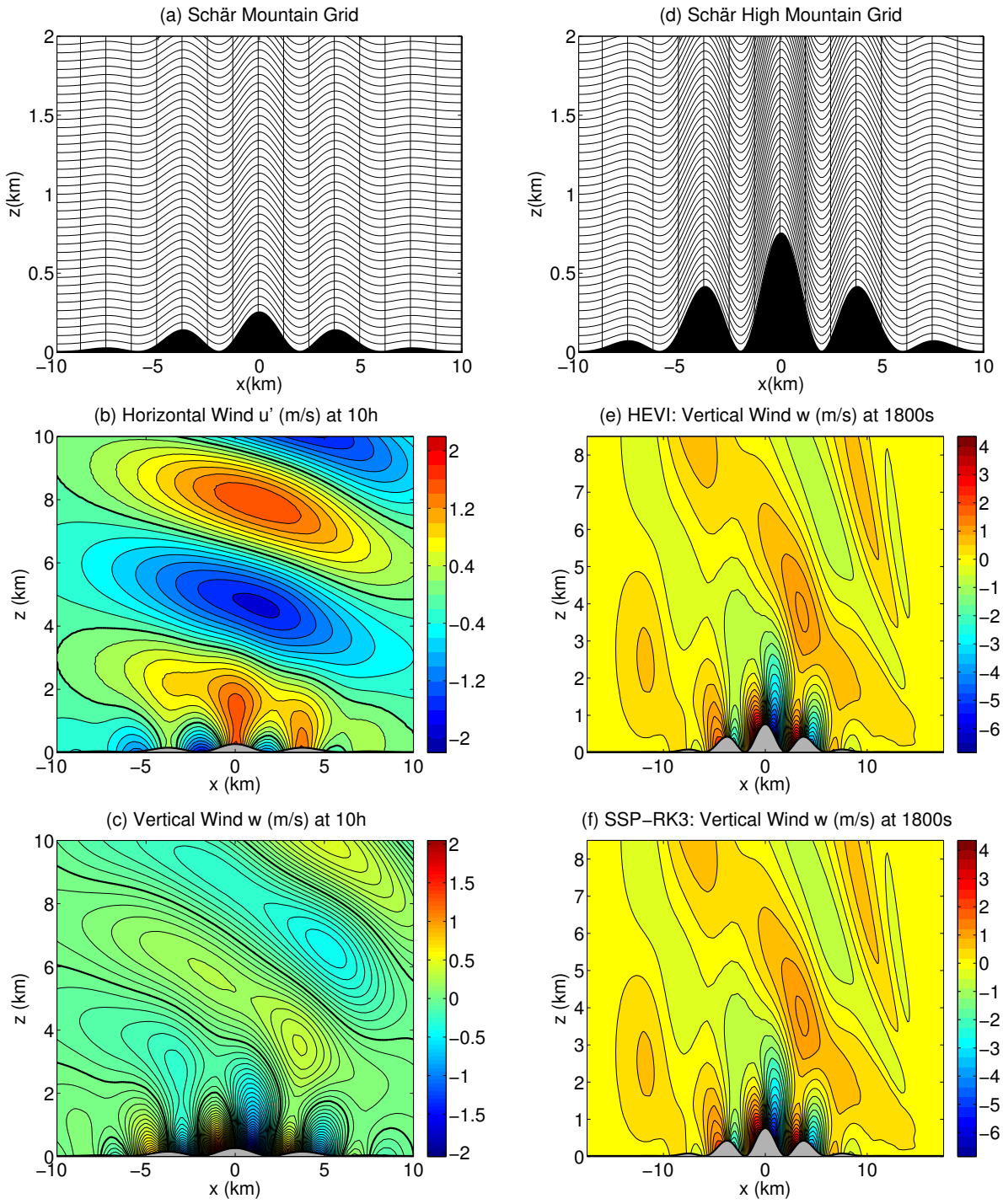

Figure 4.7: Numerical results with P^3-DG model combined with HEVI scheme for the Schär mountain test. The mountain profiles and elements are shown in (a) with $h_0 = 250$ m, and (d) with $h_0 = 750$ m. The domain is $[-25, 25] \times [0, 21]$ km^2 with grid spacing $\Delta x = 250$ m and $\Delta\zeta = 105$ m. The bottom panels on the left column show the contour plots (zero contour is highlighted by a thicker line) of wind fields after 10 h of simulation with $\Delta t = 0.125$ s. (b) Horizontal wind field perturbation u' (m/s), with a contour increment 0.2 m/s, and (c) vertical wind field w (m/s), with a contour increment 0.05 m/s. The bottom panels of the right column show vertical wind field w (m/s) with a contour increment 0.3 m/s, (e) for HEVI scheme and (f) for SSP-RK3 scheme.

stabilizes the flow field, as is shown in the Straka density current test. Moreover, in the presence of orography (Schär mountain test), no spurious wave pattern or noise is detected from the results of our HEVI scheme, and the numerical simulation is visually identical to that of the SSP-RK3 scheme.

The HEVI scheme is a practical option and competitive approach for global NH atmospheric modeling, since the existing solver of the horizontal dynamics can be greatly recycled as done in a typical split-explicit case when implemented in a full 3D domain. Here we demonstrate that it is a viable option for the high-order DG method as well. However, the efficiency of the HEVI scheme mainly depends on the performance of the 1D implicit solver. Proper preconditioning is a possible remedy for accelerating the Newton-Krylov Jacobian-free solver, and work in this direction is progressing. Our ultimate goal is to implement the HEVI-DG formulation in the High-Order Method Modeling Environment (HOMME) developed at NCAR, to extend it as a NH framework. The attractive features of HOMME (excellent parallel efficiency) can be exploited for the resulting NH dynamical core when HEVI-DG scheme is implemented. Further investigation will be continued on the application of the HEVI time-split scheme in the HOMME framework.

Chapter 5

IMEX Runge-Kutta schemes in the HEVI context

When applied to some partitioned problem, or split problem, Runge-Kutta methods are sometimes referred to as Additive Runge-Kutta (ARK). We consider a special type of ARK scheme, where the part of the system is solved explicitly and the rest is solved implicitly, the so-called Implicit-explicit (IMEX) scheme. The crucial part is to use two different integrators for the nonstiff and the stiff terms, respectively. In this chapter, we will examine different IMEX-RK schemes and compare two approaches to decompose the whole system: linear-nonlinear splitting and operator splitting.

5.1 Implicit-explit (IMEX)-Runge-Kutta schemes

After apply the DG spatial discretization to the governing equations, we obtain the ODE system:

$$\frac{\partial \mathbf{q}}{\partial t} = \mathbf{F}(\mathbf{q}), \tag{5.1}$$

where $\mathbf{q}(t)$ denotes the state variables.

In order to relax the stringent CFL condition resulted from the large aspect ratio between horizontal and vertical resolution, in the context of atmospheric modeling, we usually split the system into two parts:

$$\mathbf{q}' = f(\mathbf{q}, t) + g(\mathbf{q}, t), \tag{5.2}$$

The time-scales associated with $f(\mathbf{q}, t)$ are relatively long, while those associated with $g(\mathbf{q}, t)$ can be very short. As a consequence, f represents the non-stiff term, which is solved explicitly, whereas

g represents the stiff term, which is solved implicitly.

Given that $\mathbf{q}(t)$ at time t_n is called $\mathbf{q}_n$, to advance from time t_n to t_{n+1}, an Implicit-Explicit (IMEX) RK scheme takes the form

$$\mathbf{Q}_i = \mathbf{q}_n + \Delta t \sum_{j=1}^{i-1} \tilde{a}_{ij} f(\mathbf{Q}_j, t_0 + \tilde{c}_j \Delta t) + \Delta t \sum_{j=1}^{i} a_{ij} g(\mathbf{Q}_j, t_0 + c_j \Delta t), \quad i = 1, 2, \ldots, s \tag{5.3}$$

$$\mathbf{q}_{n+1} = \mathbf{q}_n + \Delta t \sum_{i=1}^{s} \tilde{b}_i f(\mathbf{Q}_i, t_0 + \tilde{c}_i \Delta t) + \Delta t \sum_{i=1}^{s} b_i g(\mathbf{Q}_i, t_0 + c_i \Delta t), \tag{5.4}$$

where $\tilde{A} = (\tilde{a}_{ij})_{s\times s}$, $\tilde{a}_{ij} = 0, \quad j \geq i$, and $A = (a_{ij})_{s\times s}$ are lower triangular matrices, while $\tilde{\mathbf{c}}, \tilde{\mathbf{b}}, \mathbf{c}, \mathbf{b} \in R^s$ are s-dimensional vectors. The IMEX-RK schemes are usually defined by a double Butcher *tableau*:

$$\begin{array}{c|c} \tilde{\mathbf{c}} & \tilde{A} \\ \hline & \tilde{\mathbf{b}}^T \end{array}, \qquad \begin{array}{c|c} \mathbf{c} & A \\ \hline & \mathbf{b}^T \end{array}$$

The IMEX-RK schemes can be constructed by combining an explicit RK scheme with an implicit RK scheme. The implicit scheme is usually chosen as the diagonally implicit Runge-Kutta (DIRK) scheme, i.e. $a_{ij} = 0, j > i$. In addition, it is desired that $a_{ii} = \lambda$, for $i = 1, 2, \ldots, s$, which is the so-called Single DIRK (SDIRK) scheme. Kennedy et. al. [39] also use an ESDIRK scheme for the implicit scheme, where they differ from the traditional SDIRK scheme by having the first stage explicit, i.e. $a_{11} = 0$. The fact that the implicit scheme is diagonally implicit (DIRK) and identical diagonal term makes the implementation of IMEX simpler, and ensures f is effectively explicitly computed.

In [5], Ascher et al. gave the condition on how implicit RK scheme and explicit RK scheme can be combined to create stable schemes where the overall schemes are second-, third-order accurate, under the requirement that $\mathbf{c} = \tilde{\mathbf{c}}^T$. Ascher et al. described the schemes that are stiffly accurate, i.e. accurate in the limit that fast term is infinitely fast. For the wave equations and fluid-flow, this corresponds to finding accurate solutions for the slow modes while suppressing modes that are too fast to be resolved. In the context of atmospheric modeling, this means resolving Rossby waves and the slower gravity waves accurately, whereas damping acoustic and fast gravity waves [93]. It is required that $(a_{si}) = b_i, i = 1, 2, \ldots, s$, i.e. the last row of A equals to $\mathbf{b}^T$ for the implicit

scheme to be stiffly accurate. For very stiff problems, it suggests that $(\tilde{a}_{si}) = \tilde{b}_i, i = 1, 2, \ldots, s$ in addition. In this way, the numerical solution for the next time level equals to the last stage value. Parechi and Russo [62] derived more IMEX-RK schemes and tested them on advection-diffusion equations. Their schemes are asymptotically accurate (the order of accuracy is maintained in the stiff limit), which does not require $\mathbf{c} = \tilde{\mathbf{c}}^T$, as opposed to [5]. The schemes in [5] and [62] were "strong-stability preserving" (SSP) (a given norm of the solution does not increase) and designed to damp high wave-numbers, unlike the trapezoidal scheme, which preserves the power in all wave-numbers. Kennedy and Carpenter [39] proposed some third- to fifth-order accurate ARK schemes for convection-diffusion-reaction equations and discussed some numerical properties for various ARK schemes, such as stiffness leakage and order-reduction. In [25], Giraldo et al. proposed a new, second-order accurate ARK scheme and suggested that $\mathbf{b} = \tilde{\mathbf{b}}$ is a necessary condition for the conservation of integral invariants, such as mass and energy.

Following the convention of [5], we name the schemes as [name]k(s,σ,p) where k is the order of the explicit scheme, s is the number of implicit stages, σ is the number of explicit stages and p is the order of the whole scheme. We choose some IMEX schemes due to their popularity in atmospheric modeling. The IMEX schemes we choose are given in the following double Butcher tableau:

$$ARS2(2,2,2): \quad \begin{array}{c|ccc} 0 & 0 & 0 & 0 \\ \gamma & \gamma & 0 & 0 \\ 1 & \delta & 1-\delta & 0 \\ \hline & \delta & 1-\delta & 0 \end{array} \qquad \begin{array}{c|ccc} 0 & 0 & 0 & 0 \\ \gamma & 0 & \gamma & 0 \\ 1 & 0 & 1-\gamma & \gamma \\ \hline & 0 & 1-\gamma & \gamma \end{array}, \quad \gamma = 1 - \frac{\sqrt{2}}{2}, \quad \delta = 1 - 1/(2\gamma)$$

$$ARK2(2,3,2): \quad \begin{array}{c|ccc} 0 & 0 & 0 & 0 \\ 2\gamma & 2\gamma & 0 & 0 \\ 1 & 1-\alpha & \alpha & 0 \\ \hline & \delta & \delta & \gamma \end{array} \qquad \begin{array}{c|ccc} 0 & 0 & 0 & 0 \\ 2\gamma & \gamma & \gamma & 0 \\ 1 & \delta & \delta & \gamma \\ \hline & \delta & \delta & \gamma \end{array}, \quad \begin{array}{l} \gamma = 1 - \frac{\sqrt{2}}{2}, \quad \alpha = \frac{1}{6}(3 + 2\sqrt{2}), \\ \delta = \frac{1}{2\sqrt{2}} \end{array}$$

$$ARS3(2,3,3):\quad \begin{array}{c|ccc} 0 & 0 & 0 & 0 \\ \gamma & \gamma & 0 & 0 \\ 1-\gamma & \gamma-1 & 2(1-\gamma) & 0 \\ \hline & 0 & 1/2 & 1/2 \end{array},\quad \begin{array}{c|ccc} 0 & 0 & 0 & 0 \\ \gamma & 0 & \gamma & 0 \\ 1-\gamma & 0 & 1-2\gamma & \gamma \\ \hline & 0 & 1/2 & 1/2 \end{array},\quad \gamma = \frac{3+\sqrt{3}}{6}$$

The Strang-splitting considered in Chapter 4 uses SSP-RK3 as the explicit solver and Trapezoidal rule (or Crank-Nicolson) as the implicit solver. The traditional Strang-splitting requires two explicit solve to update each time-step. This is acceptable in the 2D case, as the problem size is relatively small. However, for the full 3D NH models, the problem size increases dramatically. When the horizontal domain decomposition is employed, two explicit solves can be costly and it may introduce some communication overhead to the model and potentially impede the computational efficiency. The other option, the V-H-V sequence, in contrast required one explicit solve and two implicit solve. In general, the implicit solve needs more flops of operations than the explicit solve. Therefore, it is difficult to decide which option is superior in terms of the computational cost and the parallel efficiency. As suggested by Ullrich et. al. [91], we can use a modified sequence of V-H-V named Strang carryover, where the first implicit stage at the new time-step can reuse the last implicit stage from the previous time-step. Strang-carryover only needs one implicit solve and one explicit solve (we count SSP-RK3 as one explicit solve) per time-step. Since both schemes are at least second-order accurate, the overall scheme will maintain second-order accuracy. We use Strang-splitting to denote Strang-carryover for consistency hereafter. Strang-splitting can also be viewed as a special type of IMEX-RK scheme, defined as the following double Butcher tableau [93],

$$Strang3(1,3,2):\quad \begin{array}{c|cccccc} 0 & 0 & 0 & 0 & 0 & 0 & 0 \\ 0 & 0 & 0 & 0 & 0 & 0 & 0 \\ 1 & 0 & 1 & 0 & 0 & 0 & 0 \\ 1/2 & 0 & 1/4 & 1/4 & 0 & 0 & 0 \\ 1 & 0 & 1/6 & 1/6 & 2/3 & 0 & 0 \\ 1 & 0 & 1/6 & 1/6 & 2/3 & 0 & 0 \\ \hline & 0 & 1/6 & 1/6 & 2/3 & 0 & 0 \end{array},\quad \begin{array}{c|cccccc} 0 & 0 & 0 & 0 & 0 & 0 & 0 \\ 1/2 & 1/2 & 0 & 0 & 0 & 0 & 0 \\ 1/2 & 1/2 & 0 & 0 & 0 & 0 & 0 \\ 1/2 & 1/2 & 0 & 0 & 0 & 0 & 0 \\ 1/2 & 1/2 & 0 & 0 & 0 & 0 & 0 \\ 1 & 1/2 & 0 & 0 & 0 & 0 & 1/2 \\ \hline & 1/2 & 0 & 0 & 0 & 0 & 1/2 \end{array}.$$

As mentioned by Pareshi and Russo [62] and proved by Jin [36], the conventional Strang-splitting method in general degenerates to first order in the limit $\epsilon \to 0$ for the hyperbolic relaxation systems

$$\frac{\partial \mathbf{Q}}{\partial t} + \mathbf{A}(\mathbf{Q})\frac{\partial \mathbf{Q}}{\partial x} = \frac{1}{\epsilon}\mathbf{R}((\mathbf{Q})).$$

However, this limit may never be fully reached for our particular applications.

Some of the remarks on the considered scheme are mentioned below [49]:

- ARS2(2,2,2) has only two explicit stages. The rest schemes has three or more explicit stages. In [9], ARS2(2,2,2) is studied with the IMEX splitting and DG spatial discretization. But some instability is observed when the horizontal grid spacing is much wider than the vertical and Sebastien et al. suggested some stabilization mechanism to match the order of the pressure gradient to the source term.

- Both ARS2(2,2,2) and Strang3(1,3,2) end with an implicit stage. The other two schemes end with an explicit stage. They are stiffly accurate under the definition of stiffly accurateness in [5].

- The explicit component of ARS3(2,3,3) is not SSP since $\tilde{a}_{31} < 0$. All the rest schemes have SSP explicit components.

- Strang3(1,3,2) is a fully splitting scheme, as it does not update the explicit part and implicit part at the same stage (i.e. either the explicit component or the implicit component is updated in a stage).

5.2 Decomposition of the system

For the resulting ODE system (5.1), we compare two splitting methods in this section. The IMEX: linear-nonlinear splitting, which is widely used together with IMEX-RK schemes, and the HEVI: operator splitting, which is more popular in the atmospheric modeling community.

5.2.1 IMEX: Linear-nonlinear splitting

A classical splitting idea is to decompose the system into a linear part $F_L(q)$ and the remaining nonlinear part $\{F(\mathbf{q}) - F_L(\mathbf{q})\}$,

$$\frac{\partial \mathbf{q}}{\partial t} = \{F(\mathbf{q}) - F_L(\mathbf{q})\} + F_L(\mathbf{q}). \tag{5.5}$$

The linear part $F_L(\mathbf{q})$ is given as follows,

$$\mathbf{F_L} = \begin{pmatrix} \nabla \cdot (\rho \mathbf{u}) \\ \nabla \cdot (p'_L \mathbb{I}) + \rho' g \vec{k} \\ \nabla \cdot (\bar{\theta} \rho \mathbf{u}) \end{pmatrix} = \begin{pmatrix} \frac{\partial \rho u}{\partial x} + \frac{\partial \rho w}{\partial z} \\ \frac{\partial p'_L}{\partial x} \\ \frac{\partial p'_L}{\partial z} + \rho' g \\ \frac{\partial \bar{\theta} \rho \vec{u}}{\partial x} + \frac{\partial \bar{\theta} \rho \vec{w}}{\partial z} \end{pmatrix}$$

where $\mathbb{I}$ is the 2×2 identity matrix and p'_L is the linearized pressure

$$p'_L = \frac{\gamma \bar{p}}{\bar{\rho}\bar{\theta}} (\rho\theta)'.$$

The linear part $\mathbf{F_L}$ is stiff and is in charge of the fast acoustic wave and gravity waves. The nonlinear $\{F - F_L\}$ part is nonstiff and is charge of the advection motion. $F_L(q)$ is associated with fast wave modes and is solved implicitly. The remaining part $\{\mathbf{F} - \mathbf{F}_L\}$ is associated with slow wave modes and is solved explicitly. The IMEX-splitting needs the global implicit solve, which can be very time-consuming for large three-dimensional problems. Giraldo et al. (2010) proposed a modified splitting scheme to take advantage of the anisotropy characteristics of usual large scale atmospheric simulations. Given that the fact the computational domain is usually much wider in horizontal than tall in vertical, the modified splitting scheme only linearizes the pressure term in the vertical direction:

$$\mathbf{F_{LV}} = \begin{pmatrix} \frac{\partial \rho w}{\partial z} \\ 0 \\ \frac{\partial p'_L}{\partial z} + \rho' g \\ \frac{\partial \bar{\theta} \rho \vec{w}}{\partial z} \end{pmatrix}$$

The speed of the linearized system is given as $\sqrt{\frac{\gamma\bar{p}}{\bar{\rho}}}$. To differ from the first IMEX discretization, this splitting is denoted as IMEX-V, whereas the first one is denotes as IMEX-HV. As mentioned by Sebastien et al. [9], this IMEX-HV (and also IMEX-V) method shows some instability due to the inconsistency between gradient term and the source term on the right hand side when the anisotrophic property of the grid system is severe. We also observed similar spurious oscillation by employing this IMEX splitting in our framework. However, the operator-splitting, as mentioned below, does not present such instability for a similar setup. Therefore, we believe that HEVI: operator splitting is a more reasonable idea to split the entire system.

5.2.2 HEVI: Operator splitting

The operator splitting used in the HEVI context treats the entire horizontal component explicitly, while solving the remaining vertical component implicitly,

$$\frac{\partial \mathbf{q}}{\partial t} = F_H(\mathbf{q}) + F_V(\mathbf{q}). \tag{5.6}$$

The horizontal part $F_H(\mathbf{q})$ and the vertical part $F_V(\mathbf{q})$ are respectively defined as

$$\mathbf{F_H} = \begin{pmatrix} \frac{\partial(\rho u)}{\partial x} \\ \frac{\partial(\rho u w)}{\partial x} \\ 0 \\ \frac{\partial(\rho u \theta)}{\partial x} \end{pmatrix}, \quad \mathbf{F_V} = \begin{pmatrix} \frac{\partial(\rho w)}{\partial z} \\ 0 \\ \frac{\partial(\rho w^2 + p')}{\partial z} + \rho' g \\ \frac{\partial(\rho w \theta)}{\partial z} \end{pmatrix}.$$

where the speed of the horizontal system and vertical system equals to $\sqrt{c}+|u|$, $\sqrt{c}+|w|$, respectively, and $c = \sqrt{\frac{\gamma p}{\rho}}$ is the speed of the acoustic wave.

Since the aspect ratio between horizontal and vertical grid spacing is usually about $\mathcal{O}(10^2) \sim \mathcal{O}(10^3)$, to relax the CFL condition constrained by the small vertical grid spacing, the vertical part $F_V(\mathbf{q})$ is solved implicitly, whereas the horizontal part $F_H(\mathbf{q})$ is solved explicitly. Similar to IMEX-V decomposition, the operator splitting can take advantage of the widely used horizontal domain decomposition in the atmospheric dynamical cores. Operator splitting therefore overcomes the worst stability constraints without the need for a global implicit solution with the associated global

communication. The longest stable time-step is shorter than the full implicit, but the computational cost per time-step is reduced, especially on massively parallel computers where communication slows down global matrix solutions [93].

Atmospheric simulations is usually performed using several different resolutions. The merit of a particular time integration method should be evaluated under the considered applications. As suggested by Hamilton [33], a typical set-up for a global atmospheric model is with 300 km horizontal resolution and 1 km vertical resolution. With the estimation of sound waves speed of 350 m s^{-1} and typical horizontal and vertical wind speeds of 50 m s^{-1} and 1m s^{-1} respectively [9], we can compare the approximation of the maximum stable time step sizes of different time discretization approaches, as shown in Table 5.1. Δt^V_{max} is unspecified for HEVI discretization since the entire vertical propagation waves are treated implicitly, which is denoted as "*". As we can see, both HEVI and IMEX-V permit the identical time step size, which are slightly smaller than the maximum allowed time step size of IMEV-HV schemes. However, both HEVI and IMEX-V take into consideration the horizontal domain decomposition in the atmospheric modeling and therefore are more suitable for our specific applications. For our study, we will focus on the HEVI splitting.

Table 5.1: Estimation of maximum stable time step size of the explicit time integration scheme, IMEX-HV scheme, IMEX-V scheme and HEVI scheme. The propagation speed of the fastest horizontal and vertical speeds are called c^H and c^V respectively.

	$\Delta t^H_{max} = \frac{\min(\Delta x, \Delta y)}{c^H}$	$\Delta t^V_{max} = \frac{\Delta z}{c^V}$	$\Delta t_{max} = \min(\Delta t^H_{max}, \Delta t^V_{max})$
Explicit	857.14 s	2.86 s	2.86 s
IMEX HV	6000 s	1000 s	1000 s
IMEX V	857.14 s	1000 s	857.14 s
HEVI	857.14 s	* s	857.14 s

5.3 Von Neumann stability analysis

To study the stability properties of the above IMEX-RK schemes using HEVI splitting, we perform a von Neumann stability analysis followed by [93], to a generic wave equation including fast and slow components. Let $\mathbf{q} = q(t), f(\mathbf{q}, t) = -\imath f q, g(\mathbf{q}, t) = -\imath g q$, where $\imath = \sqrt{-1}$. Eqn. (5.1)

can be written in the following form:

$$\frac{dq}{dt} + \imath f q + \imath g q = 0. \tag{5.7}$$

Using an IMEX-RK scheme, as described in (5.3)-(5.4), the amplification factor A can be defined as $q^{n+1} = Aq^n$.

In a similar fashion, we can define the amplification factor $A^{(j)}$ for the intermediate RK stage as $Q^{(j)} = A^{(j)}q^n$. Therefore, considering a general IMEX-RK scheme,

$$A^{(j)} = 1 - \imath f \Delta t \sum_{k=1}^{j-1} \tilde{a}_{jk} A^{(k)} - \imath g \Delta t \sum_{k=1}^{j} a_{jk} A^{(k)}, \tag{5.8}$$

$$A = 1 - \imath f \Delta t \sum_{j=1}^{s-1} \tilde{c}_j A^{(j)} - \imath g \Delta t \sum_{j=1}^{s} c_j A^{(j)}. \tag{5.9}$$

When using HEVI scheme, $f\Delta t$ and $g\Delta t$ represents the Courant number associated with horizontal and vertical wave speed respectively. For clarity, we denote the horizontal and vertical Courant number as $k_H\Delta t$ and $k_V\Delta t$. It is required that $|A| \leq 1$ for a stable explicit time integration scheme. In particular, $|A| < 1$ indicates the scheme is damping, which is highly desired.

The contour plots of the magnitude of the amplification factors for different ARK schemes are shown in Figure 5.1. We are particularly interested in the stability region of the IMEX-RK schemes in the well-resolved scale (i.e. in the explicit limit $g(\mathbf{q}, t) = k_V\Delta t \equiv 0$). It is observed that ARS2(2,2,2) is unconditionally unstable in the explicit limit, i.e. there is no such a region that satisfies $|A| \leq 1$. This is not surprising. Actually, not only ARS2(2,2,2) but also those second-order schemes with only two explicit stages are not stable in the explicit limit, since it is well known that there is no two-stage, second-order, stable explicit scheme. The rest schemes, with 3 or more explicit stages, are stable as $k_V\Delta t \to 0$ for some finite values of $k_H\Delta t$ but unstable for small region near the origin. The instability region of ARS3(2,3,3) is slightly larger, compared with that of ARK2(2,3,2). Among the four schemes studied here, only Strang-splitting exhibits no instability region in the vicinity of the origin. This is because that Strang-splitting is a full split which does not update the explicit and implicit terms at the same stage. So, the amplification factor of Strang-splitting is actually the product of the amplification factor of trapezoidal rule and SSP-RK3 scheme, given

the fact that the operator is commutable in the linear stability analysis. The instability region of the Strang-splitting scheme is independent of k_V and only relies on k_H. This is why we observe the contour line of $|A| = 1$ is in parallel to the y axis. Except for ARS2(2,2,2), all the rest three schemes are viable candidates for the atmospheric applications in the context of HEVI time discretization. In the following study, we consider the numerical performance of Strang-splitting and ARS3(2,3,3) as a representative of second- and third-order schemes, respectively.

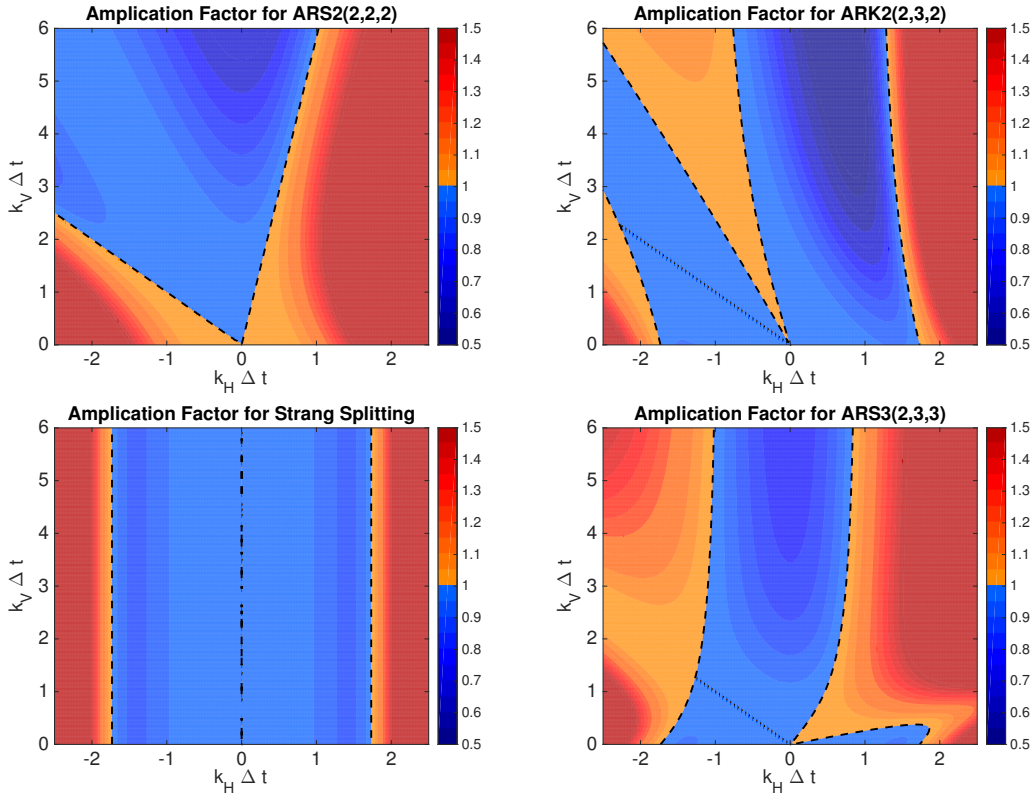

Figure 5.1: Contour plots of the magnitude of amplification factor of different IMEX-RK schemes. The contour levels are $[0.5, 1.5]$ with an increment of 0.05. The black dash contour is 1.

5.4 Implementation of IMEX-RK schemes

The efficiency of the IMEX-RK schemes is mainly influenced by the choice of the vertical implicit solver. We use the Newton's method to solve the vertical implicit part. For the linear system resulting from each Newton step, either a direct solver or GMRES iterative method can be

applied.

To identify the implicit Function at each stage, let $\mathbf{f}^{(j)} = \mathbf{f}(\mathbf{Q}_j, t_0 + \tilde{c}_j \Delta t), \quad \mathbf{g}^{(j)} = \mathbf{g}(\mathbf{Q}_j, t_n + c_j \Delta t)$. At the i-th stage, one needs to solve

$$\mathbf{Q}_i = \mathbf{q}_n + \mathbf{Y}^{(i)} + \Delta t a_{ii} \mathbf{g}^{(i)}, \quad i \geq 1, \quad \mathbf{Y}^{(i)} = \Delta t \sum_{j=1}^{i-1} (\tilde{a}_{ij} \mathbf{f}^{(j)} + a_{ij} \mathbf{g}^{(j)}) \tag{5.10}$$

Since the implicit component of IMEX-RK schemes are either SDIRK or ESDIRK schemes, all the nonzero diagonal terms are identical: $a_{ii} \equiv \lambda, i \geq 1$. So, we need to solve a nonlinear function

$$F(\mathbf{Q}_i) = \mathbf{Q}_i - \Delta t \lambda g^{(i)} - \mathbf{q}_n - \mathbf{Y}^{(i)} = 0 \tag{5.11}$$

To apply the Newton-Krylov algorithm to (5.11), given the approximation $\mathbf{Q}^{(k)}$ from k-th Newton iteration, we need to find the approximation $\mathbf{Q}^{(k+1)}$ at the (k+1)-th iteration by (the i-th subscript for the substage is omitted),

$$\mathbf{J}_k \mathbf{d}^{(k)} = -\mathbf{F}^{(k)}, \tag{5.12}$$

$$\mathbf{Q}^{(k+1)} = \mathbf{Q}^{(k)} + \mathbf{d}^{(k)} \tag{5.13}$$

where

$$\mathbf{J}_k = \mathbf{F}'(\mathbf{Q}^{(k)}) = [I - \Delta t \lambda \frac{\partial \mathbf{g}}{\partial \mathbf{q}}\Big|_{\mathbf{q}=\mathbf{Q}^{(k)}}] \tag{5.14}$$

is the Jacobian matrix, and $\mathbf{d}^{(k)} = \mathbf{Q}^{(k+1)} - \mathbf{Q}^{(k)}$ is the displacement.

5.4.1 Choices of linear solvers

At each Newton iteration (5.12)-(5.13), if the nonlinear function is simple enough, we can compute the Jacobian of the nonlinear function analytically and directly solve the linear system (5.12). Since a_{ii} is identical for each stage, for better performance, the Jacobian matrix can be recycled for each substage to save some computational cost. Alternatively, we can also apply the Newton-krylov method in a Jacobian-free fashion, which is the so-called Jacobian-free Newton Krylov (JFNK) algorithm. For JFNK, the Jacobian matrix is not explicitly computed and instead only the matrix-vector multiplication of the Jacobian matrix on some vector $\mathbf{V}$ is needed:

$$\mathbf{J}_k \mathbf{V} \approx \frac{F(\mathbf{Q}^{(k)} + \varepsilon \mathbf{V}) - F(\mathbf{Q}^{(k)})}{\varepsilon} \tag{5.15}$$

Here, the crucial part is the choice of the parameter $\varepsilon > 0$. There are several choices available, see for example Knoll & Keyes [43]. Our choice is

$$\varepsilon := \begin{cases} \sqrt{(1 + ||\mathbf{Q}^{(k)}||_2)\varepsilon_m} & \text{if } ||\mathbf{V}||_2^2 > \varepsilon_m, \\ \varepsilon_m & \text{otherwise,} \end{cases} \tag{5.16}$$

where $\varepsilon_m \approx 10^{-15}$ denotes the machine precision. The stopping criteria for the Newton iteration is

$$\|F(\mathbf{Q}^{(k)})\|_2 \leq \epsilon_r \|F(\mathbf{Q}^{(0)})\|_2 + \epsilon_a,$$

where $\epsilon_r = 10^{-3}, \epsilon_a = 10^{-11}$. The stopping criteria for the GMRES iteration is that the linear residual $\mathbf{r}_k = \mathbf{J}_k \mathbf{d_k} + \mathbf{F}(\mathbf{Q}^{(k)})$ satisfies

$$\|\mathbf{r}_k\|_2 \leq \eta \| |F(\mathbf{Q}^{(k)})| \|_2, \tag{5.17}$$

where the forcing term η is adaptively changed as the nonlinear iteration progresses. We choose η using a method of safeguarding to protect against over-solving [37]. The Newton iteration is usually called outer Newton iteration while the linear system is called inner linear solve.

The vertical implicit part is essentially a one-dimensional problem. For the DG spatial discretization, the current element is only connected to neighboring two elements. As a consequence, the Jacobian matrix $\mathbf{J}_k = \mathbf{F}'(\mathbf{Q}^{(k)}) = [I - \Delta t \lambda \frac{\partial \mathbf{g}}{\partial \mathbf{q}}\Big|_{\mathbf{q}=\mathbf{Q}^{(k)}}]$ is a block tridiagonal matrix and the sparse structure of the Jacobian matrix is shown in Fig.5.2

Due to the horizontal domain decomposition employed in our particular applications, the vertical elements are located on the same processor and we actually solve this one-dimensional problem in serial. Thomas' algorithm is the best choice for directly solving a block tridiagonal system on a single processor, since it gives linear complexity in terms of the number of blocks. For the direct solver, we use Thomas's algorithm, while for the JFNK, we use the GMRES [69] as the inner linear solver.

5.4.2 Design of a right preconditioner for the GMRES solver

The performance of JFNK approach is greatly dependent on the design of the proper preconditioner in order to reduce the number of linear solves. In order to improve the convergence of the

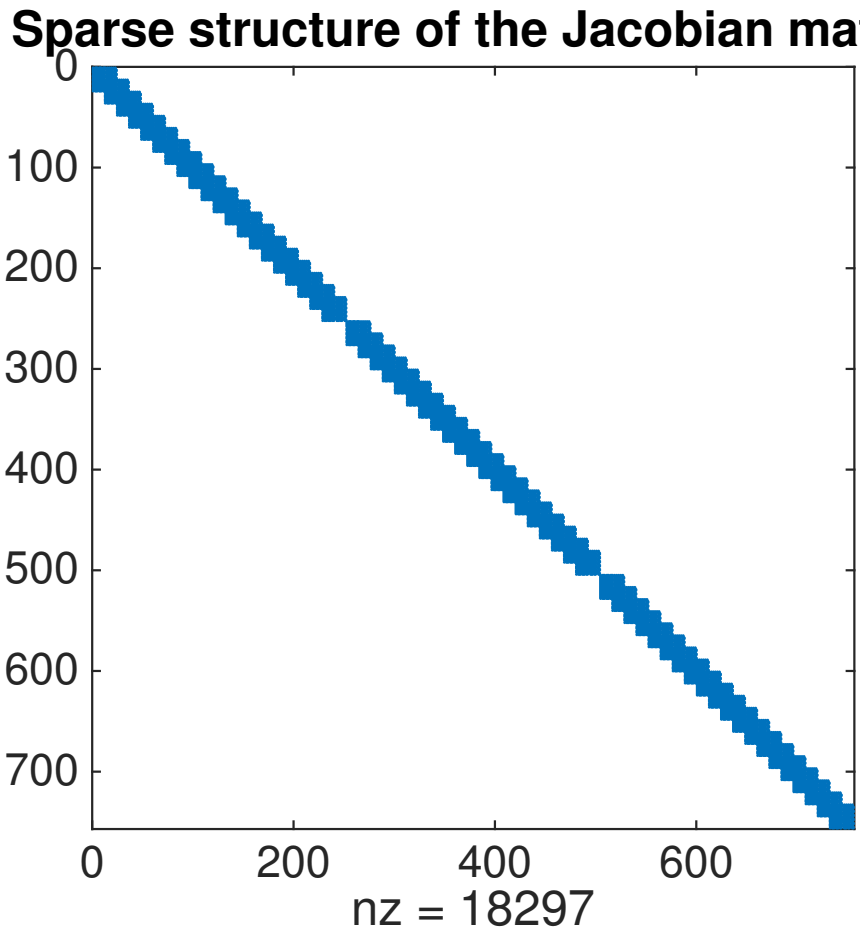

Figure 5.2: The sparse structure of the Jacobian matrix for the vertical component.

GMRES iterations, instead of solving Eqn.5.12, a right preconditioner is applied in the following way [43],

$$\mathbf{J}_k\mathbf{P}^{-1}(\mathbf{P}\mathbf{d}^{(k)}) = -\mathbf{F}^{(k)} \tag{5.18}$$

where $\mathbf{P}$ is an approximation to $\mathbf{J}_k$. As suggested by Robert Klöfkorn (2015, personal communication), a proper right preconditioner for JFNK can be constructed by evaluating the Jacobian matrix at the background hydrostatically balanced state for atmospheric applications. The governing equations are a perturbed Euler system where the prognostic variables are usually small perturbation to the hydrostatic balanced state. For near-balanced air flows, the Jacobian matrix computed at the background state is a reasonable choice. However, for the waves with strenuous

dynamics, a mechanism to detect the aging of the preconditioner and give the signal to update the Jacobian matrix will be of great importance. However, this is beyond the scope of our study. We use the fixed Jacobian matrix at the background state without recomputing as the preconditioner for the inner GMRES solver.

5.5 Numerical experiments

We compare the results of HEVI-Strang and ARS3(2,3,3) schemes qualitatively as well as their computational efficiency in this section. Same benchmark test-cases used in Section 4.4 are used here. The detailed description of initial conditions as well as boundary conditions are omitted here.

5.5.1 Qualitative comparison

To perform qualitative comparison between HEVI-Strang and ARS3(2,3,3) schemes, we examine the simulations of the benchmark test cases. The contour plots for the potential temperature θ' at 3000 s of Inertial gravity wave (IGW) test using two schemes are shown in Fig. 5.3. As we can see, both schemes yield qualitative simulations, which are in line with the results using SSP-RK3 in Fig. 4.3. The difference between the results from two schemes are very minor, though more fine features are captured by ARS3(2,3,3). As a third-order scheme, ARS3(2,3,3) provides slightly more accurate results than HEVI-Strang scheme, which is only second-order. Similar results are observed by in Fig.5.4 from using warming bubble test, and from Fig. 5.5 using Straka density test. However, ARS3(2,3,3) is computationally more expensive, as it needs two implicit solves per time-step while HEVI-Strang only needs one.

5.5.2 Performance comparison

To investigate the performance of HEVI-Strang and ARS3(2,3,3), we use IGW test and warm bubble test and test two options for solving the inner linear system: a direct solver or GMRES

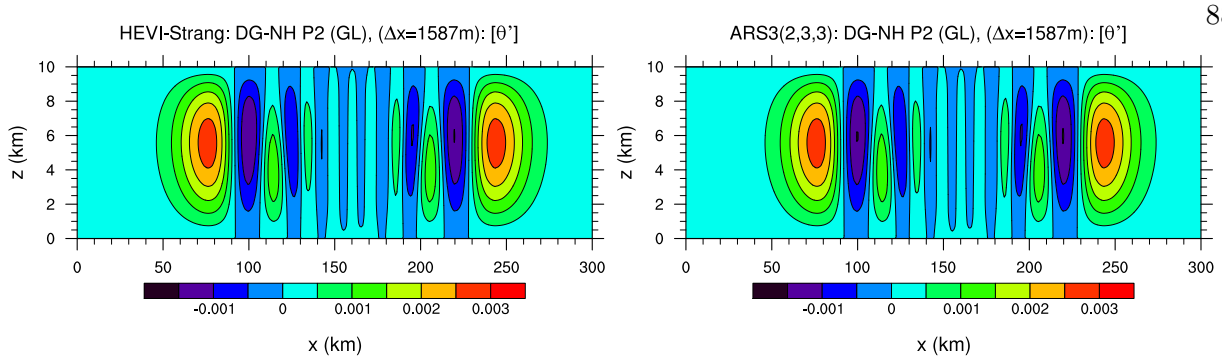

Figure 5.3: Contour plots for potential temperature perturbation for Inertia gravity wave test at $t = 3000$ s on a grid of approximate 1600 m in horizontal and 160 m in vertical (63×21 elements and 3 GL points). $\Delta t = 1.4$ s and the simulation runs for $T = 3000$ s. The left panel is with HEVI-Strang, and the right is with ARS3(2,3,3).

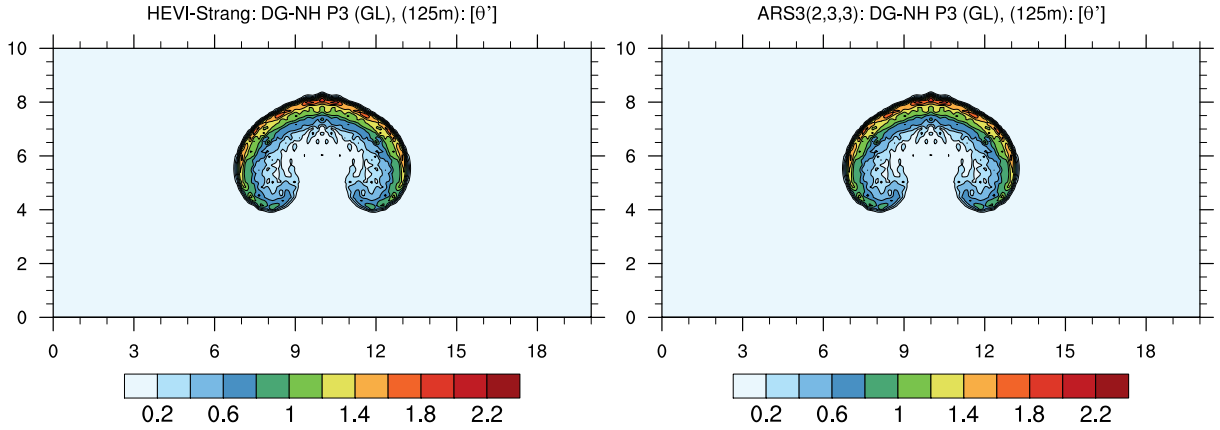

Figure 5.4: Contour plots for potential temperature perturbation for warm bubble test at $t = 1000$ s on a grid of approximate 125 m in horizontal and 125 m in vertical (20×40 elements and 4 GL points). $\Delta t = 0.125$ s and the simulation runs for $t_T = 1000$ s. The left panel is using HEVI-Strang, and the right is using ARS3(2,3,3).

solver. For GMRES solver, a right preconditioned GMRES is also tested together with the non-preconditioned version. The results from explicit SSP-RK3 scheme are used as a baseline.

5.5.2.1 Inertia Gravity Wave Test

The timing results for $\Delta x/\Delta z = 10$ are shown in Table (5.2)-(5.3) on a grid of approximately 1600 m in horizontal and 160 m in vertical. Two experimental configurations are examined: one is using 63×21 elements with 3 GL points and the other one is using 21×7 elements using 8

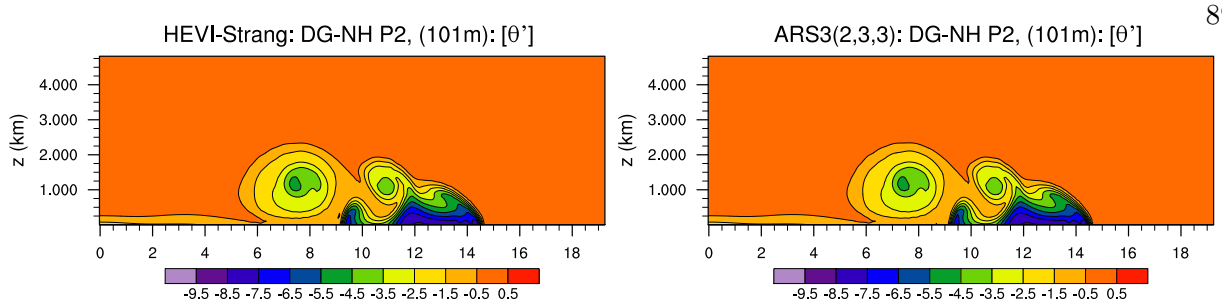

Figure 5.5: Contour plots for potential temperature perturbation for Straka density test at $t = 900$ s on a grid of approximate 100 m in horizontal and 100 m in vertical (50×50 elements and 4 GL points). $\Delta t = 0.04$ s and the simulation runs for $t_T = 900$ s. The left panel is using HEVI-Strang, and the right is using ARS3(2,3,3).

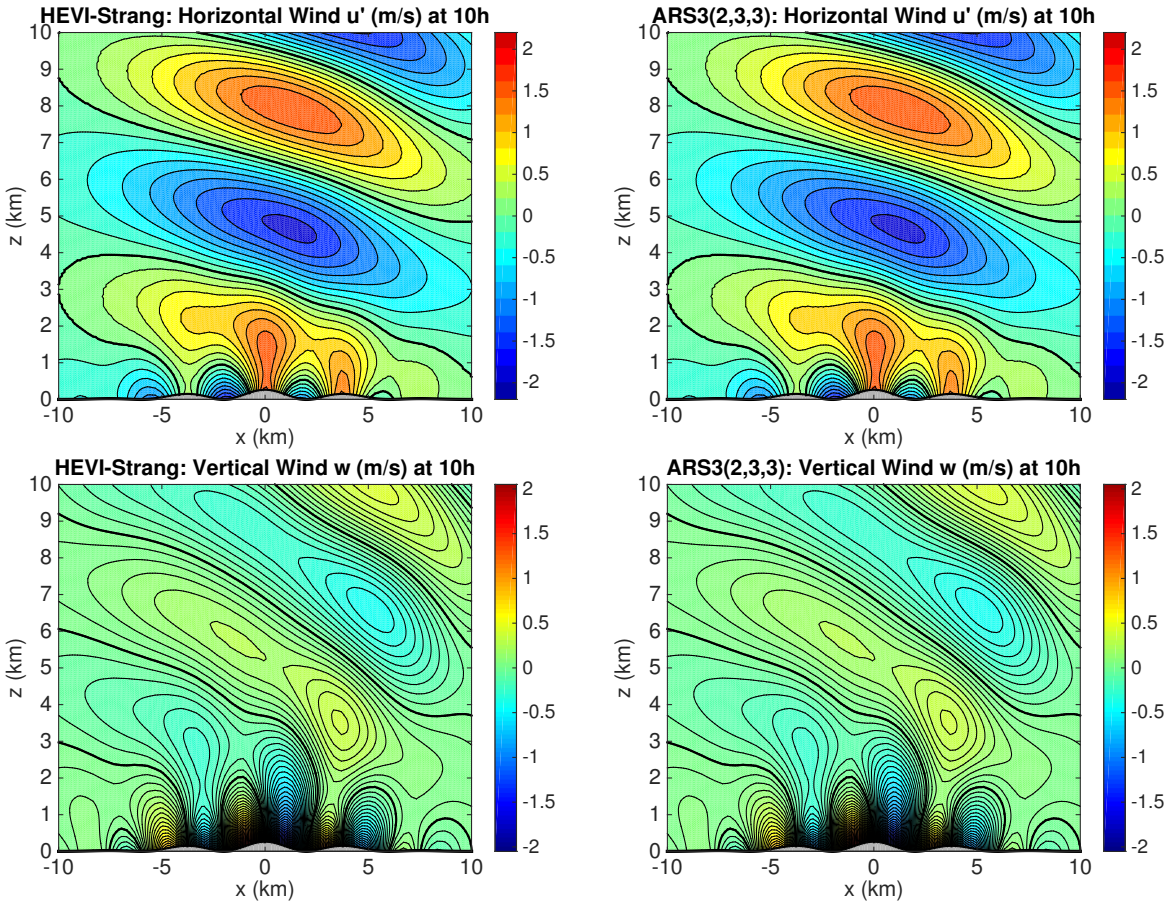

Figure 5.6: Contour plots for potential temperature perturbation for Straka density test at $t = 10$ hr on a grid of approximate 250 m in horizontal and 105 m in vertical (50×50 elements and 4 GL points). $\Delta t = 0.125$ s and the simulation runs for $t_T = 10$ hr. The left panel is using HEVI-Strang, and the right is using ARS3(2,3,3).

GL points. The result from explicit SSP-RK3 scheme is used as a reference and the timing of other schemes are normalized to it. We can see that both schemes yield evident speedup compared against the SSP-RK3 scheme, which demonstrate the computational benefit of using an IMEX-RK scheme over an explicit scheme. The only exception is the ARS3(2,3,3) with non-preconditioned GMRES. This combination is actually slower than the SSP-RK3 scheme. When the number of GL grid points N_p is moderate, the direct solver offers 50% speedup compared to JFNK method. However, when N_p increases to 8, there is no obvious improvement by using a direct solver over the JFNK method. For the GMRES solver, the improvement of using a right preconditioner is also not evident for this setup.

Table 5.2: Timing results of different IMEX-RK schemes for IGW test on a grid with $\Delta x = 1600$ m and $\Delta z = 160$ m (63×21 elements and 3 GL points). The SSP-RK3 explicit scheme is used as a reference. Timing results are normalized to timing result of SSP-RK3 scheme. Using 63 processors, SSP-RK3 scheme takes 7.66 s to run. GMRES-p means using right preconditioned GMRES as the inner linear solver.

RK scheme	Vertical solver	Δt	Normalized Time
SSP-RK3		0.14 s	1.0
HEVI-Strang	Direct Solver	1.4 s	0.33
HEVI-Strang	GMRES	1.4 s	0.64
HEVI-Strang	GMRES-p	1.4 s	0.42
ARS3	Direct Solver	1.4 s	0.51
ARS3	GMRES	1.4 s	1.08
ARS3	GMRES-p	1.4 s	0.59

Table 5.3: Timing results of different IMEX-RK schemes for IGW test on a grid with $\Delta x = 1600$ m and $\Delta z = 160$ m (21×7 elements and 8 GL points) The SSP-RK3 explicit scheme is used as a reference. Timing results are normalized to timing result of SSP-RK3 scheme. Using 21 processors, SSP-RK3 scheme takes 53.90 s to run.

RK scheme	Vertical solver	Δt	Normalized Time
SSP-RK3		0.046 s	1.0
HEVI-Strang	Direct Solver	0.46 s	0.17
HEVI-Strang	GMRES	0.46 s	0.24
HEVI-Strang	GMRES-p	0.46 s	0.23
ARS3	Direct Solver	0.46 s	0.36
ARS3	GMRES	0.46 s	0.43
ARS3	GMRES-p	0.46 s	0.43

To get the notion of how HEVI time discretization works under a typical aspect ratio $\Delta x/\Delta z$ in the global atmospheric models, the timing results for an increased aspect ratio $\Delta x/\Delta z = 100$ are shown in Table 5.4. This experiment is run on a grid with 1600 m horizontal resolution and 16 m vertical resolution (63×210 elements and 3 GL points). By using the direct solver, both schemes yield remarkable speedup compared with the explicit SSP-RK3 scheme. For the inner linear solver of the vertical implicit component, a big difference is observed between the direct solver and the JFNK method. Direct solver only costs about 5% of the computing time required by SSP-RK3, whereas the performance using JFNK is greatly degraded. HEVI-Strang is slightly cheaper than the SSP-RK3 scheme and ARS3(2,3,3) is even more expensive, though $\Delta t_{HEVI} = 100\,\Delta t_{explicit}$. The right-preconditioned GMRES, which is denoted as GMRES-p, presents evident speedup than non-preconditioned GMRES, and shows comparable efficiency with the direct solvers. To show the effect of the right preconditioner for GMRES, the number of averaged Newton iterations per time-step and the number of averaged GMRES per Newton iteration for $\Delta x/\Delta z = 10, 100$ are shown in Table 5.5. While the number of outer Newton's iterations is about 1, the number of inner linear solver increases dramatically as $\Delta x/\Delta z$ increases. For both schemes, when $\Delta x/\Delta z = 10$, the number of GMRES solve per Newton's iteration increases from 20 to 300 as $\Delta x/\Delta z$ varies from 10 to 100. After applying the right preconditioner, the number of the outer Newton solve per time-step is still 1, and the number of GMRES solves decreases to 1 and is not affected by $\Delta x/\Delta z$. The right preconditioner can effectively reduce the number of GMRES iterations and the overall computing time is comparable to the direct solver.

5.5.2.2 Warm Bubble Test

We use warm bubble test to investigate the performance of the two schemes when $\Delta x = \Delta z$. There is no advantage by using IMEX-RK schemes for this test case as $\Delta t_{explicit} = \Delta t_{HEVI}$. However, since the dynamics is more vigorous, we would like to see the efficiency of the two schemes when $\Delta t_{HEVI} = \Delta t_{explicit}$. The timing results of Strang-splitting and ARS3(2,3,3) on a 125 m horizontal and 125 m vertical resolution (40×20 elements and 4 GL points) are shown in

Table 5.4: Timing results of different IMEX-RK schemes for IGW test on a 1600 m horizontal and 16 m vertical resolution (63×210 elements and 3 GL points).The SSP-RK3 explicit scheme is used as a reference. Timing results are normalized to timing result of SSP-RK3 scheme. Using 63 processors, SSP-RK3 scheme takes 726.40 s to run.

RK scheme	Vertical solver	Δt	Normalized Time
SSP-RK3		0.014 s	1.0
HEVI-Strang	Direct Solver	1.4 s	0.03
HEVI-Strang	GMRES	1.4 s	0.92
HEVI-Strang	GMRES-p	1.4 s	0.03
ARS3	Direct Solver	1.4 s	0.05
ARS3	GMRES	1.4 s	1.49
ARS3	GMRES-p	1.4 s	0.06

Table 5.5: Number of Newton iteration per time-step and number of GMRES solve per Newton iteration of different IMEX-RK schemes and different inner linear solvers for IGW test

$\Delta x/\Delta z$	RK scheme	Vertical solver	Newton per time-step	GMRES per Newton
10	HEVI-Strang	GMRES	1.0	17.54
	HEVI-Strang	GMRES-p	1.0	1.0
	ARS3	GMRES	1.0	20.89
	ARS3	GMRES-p	1.0	1.0
100	HEVI-Strang	GMRES	1.0	308.36
	HEVI-Strang	GMRES-p	1.0	1.0
	ARS3	GMRES	1.0	293.91
	ARS3	GMRES-p	1.0	1.0

Table 5.6. We also use the result of SSP-RK3 as a baseline and normalize the wall clock time of other schemes with respect to it.

It is not surprising that all the schemes with different combinations are slower than explicit SSP-RK3 scheme since the implicit solve is expensive. Among all the scheme combinations we tested here, using HEVI-Strang and direct solver offers the best performance, which is only about 2.5 times of the explicit scheme. The more accurate ARS3(2,3,3) is approximately twice expensive than the HEVI-Strang, since ARS3(2,3,3) has two implicit stages. However, the improvement by using a direct solver over the GMRES solver is not obvious for both schemes. Similar to the IGW test, the number of GMRES solves is not related to a particular scheme. The average GMRES solve per newton's iteration is 3.1 for both schemes, which is very small. But the cost of constructing analytic

Jacobian matrix adds some overhead to the direct solver. Therefore, the overall improvement by using a direct solver is minor for this model set-up. The timing results between direct solver and GMRES solve are very comparable. However, applying the right preconditioner to GMRES solver actually deteriorates the performance of JFNK solver, as it takes some additional computational costs for constructing and applying the right preconditioner. Though the number of GMRES solves decreases to around 1.5, the overall computing cost is more expensive than the non-preconditioned GMRES.

Table 5.6: Timing results of different IMEX-RK schemes for warm bubble test on a 125 m horizontal and vertical resolution (40×20 elements and 4 GL points). The SSP-RK3 explicit scheme is used as a reference. Timing results are normalized to timing result of SSP-RK3 scheme. Using 4 processors, SSP-RK3 scheme takes 71.31 s to run.

RK scheme	Vertical solver	Δt	Normalized Time
SSP-RK3		0.04 s	1.0
HEVI-Strang	Direct Solver	0.04 s	2.38
HEVI-Strang	GMRES	0.04 s	2.84
HEVI-Strang	GMRES-p	0.04 s	2.96
ARS3	Direct Solver	0.04 s	4.58
ARS3	GMRES	0.04 s	4.75
ARS3	GMRES-p	0.04 s	6.34

Table 5.7: Number of Newton iteration per time-step and number of GMRES solve per Newton iteration of different IMEX-RK schemes and different inner linear solvers for warm bubble test

RK scheme	Vertical solver	Newton per time-step	GMRES per Newton
HEVI-Strang	GMRES	1.0	3.29
HEVI-Strang	GMRES-p	1.0	1.08
ARS3	GMRES	1.0	3.08
ARS3	GMRES-p	1.0	1.47

5.6 Summary and Conclusions

From the linear stability analysis, we investigate the stability property of various IMEX-RK schemes in the HEVI framework. HEVI-Strang, as a second IMEX-RK schemes does not have instability region in the explicit limit ($g(t, \mathbf{q}) = 0$). Only ARS2(2,2,2) shows no stability region

and it confirms that there is no stable second-order schemes with two explicit stages in the explicit limit for a generic wave equation in the HEVI context [93]. The rest schemes, with at least three explicit stages, present some instability region near the origin of the contour plot of the magnitude of the amplification factor at the well-resolved scale ($g(t, \mathbf{q}) = 0$). Except for ARS2(2,2,2), all the other schemes would be possible choices for atmospheric applications using HEVI splitting.

Qualitatively, both schemes yield similar results for the benchmark test cases, and the simulations are very close to the results using SSP-RK3 scheme. To study the efficiency of different linear solvers, we compare the performance of HEVI-Strang and ARS3(2,3,3) schemes using IGW and warming bubble test. When the aspect ratio is moderate, direct solver shows little improvement over GMRES solver, while at a large aspect ratio, direct solve significantly speeds up and the efficiency of GMRES solver degrades. This is due to the increase of GMRES solves for inner linear solve. The proposed right preconditioner, using the Jacobian matrix evaluated at the background state, can reduce the number of GMRES iterations in the inner linear solver.

HEVI-Strang only requires one implicit solve to obtain a second-order temporal accuracy, which is less expensive compared with other IMEX-RK schemes. The improved HEVI-Strang proposed by [91], by recycling the implicit solve from the last substage in the previous time-step, can reduce the number of horizontal explicit stages, which can be beneficial under the horizontal domain decomposition. Numerical results demonstrate that HEVI-Strang is a more efficient choice than ARS3(2,3,3), as it only needs one implicit solve. HEVI-Strang also yields qualitative simulations, which are virtually identical to that of ARS3(2,3,3). For atmospheric modeling, usually a second-order time scheme can meet the requirement of accuracy. Therefore, we will use the HEVI-Strang scheme as the time-integration scheme for the 3D DG-NH model.

Chapter 6

HEVI in 3D framework

6.1 Introduction

Global nonhydrostatic (NH) models with horizontal grid resolutions on the order of a few kilometers are becoming increasingly popular due to the recent paradigm shift in supercomputing resources. Many climate modeling groups have already begun to develop NH models [86, 100].

Recently, the HOMME framework is being extended to a NH dynamical core, the "High-Order Multiscale Atmospheric Model (HOMAM)". Since the DG method possesses computationally desirable properties such as local and global conservation, geometric flexibility, high on-processor operations and minimal communication footprints, it is used as the basic spatial discretization scheme for the HOMAM. Orography is handled by the terrain-following height-based coordinate system. Traditionally, 3D global NH models are developed in a dimension-split manner, which combines the horizontal 2D (spherical surface) and vertical 1D domains, using various standard discretization techniques [77, 79, 100]. A major reason for this is the ease of implementing various semi-implicit time integration schemes, which alleviates the stringent CFL stability requirement resulting from the vertical aspects of the dynamics. Although the DG method can handle 3D elements [10, 38], we prefer to use the conventional dimension-split approach for HOMAM because of the previously stated reason.

One of the major challenges for NH modeling is to develop a practical time-stepping method. The high aspect ratio between horizontal and vertical grid spacing combined with fast-moving acoustic waves impose a stringent stability constraint for explicit time stepping. In Chapter 5, we

introduce a time-splitting approach that is horizontally-explicit and vertically-implicit (HEVI) and relies on the Strang-type operator-split philosophy as a practical way to address this problem for high-order DG NH models [6]. The model time stepping is independent of the vertical resolution, and is limited only by the horizontal Courant number. Our goal is to extend the HEVI scheme to the HOMAM framework for practical NH dynamics, and testing the 3D transport scheme is a step toward this direction.

In HOMAM [57], we test the HEVI scheme and the horizontally-explicit, vertically-explicit (HEVE) scheme, and their performance is compared against a fully explicit Runge-Kutta method without time-splitting. The Dynamical Core Model Intercomparison Project (DCMIP) [34], provides a set of benchmark test cases for validating global NH atmospheric models. Recently, Kent et al. [40] used a subset of DCMIP tests specifically designed for 3D global advection, and compared the performance of different atmospheric models. For the current study, we are particularly interested in two challenging advection test-cases and one non-hydrostatic test-case to validate the time-split transport scheme used in HOMAM.

6.2 The 3D framework

We will study the transport scheme and NH scheme in the 3D framework using cubed-sphere geometry and shallow atmosphere approximation.

6.2.1 The 3D advection scheme and the 3D NH scheme

The transport equation for a passive tracer with mixing ratio q, without sources or sinks, can be written in the following conservative flux form:

$$\frac{\partial \rho\, q}{\partial t} + \nabla \cdot (\vec{v}\, \rho\, q) = 0, \tag{6.1}$$

where ρ is the air density, $\vec{v}$ is the wind field and ∇ is the gradient operator in 3D. Note that ρ follows the mass continuity equation $\partial\rho/\partial t + \nabla \cdot (\vec{v}\rho) = 0$. In order to simplify the test criteria, [40] used a divergence-free field $\vec{v}\rho$, and the resulting time-independent density ρ is analytically prescribed as an initial condition.

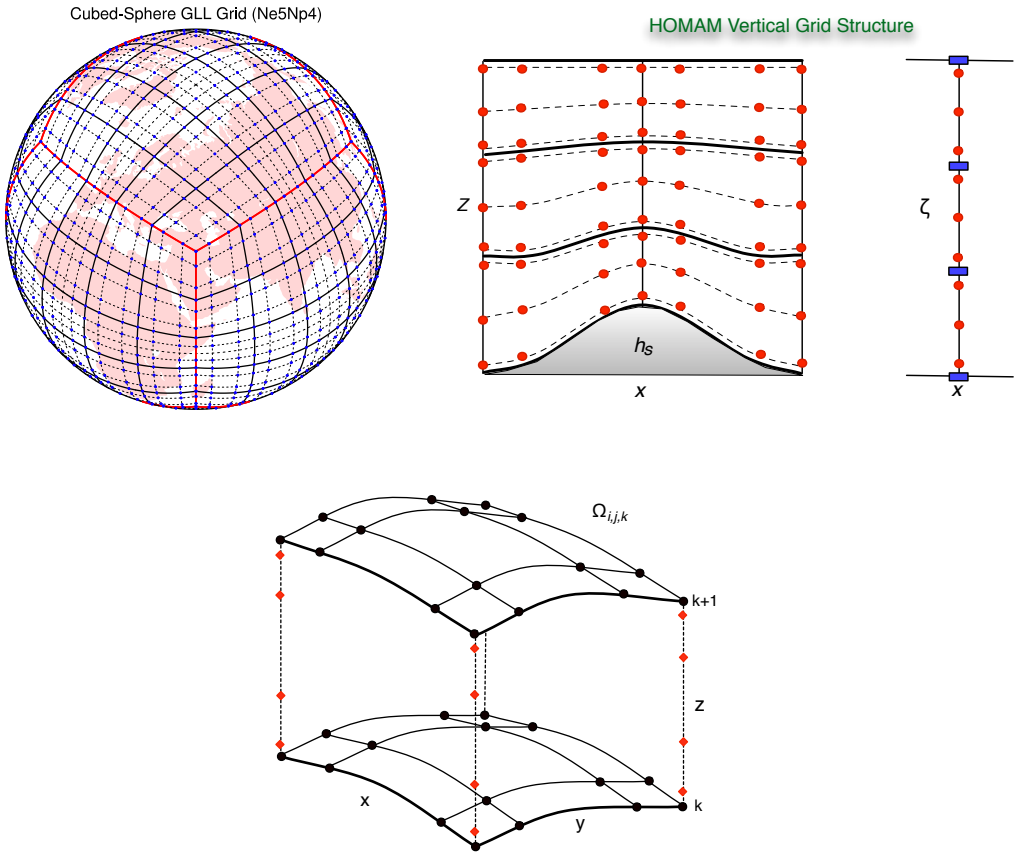

Figure 6.1: Schematic diagram showing the horizontal and vertical grid structure for HOMAM. The horizontal grid system relies on a cubed-sphere (top left) tiled with GLL quadrature element. The vertical grid lines comprise 1D elements with GL quadrature points as shown in the top right panel. The computational grid of an entire column block is shown in the bottom panel.

Based on the conservation of mass, momentum and potential temperature, the NH atmospheric model is characterized by the classical compressible Euler System (4.1)-(4.3)

6.2.2 Computational domain

The horizontal domain for HOMAM is a sphere $\mathcal{S}$ representing the planet Earth, and is based on the cubed-sphere topology shown in Fig. 6.1.

To formulate the transport equation in the 3D framework, for the cubed-sphere surface, the Jacobian of the orthogonal components to the contravariant vector transformation (the metric term) is $\sqrt{G}_h = [\det(G_{ij})]^{1/2} = |\mathbf{A}|$. The details of the local transformation laws and $\mathbf{A}$ for each

face of the cubed-sphere can be found in [55].

The accurate representation of terrain is very important for practical NH modeling where mountain waves are forced by the irregularities of the earth's surface. Although the DG method is capable of handling complex terrain with an unstructured grid, we prefer to use the classical terrain-following coordinates introduced by Gal-Chen and Sommerville [21] for Eq. (6.4). The Jacobian associated with the vertical transform in $(x, y, z) \to (x^1, x^2, \zeta)$ is

$$\sqrt{G}_v = \left[\frac{\partial z}{\partial \zeta}\right]_{(x^1,x^2)} = 1 - \frac{h_s(x^1, x^2)}{z_{top}}. \tag{6.2}$$

The vertical velocity in the ζ-coordinate is $\tilde{w} = d\zeta/dt$ and is related to w via [12]

$$\sqrt{G}_v \tilde{w} = w + \sqrt{G}_v G_v^{13}\, u^1 + \sqrt{G}_v G_v^{23}\, u^2, \tag{6.3}$$

where the metric coefficients are defined as follows:

$$\sqrt{G}_v G_v^{13} = \left[\frac{\partial h_s}{\partial x^1}\right]_{(z)} \left(\frac{\zeta}{z_{top}} - 1\right), \; \sqrt{G}_v G_v^{23} = \left[\frac{\partial h_s}{\partial x^2}\right]_{(z)} \left(\frac{\zeta}{z_{top}} - 1\right),$$

where the horizontal derivatives of the surface topography are analytically determined for the DCMIP test cases to follow.

The transport equation and Euler system can be generally expressed in 3D (x^1, x^2, x^3) curvilinear coordinates, where x^3 denotes the variable in the radial (vertical) direction $\vec{r}$ with respect to the sphere. With the shallow atmosphere approximation, r is treated as a constant such that $x^3 = r + z$ and $z \ll r$, where z may be interpreted as the geometrical height from the surface. Thus the independent variables are (x^1, x^2, z) in the computational coordinates, and the vertical velocity is given by $w = dz/dt$. Note that the horizontal metric term $\sqrt{G}_h$ is independent of z.

- The transport equation (6.1) in flux-from for a tracer variable q in 3D (x^1, x^2, z) coordinates can be written as

$$\frac{\partial \rho q}{\partial t} + \frac{1}{\sqrt{G}_h}\left[\frac{\partial}{\partial x^1}(\sqrt{G}_h \rho q\, u^1) + \frac{\partial}{\partial x^2}(\sqrt{G}_h \rho q\, u^2) + \frac{\partial}{\partial z}(\sqrt{G}_h \rho q\, w)\right] = 0. \tag{6.4}$$

On the terrain-following coordinate system, the final form of (6.4) can be written in the (x^1, x^2, ζ) coordinates as follows,

$$\frac{\partial \psi}{\partial t} + \frac{\partial(\psi u^1)}{\partial x^1} + \frac{\partial(\psi u^2)}{\partial x^2} = -\frac{\partial(\psi \tilde{w})}{\partial \zeta}, \tag{6.5}$$

where the pseudo density $\psi = \sqrt{G_h}\sqrt{G_v}\rho q$, combines the time-independent horizontal $(\sqrt{G_h})$ and the vertical $(\sqrt{G_v})$ metric terms, and the conservative variable ρq.

- Similar to the 2D case, we split $\rho = \bar{\rho} + \rho'$, $p = \bar{p} + p'$ and $\rho\theta = (\bar{\rho\theta}) + (\rho\theta)'$ as mean and perturbed state such that the mean state follows the hydrostatic balance. The 3D compressible perturbed Euler system of equations on a rotating sphere in generalized curvilinear coordinates (x^1, x^2, x^3) can be written in tensor form (**Warsi, 1992**):

$$\begin{aligned}
\frac{\partial \rho'}{\partial t} + \frac{1}{\sqrt{G}}\left[\frac{\partial}{\partial x^j}(\sqrt{G}\,\rho u^j)\right] &= 0 \quad \{\textbf{Summation Implied}\} \\
\frac{\partial \rho u^i}{\partial t} + \frac{1}{\sqrt{G}}\left[\frac{\partial}{\partial x^j}[\sqrt{G}(\rho u^i u^j + p\,G^{ij})]\right] + \Gamma^i_{jk}(\rho u^j u^k + p'\,G^{jk}) &= f\sqrt{G}(u^1\,G^{2i} - u^2\,G^{1i}) - \rho g\,G^{3i} \\
\frac{\partial(\rho\theta)'}{\partial t} + \frac{1}{\sqrt{G}}\left[\frac{\partial}{\partial x^j}(\sqrt{G}\,\rho\theta\,u^j)\right] &= 0 \\
\frac{\partial \rho \mathbf{q}}{\partial t} + \frac{1}{\sqrt{G}}\left[\frac{\partial}{\partial x^j}(\sqrt{G}\,\rho\mathbf{q}\,u^j)\right] &= 0
\end{aligned}$$

where the associated Christoffel symbols (second kind) are defined as

$$\Gamma^i_{jk} = \frac{1}{2}G^{il}\left[\frac{\partial G_{kl}}{\partial x^j} + \frac{\partial G_{jl}}{\partial x^k} - \frac{\partial G_{kj}}{\partial x^l}\right]$$

On the terrain-following coordinate system, the final form of (**??**)-(**??**) can be written in

the (x^1, x^2, ζ) coordinates as follows,

$$\frac{\partial \rho'}{\partial t} + \frac{1}{\sqrt{G}}[\frac{\partial}{\partial x^1}\sqrt{G}\rho u^1 + \frac{\partial}{\partial x^2}\sqrt{G}\rho u^2 + \frac{\partial}{\partial x^3}\sqrt{G}\rho u^3] = 0 \tag{6.6}$$

$$\frac{\partial \sqrt{G}\rho u^1}{\partial t} + \frac{\partial}{\partial x^1}\left[\sqrt{G}(\rho u^1 u^1 + G_h^{11} p')\right] + \frac{\partial}{\partial x^2}\left[\sqrt{G}(\rho u^1 u^2 + G_h^{12} p')\right] + \frac{\partial}{\partial \zeta}\left[\sqrt{G}\rho u^1 \tilde{w} + \sqrt{G}(G_v^{13} G_h^{11}\, p' + G_v^{23} G_h^{12}\, p')\right] = \sqrt{G_v} S_u^1. \tag{6.7}$$

$$\frac{\partial \sqrt{G}\rho u^2}{\partial t} + \frac{\partial}{\partial x^1}\left[\sqrt{G}(\rho u^2 u^1 + G_h^{21} p')\right] + \frac{\partial}{\partial x^2}\left[\sqrt{G}(\rho u^2 u^2 + G_h^{22} p')\right] + \frac{\partial}{\partial \zeta}\left[\sqrt{G}\rho u^2 \tilde{w} + \sqrt{G}(G_v^{13} G_h^{21}\, p' + G_v^{23} G_h^{22}\, p')\right] = \sqrt{G_v} S_u^2. \tag{6.8}$$

$$\frac{\partial(\sqrt{G}\,\rho w)}{\partial t} + \frac{\partial(\sqrt{G}\,\rho w u^1)}{\partial x^1} + \frac{\partial(\sqrt{G}\,\rho w u^2}{\partial x^2} + \frac{\partial[\sqrt{G}\,\rho w \tilde{w} + \sqrt{G_h}\,p)]}{\partial \zeta} = -\sqrt{G}\,\rho' g \tag{6.9}$$

$$\frac{\partial(\rho\theta)'}{\partial t} + \frac{1}{\sqrt{G}}\left[\frac{\partial}{\partial x^1}\sqrt{G}\rho\theta u^1 + \frac{\partial}{\partial x^2}\sqrt{G}\rho\theta u^2 + \frac{\partial}{\partial x^3}\sqrt{G}\rho\theta u^3\right] = 0 \tag{6.10}$$

$$\frac{\partial(\rho q_k)}{\partial t} + \frac{1}{\sqrt{G}}\left[\frac{\partial}{\partial x^1}\sqrt{G}\rho q_k u^1 + \frac{\partial}{\partial x^2}\sqrt{G}\rho q_k u^2 + \frac{\partial}{\partial x^3}\sqrt{G}\rho q_k u^3\right] = 0 \tag{6.11}$$

where $\sqrt{G} = \sqrt{G_h}\,\sqrt{G_v}$ is the **composite** metric term for the Euler system in the (x^1, x^2, ζ) coordinates, which is used for discretizing the Euler equations, and $\tilde{w}$ is the vertical velocity in ζ-coordinate, should be computed with

$$\sqrt{G_v}\tilde{w} = w + \sqrt{G_v} G_v^{13} u^1 + \sqrt{G_v} G_v^{23} u^2 \tag{6.12}$$

Detailed formula of the Euler system on the computational domain can be found in Appendix A.

Both transport equation (6.5) and Euler system can be written in the following generalized form as a conservation law,

$$\frac{\partial U}{\partial t} + \nabla \cdot \mathbf{F}(U) = S(U) \quad \text{in } \mathcal{D} \times (0, \mathrm{t_T}], \tag{6.13}$$

where T is a prescribed time.

In a dimension-split case, the source term $S(U)$ appearing in (6.13) corresponds to the vertical derivative on the RHS of (6.5) or (6.6)-(6.11). On each horizontal layer (cubed-sphere surface), defined by $\zeta = \zeta_k$ of the 3D domain, we adopt the nodal DG discretization which employs the

Lagrange polynomials $h_l(\xi)$, $\xi \in [-1,1]$, $0 \le l \le N$ (with $N+1 = N_p$ solution points), as the basis functions with roots at the GLL quadrature points (see [53] for details), as shown in the left panel of Fig. 6.1. This is the standard setup in the HOMME framework which we adopt in our current work. For the vertical slice, we consider DG spatial discretization for K vertical 1D elements in $[h_s, z_{top}]$, in which we employ the GL quadrature grid (see Fig. 6.1 right panel). The GL quadrature is more accurate than the GLL case and allows $K \times N_g$ independent vertical levels, where N_g is the number of GL points. Thus the total degrees-of-freedom for the time-evolving global tracer field q is $6\,N_e^2 N_p^2 \times K N_g$. The semi-discretized equation corresponding to (6.13) can generally be written in the following form:

$$\frac{d}{dt}\,\mathbf{U} = \mathbf{L}(\mathbf{U}) \quad \text{in} \quad (0, t_T), \tag{6.14}$$

where $\mathbf{L}$ indicates DG spatial discretization.

6.2.3 Time integration

We consider three time integrators for solving (6.14): an explicit SSP-RK3 method, as defined in (2.16) and the time-split schemes HEVE and HEVI. The HEVE scheme has only a limited practical value for NH models, nevertheless, it gives reference results for comparison with the HEVI scheme. The HEVE scheme is based on the Strang operator-split approach [6], which is up to $O(\Delta t^2)$ accurate. The spatial DG discretization $L(U)$ corresponding to (6.5) is decomposed into the horizontal L^H and vertical L^V parts such that $L(U) = L^H(U) + L^V(U)$. For the given time interval $[t, t+\Delta t]$, the Strang-splitting scheme has the following 3 steps:

$$U_1 := U_h(t), \qquad \frac{d}{dt}U_1 = L^H(U_1) \quad \text{in } (t, t+\Delta t/2] \tag{6.15}$$

$$U_2 := U_1(t+\Delta t/2), \qquad \frac{d}{dt}U_2 = L^V(U_2) \quad \text{in } (t, t+\Delta t], \tag{6.16}$$

$$U_3 := U_2(t+\Delta t), \qquad \frac{d}{dt}U_3 = L^H(U_3) \quad \text{in } (t+\Delta t/2, t+\Delta t], \tag{6.17}$$

and $U_h(t+\Delta t) = U_3(t+\Delta t)$. The above HEVE algorithm follows an $H-V-H$ cycle, and each stage requires an ODE solve, which can be performed with SSP-RK3. However, for the HEVI scheme, we use the improved Strang-splitting, which is still in a sequence of V-H-V, where the first

V-stage is reused from the last implicit V-stage of the previous time-step. This can reduce some communication overhead due to the additional horizontal explicit solve in the standard Strang-splitting idea.

6.3 Numerical Experiments

The DCMIP [34] test suite includes benchmark advection test cases for global transport problems, where a 3D non-divergent wind field is prescribed. The details of the test configurations and standard error norms are well documented in [40], which we do not describe herein. The initial conditions include prescribed functions for the tracer field q, density ρ and the 3D analytical velocity field (u, v, w). The wind fields are converted to computational coordinates (x^1, x^2, ζ), consistent with HOMAM, using the relations (**??**) and (6.3). For the test-cases considered herein, we use 4×4 GLL points for horizontal elements ($Np = 4$) and $N_g = 4$ GL points in the vertical 1D elements. No limiter or filter is used with the advection scheme.

6.3.1 Meridional "Hadley" circulation

This experiment is test case 1-2 of the DCMIP test suite [34, 40], in which a deformational flow that mimics a Hadley-like meridional circulation is prescribed. The initial scalar field q is a quasi-smooth cosine profile. The wind fields are designed so that the flow reverses itself halfway through the simulation and returns the tracers to their initial position, therefore, the exact solution is known at the end of the run. This test is designed to investigate the impact of horizontal-vertical spatial splitting on the accuracy of the scheme.

Figure 6.2 shows a vertical-meridional slice of the tracer field along the 180° longitude line at four different times during the 1-day simulation with the HOMAM. The horizontal resolution is $1^\circ \times 1^\circ$ ($N_e = 30, N_p = 4, N_g = 4$), there are 60 vertical levels, and the time step is 60 seconds. At $t = 12$ hours, the tracer field is at its maximum displacement from the initial condition. At the end of the simulation ($t = 24$ hours), the tracer field closely resembles its initial value, with some deviation noticeable near latitudes $\pm 30^\circ$ where the tracer field experienced the most stretching.

The resolution dependency of the normalized errors at a fixed small time step of 6 seconds is shown in Fig. 6.3. The left-hand panel indicates that the vertical convergence rate is approximately 2nd-order, while the right-hand panel shows a combined horizontal-vertical convergence rate of greater than 2nd-order. Table 6.1 compares the combined horizontal and vertical convergence rates of four different models, including Mcore[90], CAM-FV [40] and CAM-SE [31], for the Hadley experiment. The HOMAM has the highest rate of convergence of the models.

Table 6.1: Average convergence rate for the normalized error norms for the Hadley test (DCMIP test 1-2) computed using resolutions $2^\circ, 1^\circ, 0.5^\circ$ horizontal, and respectively with $30, 60, 120$ vertical levels, and with $\Delta t = 6$s for HOMAM.

Errors/Models:	Mcore	CAM-FV	CAM-SE	HOMAM
ℓ_1	2.22	1.93	2.27	2.62
ℓ_2	1.94	1.84	2.12	2.43
ℓ_∞	1.64	1.66	1.68	2.16

Table 6.2: Error norms at different vertical resolutions with a fixed horizontal resolution 1° and $\Delta t = 12$s for the DCMIP test 1-3.

Error/Levels:	L36	L60	L120
ℓ_1	1.3534	0.9654	0.7841
ℓ_2	0.7541	0.5458	0.4989
ℓ_∞	0.8864	0.7655	0.7658

Figure 6.3 also shows that the split time differencing schemes (both HEVE and HEVI) have a minimal effect on the error norms when compared to the explicit un-split RK3 scheme. The results of temporal convergence tests (not shown) indicate between first- and second-order convergence with the split schemes for the Hadley simulation. However, this test is not ideal for studying time-discretiztion errors. Solid-body rotation would be better suited for this purpose and the model will be tested with this case in the future. Also, the effects of stability with the Strang splitting on the horizontally explicit component will also be tested.

6.3.2 Advection over rough topography

DCMIP test-case 1-3 [34] investigates the ability of the tracer transport algorithm to accurately advect tracers over topography. A series of steep concentric ring-shaped mountain ranges

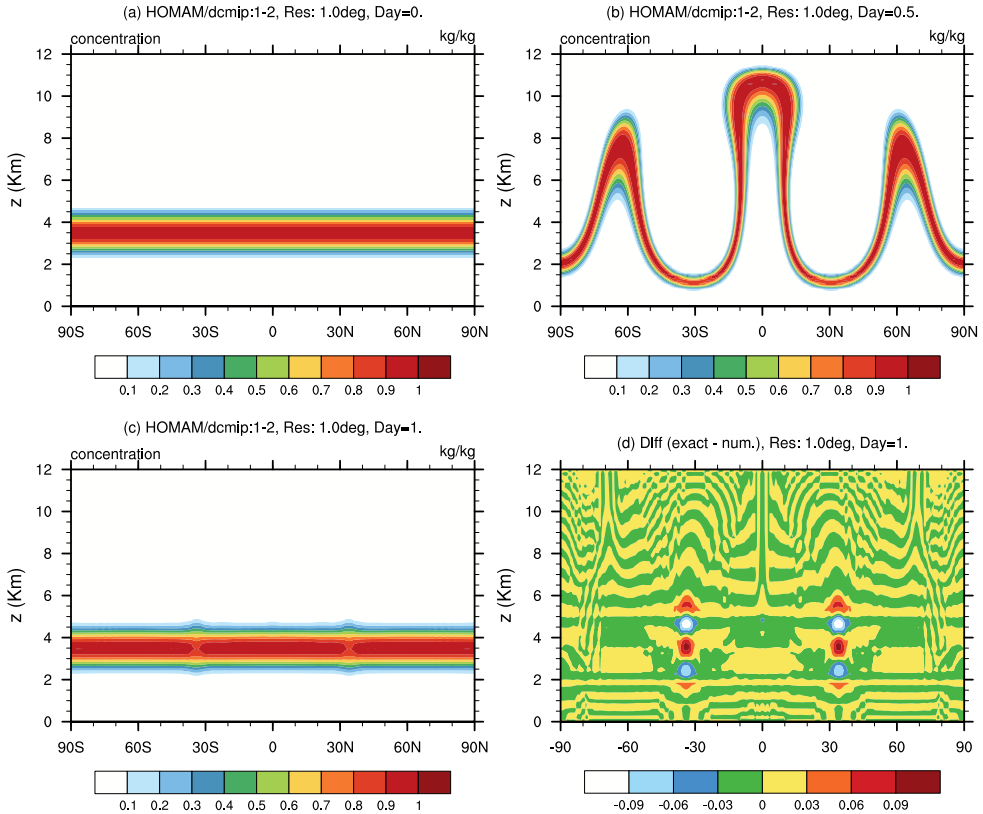

Figure 6.2: Vertical meridional cross-section of the tracer field $q = q_1$ for the Hadley test (DCMIP 1-2), simulated with HOMAM at a horizontal resolution of $1^\circ \times 1^\circ$ ($N_e = 30, N_p = 4, N_g = 4$) with 60 vertical levels and $\Delta t = 60$s at times (a) $t = 0$, (b) $t = 12$, and (c) $t = 24$ hours. The difference between the analytical and simulated field at $t = 24$ hours is shown in (d).

forms the terrain. The prescribed flow field is a constant solid-body rotation and the tracer field q is given by three thin vertically stacked cloud-like patches (non-smooth) which circumnavigate the globe and return to their initial positions after 12 days. In height coordinates, the vertical velocity (w) is zero, however, in the terrain-following vertical ζ coordinate system, there is a vertical velocity ($\tilde{w}$) caused by the topography which induces cross-coordinate vertical advection. As in DCMIP test-case 1-2, the exact solution at the end of the run is the initial condition.

Figure 6.4 shows the results of the simulation with HOMAM at the initial condition, halfway into the simulation when the tracer fields are centered over the highest mountains, and at the end of the run when the tracers have returned to their original position. Overall, the shapes of the tracer patches have been maintained, however, some dissipation has occurred. The right-hand column of

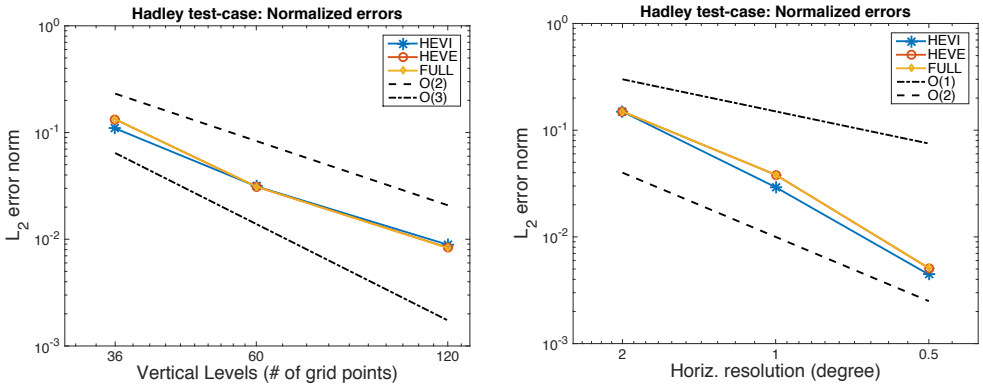

Figure 6.3: Convergence of ℓ_2 error norm for the Hadley test after 1 day with HOMAM. The left panel shows the explicit SSP-RK3 (FULL), HEVE and HEVI schemes at a fixed horizontal resolution of 1°, $\Delta t = 6$s, and varying vertical levels. The right panel shows results of varying the 3D (horizontal and vertical) resolution.

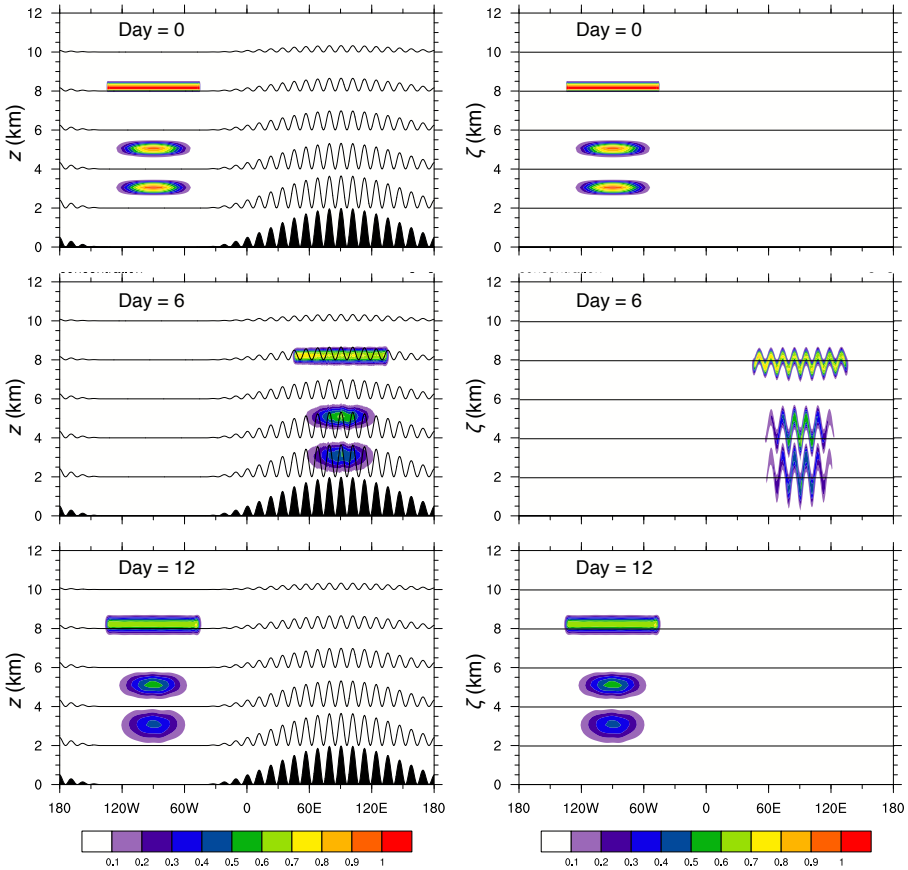

Figure 6.4: Vertical cross-sections along the equator for the tracer field $q = q4$ for the DCMIP test 1-3 with the top panels showing the initial fields. Left and right columns show the simulated results on the vertical z and transformed ζ coordinates, respectively, at days 6 and 12. The black shading indicates bottom topography and the dark thin lines are reference horizontal grid lines. The results are simulated with HOMAM using the HEVE scheme at a horizontal resolution of 1°, 60 vertical levels, and $\Delta t = 12$s.

panels in Fig. 6.4 shows the tracer fields in the model coordinate (ζ) system. The plot at day 6 shows the considerable vertical displacement across model levels that occurs. Table 6.2 shows the normalized errors for the runs with varying vertical resolution and the horizontal resolution fixed at 1° and the time step at 12 seconds. The error norms of HOMAM are comparable to or better than those of other models presented in [40]. As in the Hadley experiment, the split-explicit (HEVE) time-stepping scheme has almost no affect on the errors (results not shown).

6.3.3 Non-hydrostatic gravity wave test

The only NH test case to examine here is DCMIP 3-1. DCMIP 3-1 test case investigates the response of models to short time-scale wave motion triggered by a localized perturbation [34]. The initial state is hydrostatically balanced and in gradient-wind balance. The evolution of gravity waves is trigged by an overlaid potential temperature perturbation. This test case is in the non-hydrostatic scale and is performed on a reduced-size earch. The reduction factor is set to $X = 125$, which leads to a reduced Earth with a circumference at the equator about 320 KM. The initial wind fields are defined as

$$\begin{aligned} u(\lambda, \varphi, z) &= u_0 \cos(\varphi) \\ v(\lambda, \varphi, z) &= 0 \\ w(\lambda, \varphi, z) &= 0 \end{aligned}$$

where $u_0 = 20$ m s^{-1}. A small potential temperature perturbation θ' is added to the balanced background potential temperature, where

$$\theta'(\lambda, \varphi, z) = \Delta\theta s(\lambda, \varphi) \sin(\frac{2\pi z}{L_z}) \tag{6.18}$$

where $s(\lambda, \varphi) = \frac{d^2}{d^2+r^2}$, $\Delta\theta = 1$ K and $L_z = 20000$ m.

The suggested grid spacings are about $1.125° \times 1.125°$ in the horizontal direction which yields a physical horizontal grid spacing of about 1 km near the equator. z_{top}=10 km and 10 vertical levels is suggested by [34]. The simulation should run until $t = 3600$ s.

For this test case, we use a 25×25 grid with N_p=4. and $K = 3$ vertical 1D elements with N_g=4. So, $\Delta x = \Delta y = \Delta z \approx 1$ km. With the estimation of sound waves speed of 350 m s^{-1} and maximum horizontal wind speed 20 m s^{-1}, the time-step size for the horizontal motion should satisfy:

$$\frac{\{\text{speed}\}\Delta t}{\hbar} \leq \frac{1}{2N_p - 1} \tag{6.19}$$

where speed= 370 m s^{-1} and $\hbar = \sqrt{\Delta x^2 + \Delta y^2}$. This yields that $\Delta t \leq 0.27$ s. We test the performance of Strang-splitting scheme under 12, 24 and 60 vertical levels. This leads to $\Delta x/\Delta z = 1, 2, 5$. The implicit solve is done by JFNK method since it is very challenging to construct the Jacobian matrix analytically in the 3D framework. Since the time-step size of the IMEX-RK scheme with HEVI splitting is constrained by the horizontal motion, we choose Δt=0.25 s for the numerical experiments. The contour plots of the fields of the potential temperature perturbation at $t = 3600$ s are shown for different vertical levels in Fig. 6.5. The result using 12 vertical levels and SSP-RK3 scheme is also shown as a baseline. We see that the potential temperature field at t=3600 s are virtually identical for using 12, 24 and 60 vertical levels with Strang-splitting scheme. Minor difference is observed from the result of the SSP-RK3 scheme. However, the quality of all contour plots is very close to other NH models in literature, such as ICON-IAP and ENDGame [34]. The timing results of the SSP-RK3 scheme and HEVI scheme are shown in Table 6.3. When $\Delta x/\Delta z = 1$, the HEVI scheme is about twice expensive the computing time of SSP-RK3 scheme. As the aspect ratio increases, we see that the speedup of the HEVI scheme becomes more evident. When $\Delta x/\Delta z = 5$, we observe that the computing time of HEVI-Strang is only half of the SSP-RK3 scheme. This demonstrate the correctness of our DG-NH model and also shows the effectiveness of the HEVI splitting. Since this test is run on a reduced planet, the aspect ratio is very far from the real application. In the real atmospheric simulation, $\Delta x/\Delta z$ is above $\mathcal{O}(10^2)$. We believe that the efficiency of HEVI scheme can be more notable on a unreduced Earth. However, a proper preconditioner is also desirable to improve the overall efficiency. This can be a research direction for the future work.

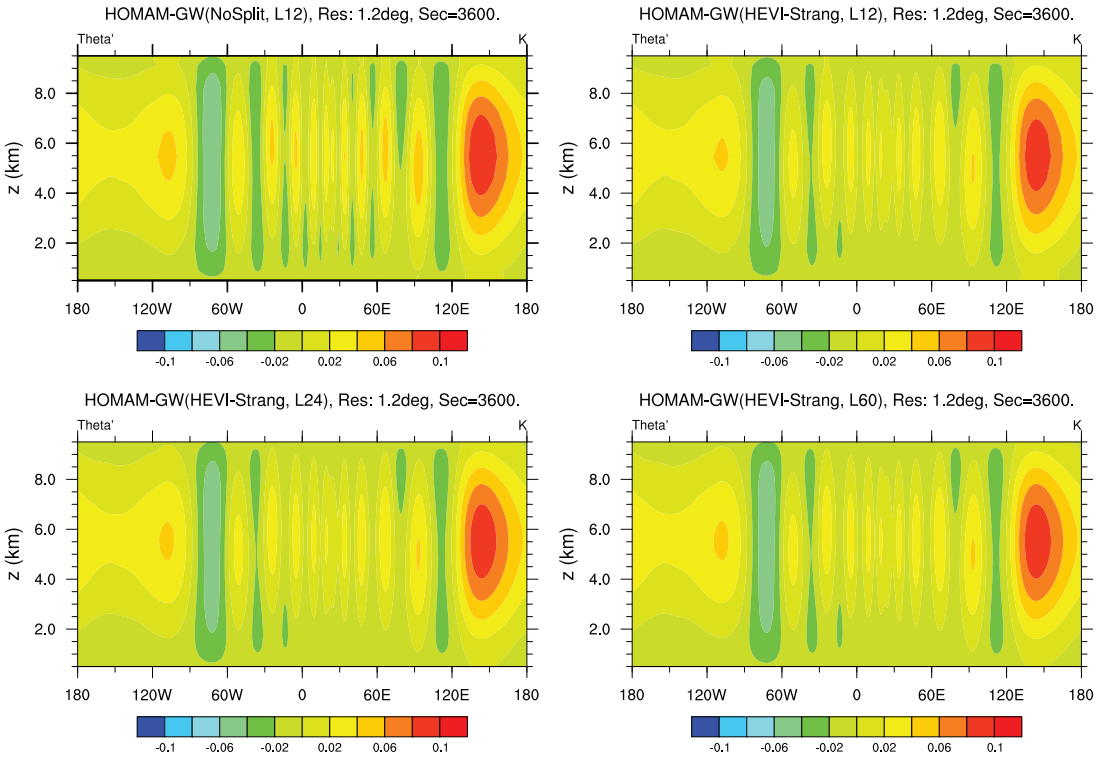

Figure 6.5: Contour plot of the potential temperature field of DCMIP 3-1 test on a grid with $1.125^\circ \times 1.125^\circ$ in the horizontal. 12, 24 and 60 vertical levels are tested for HEVI-Strang scheme. $\Delta t = 0.25$ s for all the experiments. The result using 12 vertical levels and SSP-RK3 scheme is used as a reference solution.

Table 6.3: Timing results of HEVI-Strang and SSP-RK3 for NH-IGW test on a grid with $\Delta x = \Delta y = 1$ km (25×25 elements and 3 GL points). The explicit SSP-RK3 scheme is used as a reference. The simulation runs for 3600 s.

RK scheme	$\Delta x/\Delta z$	Vertical Levels	Δt	Computing Time
SSP-RK3	1	12	0.25 s	91.0 s
HEVI-Strang		12	0.25 s	167.0 s
SSP-RK3	2	24	0.125 s	356.0 s
HEVI-Strang		24	0.25 s	349.0 s
SSP-RK3	5	60	0.05 s	2297.0 s
HEVI-Strang		60	0.25 s	1234.0 s

The strong scaling results of the HEVI-Strang scheme is shown in Fig. 6.6. $\Delta x \simeq 208$ m and $\Delta z \simeq 166.7$ m ($N_e = 128, N_p = 4, N_v = 15, N_v = 4$) for this experiment and $\Delta t_{HEVI} = \Delta t_{explicit}$. This experiment is simulated for $t_T = 1000$ s. So, there is no benefit by using HEVI-Strang scheme but the overall scalability performance of the scheme can still be evaluated. We can see that both HEVI-Strang and SSP-RK3 show nearly linear speedup. It demonstrates that HEVI-Strang does not impede the nearly optimal scalability of the HOMME framework.

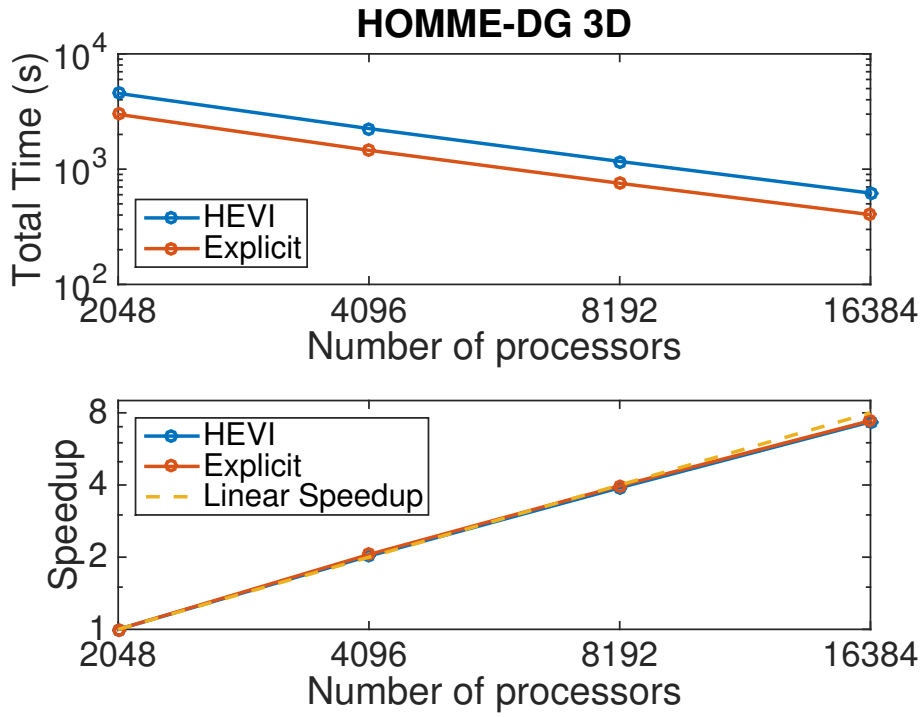

Figure 6.6: Strong scaling results of HEVI-Strang and SSP-RK3

6.4 Summary

Various time stepping schemes were tested for 3D advection in a new global atmospheric dynamical core, HOMAM. The spatial discretization of the model is based on the discontinuous Galerkin method, combining the 2D horizontal elements on the cubed-sphere surface and 1D vertical elements in the terrain-following height-based coordinate. The time integrators are the horizontally explicit and vertically implicit (HEVI), split-explicit scheme HEVE and un-split third-order Runge-Kutta scheme. Two challenging advection tests from the DCMIP test suite were used for validating the schemes. The convergence shows a second-order accuracy with the smooth scalar field, irrespective of a particular time-integrator. For the non-smooth transport, the split schemes works well and results are comparable with other published results. We also test the time-splitting schemes with the nonhydrostatic HOMAM using DCMIP 3-1. The quality of our simulation is in agreement with other NH models. By varying the vertical levels while keeping the horizontal resolution fixed, HEVI scheme (or Strang-splitting) shows almost identical results using same time step size, determined by the horizontal grid spacing. The numerical results verify that the HEVI scheme can effectively relax the CFL constraint to the horizontal part of the wave propagation. The resulting time-step size is only limited by the horizontal grid spacing. The strong scaling results demonstrates that the HEVI scheme does not degrade the inherent scalability of the HOMME framework. It shows that the HEVI scheme is an efficient and practical choice of the 3D DG-NH model. However, more DCMIP tests in the NH scale need to be tested and this can be the future work of the study.

Chapter 7

Summary and Suggested work

The hope for a high-resolution atmospheric model becomes feasible with the arrival of the next generation of massively parallel computer architecture. As a consequence, significant efforts have been put into the design of new global atmospheric models for the past decade. However, there are many changes taking place towards this goal given the new trend of high performance computing. The traditional latitude-longitude gris may no longer be a favorable choice since the numerical techniques to resolve the polar singulars will impede the overall performance. In terms of numerical methods, it is desirable that they must be designed to offer scalability on parallel systems and globally and locally conservative properties. In addition, the equation sets need to change to the compressible Euler system or Navier-Stokes system equations to include the horizontal transport of vertical momentum. Many operational atmospheric models do not use the fully conservative form of the equations and the importance of the conservative equation sets will be more noticeable in the non-hydrostatic regime. To avoid the excessive computing cost, shallow-water system can be used to answer questions about the horizontal aspects of the fully 3D model as it represents all the horizontal aspects of dynamics.

The choice of the time-integration schemes is probably one of the most prominent challenges to confront when entering the non-hydrostatic regime. As the typical large aspect ratio between horizontal and vertical resolution in the atmospheric applications is at $\mathcal{O}(10^2) - \mathcal{O}(10^4)$, the vertical resolution will be a limiting factor on the maximum stable explicit time-step size. Those non-hydrostatic models solely relying on the explicit time integration schemes will make the long-

term integrations impractical. The design of the time-integration scheme should be not determined without consideration for the typical horizontal domain decomposition in the atmospheric community and the large horizontal-vertical grid aspect ratio.

7.1 Summary

This thesis presents our ongoing efforts for extending the hydrostatic HOMME-DG model to the non-hydrostatic version. Several numerical aspects have been studied. In particular, the time-integration schemes are tackled in the 2D framework and also test qualitatively in the 3D DG-NH model.

In Chapter 2, we describe the cubed-sphere grid and discontinuous Galerkin (DG) spatial discretization method used throughout the thesis. Cubed-sphere grid is a viable replacement for traditional latitude-longitude grid in designing non-hydrostatic atmospheric models, as it avoid the issues of polar singularities and grid clustering in the latitude-longitude grids and presents quasi-uniform grid system. The DG methods have been shown to be accurate, conservative and highly scalable in many scientific fields and is therefore gaining more popularity in the atmospheric community. The discontinuous Galerkin method is also available in the hydrostatic HOMME framework, thereafter we call it HOMME-DG. This thesis is working on upgrading hydrostatic HOMME-DG model to the non-hydrostatic version.

Chapter 3 studies the importance of conservative form of the equation sets in the shallow water framework. As the major part of the horizontal dynamics of 3D NH dynamics can be characterized as global shallow water equations (SWE), a nodal DG method has been studied by using the conservative form of the SWE. The influence of the full conservative equation sets in conserving integral invariants is rigorously compared against the vector-invariant form of SWE, which is a commonly adopted by the atmospheric modelers. Several important components, such as the well-balanced correction and numerical diffusion, are also discussed briefly.

In Chapter 4, the idea of operator splitting method based on the Strang-splitting approach is experimented to develop an efficient time integration scheme for the proposed 3D DG-NH model.

This includes using the compressible Euler system in the simple x-z plane with a terrain-following height-based coordinate transform. Several NH benchmark test-cases are used to evaluate the HEVI-Strang scheme. The numerical results show that the resulting CFL constraint is relaxed to the horizontal grid resolution only. The terrain-following height-based z-coordinate system can effectively handle the complex domain and the existence of sharp mountain does not introduce any spurious noise to the HEVI time-splitting scheme.

In Chapter 5, a modified Strang-splitting scheme commonly used in literature is considered, and we compare the stability region and the performance of the HEVI-Strang scheme with other popular implicit-explicit Runge-Kutta (IMEX-RK) schemes. The HEVI-Strang scheme can be viewed as a special type of IMEX-RK methods, as it does not update the implicit term and explicit term at the same stage. According to the linear stability analysis, the HEVI-Strang scheme shows large stability region in the well-resolved scale (in the explicit limit) compared with other schemes. Two types of splitting ideas – HEVI operator-splitting and IMEX linear-nonlinear splitting – are discussed. The HEVI operator-splitting and IMEX-V splitting (which splits only in the vertical) yield identical maximum stable time-step size under the configuration of typical atmospheric applications. The numerical results also shows that the HEVI-Strang scheme is more efficient since it needs only one implicit solve. However, the vertical implicit solver is the major limitation of the overall efficiency of the HEVI scheme, and it is dominated by the linear solve inside the Newton iteration. The GMRES iteration significantly degrades as the disparity between the horizontal and vertical resolution increases. A right preconditioner for GMRES is constructed by computing the Jacobian matrix at the balanced background state. We observe that the proposed right preconditioner greatly reduces the number of GMRES solves per Newton step, and the overall performance is very close to directly solving the linear system, which is done through constructing the analytic Jacobian matrix. The HEVI-Strang scheme proves to be a practical and efficient choice under the 2D NH framework.

In Chapter 6, we incorporate the HEVI-Strang scheme into the 3D DG-NH model. The global 3D DG-NH model is constructed by vertically stacking the horizontal cubed-sphere layer.

Some of the dynamical-core model-intercomparison project (DCMIP) benchmark test cases are used to evaluate the global 3D model. The HEVI-Strang scheme works qualitatively when comparing with the results from other existing NH models. By varying the horizontal-vertical aspect ratio moderately, it is observed that the time-step size of HEVI-scheme is not affected the vertical grid spacing. This is promising because for the real life applications, the aspect ratio can be very large.

7.2 Future work

The 3D DG-NH model needs to be rigorously evaluated through additional DCMIP non-hydrostatic test cases to ensure us the accuracy of the model. Moreover, we only test the performance of HEVI-Strang scheme when the aspect ratio is moderate, which is far from $\mathcal{O}(10^2)$ in the operational application setup. It can be anticipated that GMRES may not work effectively when the aspect ratio goes large. The resulting vertical system should be either solved directly by finding the analytic Jacobian or applying the idea of right preconditioner proposed in 2D framework, as both approach both require the derivation of the analytic Jacobian matrix. Some future efforts needs to pay to formulate the analytic Jacobian matrix for the vertical implicit component.

As HEVI-Strang splitting is a full splitting scheme, different spatial discretization methods can be applied to the horizontal part and vertical part. For the current implementation, we use nodal DG methods for both parts. Another possibility is to use high-order finite volume method for the vertical component. This can be beneficial to incorporate the physics package for the real atmosphere simulations.

While the implicit vertical solver overcomes the CFL limitation in the vertical, fast acoustic waves and gravity waves still impose a less restrictive, yet still significant, constraint on the horizontal direction as well. Using a fully implicit integration in the horizontal can overcome this limitation, but in this way the element would be strongly coupled together, which may inevitably impede the good scaling of HOMME. However, it may be possible to develop a horizontal time-integration that is semi-implicit with only the fast waves being treated implicitly and the slow

waves being handled explicitly as before. The feasibility of this approach can be explored in our 2D model and if that effort proves successful, semi-implicit time scheme in horizontal can be integrated into the full 3D model.

In terms of the DG-NH model itself, the overall performance of the DG-NH model needs to be evaluated in terms of scalability by testing the computational efficiency with larger processor cores. The DG-NH model should also be assessed by comparing against other high-order NH models from DCMIP test suite. Short-term idealized climate simulations, such as Held-Suarez and aqua-planet tests, can be used to show the robustness of our DG-NH model and validate the parallel efficiency in the relative long-term simulation. The ultimate goal is to integrate the HOMME-DG into CAM framework for the real planet simulations. The current HOMME framework provides a regional refinement capability through static mesh refinement. The DG-NH model can easily incorporate this feature to facilities the regional climate simulations.

Bibliography

[1] HOMME: High-Order Method Modeling Environment. http://www.homme.ucar.edu/.

[2] N. Ahmad and J. Linedman. Euler solutions using flux-based wave decomposition. Int. J. Numer. Meth. Fluids, 54:47–72, 2007.

[3] R. Alexander. Diagonally implicit runge-kutta methods for stiff o.d.e.'s. SIAM Journal on Numerical Analysis, 14(6):1006–1021, 1977.

[4] Douglas N Arnold, Franco Brezzi, Bernardo Cockburn, and L Donatella Marini. Unified analysis of discontinuous Galerkin methods for elliptic problems. SIAM J Numer. Anal., 39(5):1749–1779, January 2002.

[5] Uri M. Ascher, Steven J. Ruuth, and Raymond J. Spiteri. Implicit-Explicit Runge-Kutta Methods for Time-Dependent Partial Differential Equations. Appl. Numer. Math, 25:151–167, 1997.

[6] L. Bao, R. Klöfkorn, and R. D. Nair. Horizontally explicit and vertically implicit (HEVI) time discretization scheme for a discontinuous Galerkin nonhydrostatic model. Mon. Wea. Rev., 2015. DOI:10.1175/MWR-D-14-00083.1.

[7] F. Bassi and S. Rebay. A high-order accurate discontinuous finite element method for the numerical solution of the compressible Navier-Stokes equations. J. Comput. Phys., 131:267–279, 1997.

[8] Alfredo Bermudez and Ma Elena Vazquez. Upwind methods for hyperbolic conservation laws with source terms. Comput. Fluids, 23(8):1049–1071, 1994.

[9] Sébastien Blaise, Jonathan Lambrechts, and Eric Deleersnijder. A stabilization for three-dimensional discontinuous Galerkin discretizations applied to nonhydrostatic atmospheric simulations. International Journal for Numerical Methods in Fluids, pages n/a–n/a, 2015.

[10] S. Brdar, M. Baldauf, A. Dedner, and R. Klöfkorn. Comparison of dynamical cores for NWP models: comparison of COSMO and Dune. Theor. Comput. Fluid Dyn., 27:453–472, 2013.

[11] John Charles Butcher. The numerical analysis of ordinary differential equations. Runge-Kutta and general linear methods. John Wiley & Sons Inc, February 1987.

[12] T. L. Clark. A small-scale dynamics model using a terrain-following coordinate transformation. J. Comput. Phys., 24:186–215, 1977.

[13] B. Cockburn. An introduction to the Discontinuous-Galerkin method for convection-dominated problems. In A. Quarteroni, editor, Lecture Notes in Mathematics: Advanced Numerical Approximation of Nonlinear Hyperbolic Equations, volume 1697, pages 151–268. Springer, 1997.

[14] B. Cockburn and C.-W. Shu. The Runge-Kutta local projection P1-Discontinuous Galerkin finite element method for conservation laws. Math. Model. Numer. Anal., 25:337–361, 1991.

[15] B. Cockburn and C-W. Shu. The local discontinuous Galerkin for convection diffusion systems. SIAM J. Numer. Anal., 35:2440–2463, 1998.

[16] J. M. Dennis, J. Edwards, K. J. Evans, O. Guba, P. H. Lauritzen, A. A. Martin, A. St-Cyr, M. A. Taylor, and P. H. Worely. CAM-SE: a scalable spectral element dynamical core for the community atmosphere model. International Journal of High Performance Computing Applications, 26:74–89, 2012.

[17] D. R. Durran. Numerical Methods for Wave Equations in Geophysical Fluid Dynamics. Springer, 1999. ISBN 0-387-98376-7, 465 pp.

[18] D. R. Durran and J. B. Klemp. A compressibel model for the simulation of moist mountain waves. Mon. Wea. Rev., 111:2341–2361, 1983.

[19] Katherine J Evans, Mark A Taylor, and John B Drake. Accuracy Analysis of a Spectral Element Atmospheric Model Using a Fully Implicit Solution Framework. Mon. Weather Rev., 138(8):3333–3341, August 2010.

[20] Natasha Flyer, Erik Lehto, Sébastien Blaise, Grady B Wright, and Amik St-Cyr. A guide to RBF-generated finite differences for nonlinear transport: Shallow water simulations on a sphere. J. Comput. Phys., 231(11):4078–4095, June 2012.

[21] T. Gal-Chen and R. C. Sommerville. On the use of a coordinate transformation for the solution of navier-stokes. J. Comput. Phys., 17:209–228, 1975.

[22] Joseph Galewsky, Richard K Scott, and Lorenzo M Polvani. An initial-value problem for testing numerical models of the global shallow-water equations. Tellus A, 56(5):429–440, 2004.

[23] A. Gelb and J. P. Gleeson. Spectral viscosity for shallow water equations in spherical geometry. Mon. Weather Rev., 129:2346–2360, September 2001.

[24] F X Giraldo, J S Hesthaven, and T Warburton. Nodal High-Order Discontinuous Galerkin Methods for the Spherical Shallow Water Equations. J. Comput. Phys., 181(2):499–525, September 2002.

[25] Francis X Giraldo, James F Kelly, and Emil M Constantinescu. Implicit-explicit formulations of a three-dimensional nonhydrostatic unified model of the atmosphere (NUMA). SIAM Journal on Scientific Computing, 35(5):B1162–B1194, 2013.

[26] F.X. Giraldo, J.S. Hesthaven, and T. Warburton. Nodal high-order Discontinuous Galerkin methods for spherical shallow water equations. J. Comput. Phys., 181:499–525, 2002.

[27] F.X. Giraldo and M. Restelli. A study of spectral element and Discontinuous galerkin method for the Navier-Stokes equations in nonhydrostatic mesoscale modeling: Equation sets and test cases. J. Comput. Phys., 227:3847–3877, 2008.

[28] S. Gottlieb, C.-W. Shu, and E. Tadmor. Strong Stability-Preserving high-order time discretization methods. SIAM Review, 43(1):89–112, 2001.

[29] Sigal Gottlieb, Chi-Wang Shu, and Eitan Tadmor. Strong Stability-Preserving High-Order Time Discretization Methods. SIAM Rev., 43(1):89–112, March 2001.

[30] Wei Guo, Ramachandran D Nair, and Jing-Mei Qiu. A Conservative Semi-Lagrangian Discontinuous Galerkin Scheme on the Cubed Sphere. Monthly Weather Review, 142(1):457–475, January 2014.

[31] D. Hall, M. Taylor, P. Ullrich, K. Reed, C. Jablonowski, R. Nair, and H. Tufo. Dynamical core model intercomparison project: CAM-SE passive tracer transport. Q. J. Roy. Meteol. Soc., 000:000–000, 2015.

[32] G. J. Haltiner and R. T. Williams. Numerical prediction and dynamic meteorology (2nd Edition), volume 110. 1984.

[33] Kevin Hamilton. High Resolution Numerical Modelling of the Atmosphere and Ocean. pages 7–27. Springer New York, New York, NY, 2008.

[34] C. Jablonowski, P. A. Ullrich, J. Kent, K. A. Reed, M. A. Taylor, P. H. Lauritzen, and R. D. Nair. Dynamical core model intercomparison project (dcmip) test case document. The 2012 Dynamical Core Model Intercomparison Project, https://www.earthsystemcog.org/projects/dcmip-2012/, 2012.

[35] Christiane Jablonowski and David L Williamson. The pros and cons of diffusion, filters and fixers in atmospheric general circulation models. In Numerical Techniques for Global Atmospheric Models, pages 381–493. Springer, 2011.

[36] Shi Jin. Runge-Kutta Methods for Hyperbolic Conservation Laws with Stiff Relaxation Terms. Journal of Computational Physics, 122(1):51–67, November 1995.

[37] C T Kelley. Solving Nonlinear Equations with Newton's Method. SIAM, January 2003.

[38] J. F. Kelley and F. X. Giraldo. A continuous and discontinuous Galerkin methods for a scalable three-dimensional nonhydrostatic atmospheric model: Limited-area mode. J. of Comput. Phys., 231:7988–8008, 2012.

[39] C A Kennedy and M H Carpenter. Additive Runge-Kutta schemes for convection-diffusion-reaction equations. Applied Numerical Mathematics, 44(1-2):139–181, January 2003.

[40] J. Kent, P. A. Ullrich, and C. Jablonowski. Dynamical core model intercomparison project: Tracer transport test cases. Q. J. Roy. Meteol. Soc., 140:1279–1293, 2014.

[41] J. B. Klemp. A terrain-following coordinate with smoothed coordinate surfaces. Mon. Wea. Rev., 139:2163–2169, 2011.

[42] Joseph B Klemp, William C Skamarock, and O Fuhrer. Numerical consistency of metric terms in terrain-following coordinates. Monthly Weather Review, 131(7):1229–1239, July 2003.

[43] D. A. Knoll and D. E. Keyes. Jacobian-free Newton-Krylov methods: a survey of approaches and applications. J. Comput. Phys., 293:357–397, 2004.

[44] P. Lasaint and P.A. Raviart. On a finite element method for solving the neutron transport equation. Math. Aspects finite Elem. partial Differ. Equat., Proc. Symp. Madison 1974, 89-123 (1974)., 1974.

[45] Michael N Levy. A High-Order Element-based Galerkin Method for the Global Shallow Water Equations. PhD thesis, University of Colorado, Boulder, November 2009.

[46] Michael N Levy, Ramachandran D Nair, and Henry M Tufo. High-order Galerkin methods for scalable global atmospheric models. Comput. Geosci., 33(8):1022–1035, August 2007.

[47] X. Li, C. Chen, X. Shen, and F. Xiao. A multimoment constrained finite-volume model for nonhydrostatic atmospheric dynamics. Mon. Wea. Rev., 141:1216–1240, 2013.

[48] R. Liska and B. Wendroff. Comparison of several difference schemes on 1d and 2d test problems for the euler equations. SIAM J. Sci. Comput., 25(3):995–1017, March 2003.

[49] S J Lock, N Wood, and Hilary Weller. Numerical analyses of Runge-Kutta implicit-explicit schemes for horizontally explicit, vertically implicit solutions of atmospheric models. Quarterly Journal of the Royal Meteorological Society, pages n/a–n/a, February 2014.

[50] Thomas Melvin, Mark Dubal, N Wood, A Staniforth, and Mohamed Zerroukat. An inherently mass-conserving iterative semi-implicit semi-Lagrangian discretization of the non-hydrostatic vertical-slice equations. Quarterly Journal of the Royal Meteorological Society, 136(648):n/a–n/a, 2010.

[51] R. D. Nair. Diffusion experiments with a global Discontinuous Galerkin shallow-water model. Mon. Wea. Rev., 137:3339–3350, 2009.

[52] R. D. Nair, H.-W. Choi, and H. M. Tufo. Computational aspects of a scalable high-order Discontinuous Galerkin atmospheric dynamical core. Computers and Fluids, 38:309–319, 2009.

[53] R. D. Nair, M. N. Levy, and P. H. Lauritzen. Emerging numerical methods for atmospheric modeling. In P. H. Lauritzen, C. Jablonowski, M. A. Taylor, and R. D. Nair, editors, Numerical Techniques for Global Atmospheric Models, volume 80, pages 189–250. Springer-Verlag, 2011. LNCSE.

[54] R. D. Nair, S. J. Thomas, and R. D. Loft. A Discontinuous Galerkin global shallow water model. Mon. Wea. Rev., 133:876–888, 2005.

[55] R. D. Nair, S. J. Thomas, and R. D. Loft. A Discontinuous Galerkin transport scheme on the cubed sphere. Mon. Wea. Rev., 133:814–828, 2005.

[56] R D Nair, S J Thomas, and R D Loft. A discontinuous Galerkin transport scheme on the cubed sphere. Mon. Weather Rev., 123:814–828, March 2005.

[57] Ram D Nair, Lei Bao, and Michael D Toy. A Time-split Discontinuous Galerkin Transport Scheme for Global Atmospheric Model. Procedia Computer Science, 51:2056–2065, 2015.

[58] Ramachandran D Nair. Diffusion Experiments with a Global Discontinuous Galerkin Shallow-Water Model. Mon. Weather Rev., 137(10):3339–3350, October 2009.

[59] Ramachandran D Nair, Stephen J Thomas, and Richard D Loft. A discontinuous Galerkin global shallow water model. Mon. Weather Rev., 133(4):876–888, 2005.

[60] Sebastian Noelle, Yulong Xing, and Chi-Wang Shu. High-order well-balanced schemes. In Numerical methods for balance laws, pages 1–66. Dept. Math., Seconda Univ. Napoli, Caserta, 2009.

[61] M. R. Norman, R. D. Nair, and F. H. M. Semazzi. A low communication and large time step explicit finite-volume solver for non-hydrostatic atmospheric dynamics. J. Comput. Phys., 230:1567–1584, 2011.

[62] Lorenzo Pareschi and Giovanni Russo. Implicit–Explicit Runge–Kutta Schemes and Applications to Hyperbolic Systems with Relaxation. JOURNAL OF SCIENTIFIC COMPUTING, 25(1):129–155, October 2005.

[63] J.M. Prusa, P.K. Smolarkiewicz, and A.A. Wyszogrodzki. EULAG, a computational model for multiscale flows. Comput. Fluids., 37:1193–1207, 2008.

[64] M Rančić, R J Purser, and F Mesinger. A global shallow-water model using an expanded spherical cube: Gnomonic versus conformal coordinates. Quart. J. Roy. Meteor. Soc., 122(532):959–982, 1996.

[65] M. Restelli and F. Giraldo. A conservative discontinuous galerkin semi-implicit formulation for the navier–stokes equations in nonhydrostatic mesoscale modeling. SIAM J. Sci. Comput., 31(3):2231–2257, 2009.

[66] Todd D Ringler. Momentum, Vorticity and Transport: Considerations in the Design of a Finite-Volume Dynamical Core. In Numerical Techniques for Global Atmospheric Models, pages 143–183. Springer, 2011.

[67] C Ronchi, R Iacono, and P S Paolucci. The "Cubed Sphere": A New Method for the Solution of Partial Differential Equations in Spherical Geometry. J. Comput. Phys., 124(1):93–114, March 1996.

[68] J. A. Rossmanith. A wave propagation method for hyperbolic systems on the sphere. J. Comput. Phys., 213:629–658, 2006.

[69] Youcef Saad and Martin H Schultz. GMRES: A Generalized Minimal Residual Algorithm for Solving Nonsymmetric Linear Systems. SIAM Journal on Scientific and Statistical Computing, 7(3):856–869, 1986.

[70] R. Sadourny. Conservative finite-difference approximations of the primitive equations on quasi-uniform spherical grids. Mon. Wea. Rev., 100:136–144, 1972.

[71] Robert Sadourny. Conservative finite-difference approximations of the primitive equations on quasi-uniform spherical grids. Mon. Weather Rev., 100(2):136–144, 1972.

[72] M. Satoh. Conservative scheme for the compressible non-hydrostatic models with the horizontally explicit and vertically implicit time integration scheme. Mon. Wea. Rev., 130:1227–1245, 2002.

[73] Masaki Satoh. Atmospheric Circulation Dynamics and Circulation Models. Springer Verlag, June 2004.

[74] Masaki Satoh, Hirofumi Tomita, Hisashi Yashiro, Hiroaki Miura, Chihiro Kodama, Tatsuya Seiki, Akira T Noda, Yohei Yamada, Daisuke Goto, Masahiro Sawada, Takemasa Miyoshi, Yosuke Niwa, Masayuki Hara, Tomoki Ohno, Shin-ichi Iga, Takashi Arakawa, Takahiro Inoue, and Hiroyasu Kubokawa. The Non-hydrostatic Icosahedral Atmospheric Model: description and development. Progress in Earth and Planetary Science, 1(1):1–32, 2014.

[75] C. Schar, D. Leuenberger, O. Fuhrer, D. Luthic, and C. Girard. A new terrain-following vertical coordinate formulation for atmospheric prediction models. Mon. Wea. Rev., 130:2459–2480, 2002.

[76] Juan Simarro, VÍctor Homar, and Gonzalo Simarro. A non-hydrostatic global spectral dynamical core using a height-based vertical coordinate. Tellus A, 65(0):487, June 2013.

[77] J. Simmaro and M. Hortal. A semi-implicit non-hydrostatic dynamical kernel using finite elements in the vertical discretization. Q. J. R. Meteorol. Soc., 138:826–839, 2012.

[78] W. C. Skamarock and J. B. Klemp. A time-split nonhydrostatic atmospheric model for weather research and forecasting applications. J. Comput. Phys., 227:3465–3485, 2008.

[79] W. C. Skamarock, J. B. Klemp, M. G. Duda, L. D. Flower, S-H. Park, and T. D. Ringler. A multiscale nonhydrostatic atmospheric model using centroidal voronoi tesselations and c-grid staggering. Mon. Wea. Rev., 140:3090–3105, 2012.

[80] W.C. Skamarock and J.B. Klemp. Efficiency and accuracy of the Klemp-Wilhelmson time-splitting technique. Mon. Wea. Rev., 122:2623–2630, 1994.

[81] A St-Cyr, C Jablonowski, J M Dennis, H M Tufo, and S J Thomas. A Comparison of Two Shallow-Water Models with Nonconforming Adaptive Grids. Mon. Weather Rev., 136:1898–1922, 2008.

[82] Amik St-Cyr and D. Neckels. A fully implicit Jacobian-free high-order Discontinuous Galerkin mesoscale flow solver. LNCS, 5545:243–252, 2009. Springer-Verlag.

[83] J.M. Straka, R.B. Wilhelmson, L.J. Wicker, J.R. Anderson, and K.K. Droegemeier. Numerical solutions of a non-linear density current: a benchmark solution and comparisons. Int. J. Numer. Meth. Fluids, 17:1–22, 1993.

[84] Gilbert Strang. On the construction and comparison of difference schemes. SIAM Journal on Numerical Analysis, 5(3):506–517, 1968.

[85] M A Taylor, J Edwards, S Thomas, and R Nair. A mass and energy conserving spectral element atmospheric dynamical core on the cubed-sphere grid. J. Phys: Conference Series, 78(1):012074, August 2007.

[86] H. Tomita, K. Goto, and M. Satoh. A new approach to atmospheric general circulation model: Global cloud resolving model NICAM and its computational performance. SIAM J. Sci. Comput., 30:2755–2776, 2008.

[87] E. F. Toro. Riemann Solvers and Numerical Methods for Fluid Dynamics. A Practical Introduction (2nd Ed.). Springer-Verlag, New York, 1999.

[88] E F Toro. Shock-capturing methods for free-surface shallow flows. Wiley, March 2001.

[89] M. D. Toy and D. A. Randall. Design of a nonhydrostatic atmospheric model based on a generalized vertical coordinate. Mon. Wea. Rev., 137:2305–2330, 2009.

[90] P. Ullrich and C. Jablonowski. A nonhydrostatic atmospheric dynamical core utilizing high-order finite-volume methods. J. Comp. Phys., 231:5078–5108, 2012.

[91] P. Ullrich and C. Jablonowski. Operator-split runge-kutta-rosenbrock methods for nonhydrostatic atmospheric models. Mon. Wea. Rev., 140:1257–1284, 2012.

[92] Paul A. Ullrich, Christiane Jablonowski, and Bram van Leer. High-order finite-volume methods for the shallow-water equations on the sphere. J. Comput. Phys., 229:6104–6134, August 2010.

[93] Hilary Weller, Sarah-Jane Lock, and Nigel Wood. Runge-kutta imex schemes for the horizontally explicit/vertically implicit (hevi) solution of wave equations. Journal of Computational Physics, 252:365–381, November 2013.

[94] L. J. Wicker and W. C. Skamarock. A time-splitting scheme for the elastic equations incorporating second-order Runge-Kutta time differencing. Mon. Wea. Rev, 126:1992–1999, 1998.

[95] David L Williamson, John B Drake, James J Hack, Rüdiger Jakob, and Paul N Swarztrauber. A standard test set for numerical approximations to the shallow water equations in spherical geometry. J. Comput. Phys., 102(1):211–224, 1992.

[96] Yulong Xing and Chi-Wang Shu. A new approach of high order well-balanced finite volume WENO schemes and discontinuous Galerkin methods for a class of hyperbolic systems with source terms. Commun. Comput. Phys, 1(1):100–134, 2006.

[97] Yulong Xing, Xiangxiong Zhang, and Chi-Wang Shu. Positivity-preserving high order well-balanced discontinuous Galerkin methods for the shallow water equations. Adv. Water Resour., 33(12):1476–1493, December 2010.

[98] Chao Yang and Xiao-Chuan Cai. Parallel multilevel methods for implicit solution of shallow water equations with nonsmooth topography on the cubed-sphere. J. Comput. Phys., 230(7):2523–2539, April 2011.

[99] Chao Yang, Jianwen Cao, and Xiao-Chuan Cai. A Fully Implicit Domain Decomposition Algorithm for Shallow Water Equations on the Cubed-Sphere. SIAM J Sci. Comput., 32(1):418–438, January 2010.

[100] G. Zagal, D. Reinert P. Ripodas, and M. Baldauf. The ICON (icosahedral non-hydrostatic) modelling framework of DWD and MPI-M: Description of the non-hydrostatic dynamical core. Q. J. R. Meteorol. Soc, pages 1–17, 2014. DOI: 10.1002/qj.2378.

[101] Y. Zhang and R. D. Nair. A nonoscillatory Discontinuous galerkin transport scheme on the cubed sphere. Mon. Wea. Rev., 140:3106–3126, 2012.

Appendix A

Implementation of Non-hydrostatic Discontinuous Galerkin Atmospheric model

A.1 Euler's system on the cubed-sphere

A.1.1 General curvilinear form

A direct expansion of the Euler system in (x^1, x^2, x^3) coordinates and using the metric terms leads to the following, where the details of the algebraic derivations have been omitted for brevity.

- The 3D compressible Euler system of equations on a rotating sphere in generalized curvilinear coordinates (x^1, x^2, x^3) can be written in tensor form (**Warsi, 1992**):

$$\begin{aligned}
\frac{\partial \rho}{\partial t} + \frac{1}{\sqrt{G}}\left[\frac{\partial}{\partial x^j}(\sqrt{G}\,\rho u^j)\right] &= 0 \quad \{\textbf{Summation Implied}\} \\
\frac{\partial \rho u^i}{\partial t} + \frac{1}{\sqrt{G}}\left[\frac{\partial}{\partial x^j}[\sqrt{G}(\rho u^i u^j + p\,G^{ij})]\right] + \Gamma^i_{jk}(\rho u^j u^k + p\,G^{jk}) &= f\sqrt{G}(u^1\,G^{2i} - u^2\,G^{1i}) - \rho g\,G^{3i} \\
\frac{\partial \rho\theta}{\partial t} + \frac{1}{\sqrt{G}}\left[\frac{\partial}{\partial x^j}(\sqrt{G}\,\rho\theta\,u^j)\right] &= 0 \\
\frac{\partial \rho q}{\partial t} + \frac{1}{\sqrt{G}}\left[\frac{\partial}{\partial x^j}(\sqrt{G}\,\rho q\,u^j)\right] &= 0
\end{aligned}$$

- Where u^i is contravariant wind field, G_{ij} metric tensor, $\sqrt{G} = |G_{ij}|^{1/2}$ is the Jacobian of the transform, $G^{ij} = (G_{ij})^{-1}$, and $i, j, k \in \{1, 2, 3\}$. The associated Christoffel symbols (second kind) are defined as

$$\Gamma^i_{jk} = \frac{1}{2}G^{il}\left[\frac{\partial G_{kl}}{\partial x^j} + \frac{\partial G_{jl}}{\partial x^k} - \frac{\partial G_{kj}}{\partial x^l}\right]$$

- Mathematically elegant but computationally cumbersome!

A.1.2 Perturbed Euler system

Note that we split $\rho = \bar{\rho} + \rho'$, $p = \bar{p} + p'$ and $\rho\theta = (\bar{\rho\theta}) + (\rho\theta)'$ as mean and perturbed state such that the mean state follows the hydrostatic balance.

- Continuity Equation.

$$\frac{\partial \rho'}{\partial t} + \frac{1}{\sqrt{G}}[\frac{\partial}{\partial x^1}\sqrt{G}\rho u^1 + \frac{\partial}{\partial x^2}\sqrt{G}\rho u^2 + \frac{\partial}{\partial x^3}\sqrt{G}\rho u^3] = 0 \tag{A.1}$$

- u^1 -momentum Equation.

$$\begin{aligned}
&\frac{\partial \rho u^1}{\partial t} + \frac{1}{\sqrt{G}}\left\{\frac{\partial}{\partial x^1}[\sqrt{G}(\rho u^1 u^1 + G^{11}p')] + \frac{\partial}{\partial x^2}[\sqrt{G}(\rho u^1 u^2 + G^{12}p')] + \frac{\partial}{\partial x^3}[\sqrt{G}(\rho u^1 u^3)]\right\} \\
&+ \Gamma^1_{11}(\rho u^1 u^1 + p'G^{11}) + 2\Gamma^1_{12}(\rho u^1 u^2 + p'G^{12}) + \Gamma^1_{22}(\rho u^2 u^2 + p'G^{22}) \\
&= f\sqrt{G}(G^{12}u^1 - G^{11}u^2)
\end{aligned} \tag{A.2}$$

- u^2 -momentum Equation.

$$\begin{aligned}
&\frac{\partial \rho u^2}{\partial t} + \frac{1}{\sqrt{G}}\left\{\frac{\partial}{\partial x^1}[\sqrt{G}(\rho u^2 u^1 + G^{21}p')] + \frac{\partial}{\partial x^2}[\sqrt{G}(\rho u^2 u^2 + G^{22}p')] + \frac{\partial}{\partial x^3}[\sqrt{G}(\rho u^2 u^3)]\right\} \\
&+ \Gamma^2_{11}(\rho u^1 u^1 + p'G^{11}) + 2\Gamma^2_{12}(\rho u^1 u^2 + p'G^{12}) + \Gamma^2_{22}(\rho u^2 u^2 + p'G^{22}) \\
&= \sqrt{G}\,\rho f(u^1 G^{22} - u^2 G^{12})
\end{aligned} \tag{A.3}$$

- u^3 -momentum Equation.

$$\begin{aligned}
&\frac{\partial \rho u^3}{\partial t} + \frac{1}{\sqrt{G}}\left\{\frac{\partial}{\partial x^1}[\sqrt{G}(\rho u^3 u^1)] + \frac{\partial}{\partial x^2}[\sqrt{G}(\rho u^3 u^2)] + \frac{\partial}{\partial x^3}[\sqrt{G}(\rho u^3 u^3 + p')]\right\} \\
&= -\rho' g
\end{aligned} \tag{A.4}$$

- Potential temperature Equation.

$$\frac{\partial (\rho\theta)'}{\partial t} + \frac{1}{\sqrt{G}}\left[\frac{\partial}{\partial x^1}\sqrt{G}\rho\theta u^1 + \frac{\partial}{\partial x^2}\sqrt{G}\rho\theta u^2 + \frac{\partial}{\partial x^3}\sqrt{G}\rho\theta u^3\right] = 0 \tag{A.5}$$

- Moisture (tracer) Equation.

$$\frac{\partial (\rho q_k)}{\partial t} + \frac{1}{\sqrt{G}}\left[\frac{\partial}{\partial x^1}\sqrt{G}\rho q_k u^1 + \frac{\partial}{\partial x^2}\sqrt{G}\rho q_k u^2 + \frac{\partial}{\partial x^3}\sqrt{G}\rho q_k u^3\right] = 0 \tag{A.6}$$

In the momentum equations, $f = 2\Omega \sin\phi$ represents the Coriolis term.

A.2 Practical Implementation with terrain-following ζ-coordinates

Let us consider the following "intuitive" definitions separately for the horizontal (cubed-sphere) and the vertical ζ-coordinate systems. The computational domain comprises of the 3D coordinate system (x^1, x^2, ζ). This transformation may be viewed as converting the 3D Euler Cartesian system $(x, y, z) \rightarrow (x^1, x^2, z)$, the cubed-sphere horizontal coordinates, followed by the Gal-Chen & Sommerville (GS) transform $(x^1, x^2, z) \rightarrow (x^1, x^2, \zeta)$.

If $h = h(x^1, x^2)$ is the prescribed mountain profile and z_{top} is the top of the model domain, then the vertical z height coordinate can be transformed to the monotonic ζ coordinate using the following mapping:

$$\zeta = z_{top}\frac{z-h}{z_{top}-h}, \quad z(\zeta) = h(x^1, x^2) + \zeta\,\frac{z_{top}-h}{z_{top}}; \quad h \le z \le z_{top}. \tag{A.7}$$

The Jacobian associated with the transform $(x, y, z) \rightarrow (x^1, x^2, z)$ is

$$\sqrt{G}_v = \left[\frac{\partial z}{\partial \zeta}\right]_{(x^1,x^2)} = 1 - \frac{h(x^1, x^2)}{z_{top}} \tag{A.8}$$

The **total** Jacobian is hence derived in a **sequential** manner: $\sqrt{G}_h \implies$ horizontal metric term (Jacobian) associated with the gnomonic (cubed-sphere) transform. $\sqrt{G}_v \implies$ vertical metric term associated with $z \rightarrow \zeta$, the GS coordinate transformation.

Let $\sqrt{G} = \sqrt{G}_h\,\sqrt{G}_v$ be the **composite** metric term for the Euler system in the (x^1, x^2, ζ) coordinates, which is used for discretizing the Euler equations. Similarly the notations G_h^{ij} and G_v^{ij} are respectively the contravariant terms associated with the horizontal and vertical transformations.

The Euler system defined above can be written in the following compact form:

$$\frac{\partial \mathbf{U}}{\partial t} + \frac{\partial \mathbf{F}_1}{\partial x^1} + \frac{\partial \mathbf{F}_2}{\partial x^2} + \frac{\partial \mathbf{F}_3}{\partial \zeta} = \mathbf{S}(\mathbf{U}), \tag{A.9}$$

where $\mathbf{U}$ is the state vector and $\mathbf{F}_1, \mathbf{F}_2, \mathbf{F}_3$ are the flux functions along the coordinate direction,

and $\mathbf{S}(\mathbf{U})$ denote the source vector. These are defined as follows:

$$\mathbf{U} = \begin{bmatrix} \sqrt{G}\rho' \\ \sqrt{G}\rho u^1 \\ \sqrt{G}\rho u^2 \\ \sqrt{G}\rho w \\ \sqrt{G}(\rho\theta)' \end{bmatrix} \tag{A.10}$$

$$\mathbf{F}_1 = \begin{bmatrix} \sqrt{G}\,\rho u^1 \\ \sqrt{G}\,(\rho u^1 u^1 + p' G_h^{11}) \\ \sqrt{G}\,(\rho u^2 u^1 + p' G_h^{21}) \\ \sqrt{G}\,\rho w u^1 \\ \sqrt{G}\,\rho\theta u^1 \end{bmatrix} \tag{A.11}$$

$$\mathbf{F}_2 = \begin{bmatrix} \sqrt{G}\,\rho u^2 \\ \sqrt{G}\,(\rho u^1 u^2 + p' G_h^{12}) \\ \sqrt{G}\,(\rho u^2 u^2 + p' G_h^{22}) \\ \sqrt{G}\,\rho w u^2 \\ \sqrt{G}\,\rho\theta u^2 \end{bmatrix} \tag{A.12}$$

$$\mathbf{F}_3 = \begin{bmatrix} \sqrt{G}\,\rho\tilde{w} \\ \sqrt{G}\,\rho u^1\tilde{w} + \sqrt{G}_h\,(\sqrt{G}_v G_v^{13}\,G_h^{11}p' + \sqrt{G}_v G_v^{23}\,G_h^{12}p') \\ \sqrt{G}\,\rho u^2\tilde{w} + \sqrt{G}_h\,(\sqrt{G}_v G_v^{13}\,G_h^{21}p' + \sqrt{G}_v G_v^{23}\,G_h^{22}p') \\ \sqrt{G}\,(\rho w\tilde{w} + p') \\ \sqrt{G}\,\rho\theta\tilde{w} \end{bmatrix} \tag{A.13}$$

$$\mathbf{S}(\mathbf{U}) = \sqrt{G}\begin{bmatrix} 0 \\ \sqrt{G_h}\,\rho f(u^1 G^{21} - u^2 G^{11}) - M^1_\Gamma \\ \sqrt{G_h}\,\rho f(u^1 G^{22} - u^2 G^{12}) - M^2_\Gamma \\ -\rho' g \\ 0 \end{bmatrix} \tag{A.14}$$

where the vertical velocity $\tilde{w}$ in the ζ-coordinate, and other geometric terms are defined as:

$$\begin{aligned}
M^1_\Gamma &= \Gamma^1_{11}(\rho u^1 u^1 + p' G^{11}_h) + 2\Gamma^1_{12}(\rho u^1 u^2 + p' G^{12}_h) + \Gamma^1_{22}(\rho u^2 u^2 + p' G^{22}_h) \\
M^2_\Gamma &= \Gamma^2_{11}(\rho u^1 u^1 + p' G^{11}_h) + 2\Gamma^2_{12}(\rho u^1 u^2 + p' G^{12}_h) + \Gamma^2_{22}(\rho u^2 u^2 + p' G^{22}_h) \\
\tilde{w} &= \frac{d\zeta}{dt} = (w + \sqrt{G_v} G^{13}_v\, u^1 + \sqrt{G_v} G^{23}_v\, u^2)/\sqrt{G_v} \\
\sqrt{G_v} &= \left[\frac{\partial z}{\partial \zeta}\right]_{(x^1,x^2)}, \sqrt{G_v} G^{13}_v = \left[\frac{\partial h}{\partial x^1}\right]_{(z)} \left(\frac{\zeta}{z_{top}} - 1\right), \sqrt{G_v} G^{23}_v = \left[\frac{\partial h}{\partial x^2}\right]_{(z)} \left(\frac{\zeta}{z_{top}} - 1\right).
\end{aligned}$$

The Christoffel symbols are defined as follow;

$$\Gamma^1_{11} = \frac{2\tan\xi\tan^2\eta}{\mu^2}, \quad \Gamma^1_{12} = -\frac{\tan\eta\sec^2\eta}{\mu^2}, \quad \Gamma^1_{22} = 0$$
$$\Gamma^2_{11} = 0, \quad \Gamma^2_{12} = -\frac{\tan\xi\sec^2\xi}{\mu^2}, \quad \Gamma^2_{22} = \frac{2\tan^2\xi\tan\eta}{\mu^2}$$

A.2.1 Notes on $(x, y, z) \to (x, y, \zeta) \to (x^1, x^2, \zeta)$ transform

A.2.1.1 Horizontal (u^1, u^2) Momentum Equations.

Let us consider the u^1-equation first. The u^1 momentum equation for perturbed Euler system can be written in terms of horizontal metric terms $\sqrt{G_h}$ and G^{ij}_h associated with cubed-sphere mapping as below:

$$\begin{aligned}
\frac{\partial \rho u^1}{\partial t} + \frac{1}{\sqrt{G}}\left\{\frac{\partial}{\partial x^1}[\sqrt{G}(\rho u^1 u^1 + G^{11}p')] + \frac{\partial}{\partial x^2}[\sqrt{G}(\rho u^1 u^2 + G^{12}p')] + \frac{\partial}{\partial x^3}[\sqrt{G}(\rho u^1 u^3)]\right\} \\
+\Gamma^1_{11}(\rho u^1 u^1 + p' G^{11}) + 2\Gamma^1_{12}(\rho u^1 u^2 + p' G^{12}) + \Gamma^1_{22}(\rho u^2 u^2 + p' G^{22}) \\
= f\sqrt{G}(G^{12}u^1 - G^{11}u^2).
\end{aligned} \tag{A.15}$$

This can be simplified as follows in the (x^1, x^2, z) cubed-sphere shallow atmosphere formulation:

$$\frac{\partial\sqrt{G_h}\rho u^1}{\partial t} + \frac{\partial}{\partial x^1}[\sqrt{G_h}(\rho u^1 u^1 + G_h^{11}p')] + \frac{\partial}{\partial x^2}[\sqrt{G_h}(\rho u^1 u^2 + G_h^{12}p')] + \frac{\partial}{\partial z}[\sqrt{G_h}(\rho u^1 w)] = f^1 - \Gamma_M^1 \equiv S_u^1, \quad \text{(A.16)}$$

where suffix h indicate horizontal metric terms resulting from the cubed-sphere mapping. f^1 and Γ_M^1 are the Coriolis term and geometric term (or cubed-sphere curvature term) which constitute the source S_u^1 for the u^1-momentum equation.

Our goal is further transform Eq. (A.16) into the (x^1, x^2, ζ) system, by utilizing the following differential transforms (**Clark, 1977**). For an arbitrary scalar $\psi = \psi(x^1, x^2, z)$:

$$\begin{aligned}
\sqrt{G_v}\frac{\partial\psi}{\partial x^1} &= \frac{\partial(\sqrt{G_v}\psi)}{\partial x^1} + \frac{\partial(\sqrt{G_v}G_v^{13}\psi)}{\partial\zeta} \\
\sqrt{G_v}\frac{\partial\psi}{\partial x^2} &= \frac{\partial(\sqrt{G_v}\psi)}{\partial x^2} + \frac{\partial(\sqrt{G_v}G_v^{23}\psi)}{\partial\zeta} \\
\sqrt{G_v}\frac{\partial\psi}{\partial z} &= \frac{\partial\psi}{\partial\zeta}
\end{aligned}$$

Now multiplying (A.16) by $\sqrt{G_v}$ and using the definition $\sqrt{G} = \sqrt{G_h}\sqrt{G_v}$, we have:

$$\frac{\partial\sqrt{G}\rho u^1}{\partial t} + \sqrt{G_v}\frac{\partial}{\partial x^1}[\sqrt{G_h}(\rho u^1 u^1 + G_h^{11}p')] + \frac{\partial}{\partial x^2}[\sqrt{G_h}(\rho u^1 u^2 + G_h^{12}p')] + \sqrt{G_v}\frac{\partial}{\partial z}[\sqrt{G_h}(\rho u^1 w)] = \sqrt{G_v}S_u^1 \quad \text{(A.17)}$$

Using the above differential transform for ψ we get

$$\frac{\partial\sqrt{G}\rho u^1}{\partial t} + \frac{\partial}{\partial x^1}[\sqrt{G}(\rho u^1 u^1 + G_h^{11}p')] + \frac{\partial}{\partial x^2}[\sqrt{G}(\rho u^1 u^2 + G_h^{12}p')] + \frac{\partial}{\partial\zeta}[\sqrt{G_h}(\rho u^1 w)] + \frac{\partial}{\partial\zeta}[\sqrt{G_h}\sqrt{G_v}G_v^{13}(\rho u^1 u^1 + G_h^{11}p')] + \frac{\partial}{\partial\zeta}[\sqrt{G_h}\sqrt{G_v}G_v^{23}(\rho u^1 u^2 + G_h^{12}p')] = \sqrt{G_v}S_u^1, \quad \text{(A.18)}$$

$$\frac{\partial\sqrt{G}\rho u^1}{\partial t} + \frac{\partial}{\partial x^1}[\sqrt{G}(\rho u^1 u^1 + G_h^{11}p')] + \frac{\partial}{\partial x^2}[\sqrt{G}(\rho u^1 u^2 + G_h^{12}p')] + \frac{\partial}{\partial\zeta}[\sqrt{G_h}\rho u^1(w + \sqrt{G_v}G_v^{13}u^1 + \sqrt{G_v}G_v^{23}u^2) + \sqrt{G_h}(\sqrt{G_v}G_v^{13}G_h^{11}p' + \sqrt{G_v}G_v^{23}G_h^{12}p') = \sqrt{G_v}S_u^1, \quad \text{(A.19)}$$

By using the relation $\sqrt{G}_v\tilde{w} = w + \sqrt{G}_v G_v^{13}\, u^1 + \sqrt{G}_v G_v^{23}\, u^2$, we get following simplification.

$$\frac{\partial\sqrt{G}\rho u^1}{\partial t} + \frac{\partial}{\partial x^1}\left[\sqrt{G}(\rho u^1 u^1 + G_h^{11}p')\right] + \frac{\partial}{\partial x^2}\left[\sqrt{G}(\rho u^1 u^2 + G_h^{12}p')\right] + \frac{\partial}{\partial \zeta}\left[\sqrt{G}\rho u^1\tilde{w} + \sqrt{G}(G_v^{13}G_h^{11}\,p' + G_v^{23}G_h^{12}\,p')\right] = \sqrt{G}_v S_u^1. \tag{A.20}$$

By symmetry, we can derive u^2-equation.

$$\frac{\partial\sqrt{G}\rho u^2}{\partial t} + \frac{\partial}{\partial x^1}\left[\sqrt{G}(\rho u^2 u^1 + G_h^{21}p')\right] + \frac{\partial}{\partial x^2}\left[\sqrt{G}(\rho u^2 u^2 + G_h^{22}p')\right] + \frac{\partial}{\partial \zeta}\left[\sqrt{G}\rho u^2\tilde{w} + \sqrt{G}(G_v^{13}G_h^{21}\,p' + G_v^{23}G_h^{22}\,p')\right] = \sqrt{G}_v S_u^2. \tag{A.21}$$

A.2.1.2 w-Momentum Equation

Consider the w momentum equation in (x, y, z) coordinates:

$$\frac{\partial\rho w}{\partial t} + \frac{\partial\rho wu}{\partial x} + \frac{\partial\rho wv}{\partial y} + \frac{\partial\rho ww}{\partial z} = -\frac{\partial p}{\partial z} - \rho' g \tag{A.22}$$

The spacial derivates for an arbitrary scaler ψ can be written in terms of the transformed vertical ζ-coordinate as follows:

$$\begin{aligned}
\sqrt{G}_v\frac{\partial\psi}{\partial x} &= \frac{\partial(\sqrt{G}_v\psi)}{\partial x} + \frac{\partial(\sqrt{G}_v G_v^{13}\psi)}{\partial\zeta} \\
\sqrt{G}_v\frac{\partial\psi}{\partial y} &= \frac{\partial(\sqrt{G}_v\psi)}{\partial y} + \frac{\partial(\sqrt{G}_v G_v^{23}\psi)}{\partial\zeta} \\
\sqrt{G}_v\frac{\partial\psi}{\partial z} &= \frac{\partial\psi}{\partial\zeta}
\end{aligned}$$

We can write Eq. (A.22) $\times\sqrt{G}_v$, by substituting $\psi = \rho w$ in the above partial derivates:

$$\frac{\partial\sqrt{G}_v\rho w}{\partial t} + \frac{\partial\sqrt{G}_v\rho wu}{\partial x} + \frac{\partial\sqrt{G}_v\rho wv}{\partial y} + \frac{\partial}{\partial\zeta}\left[\rho w\left(w + \sqrt{G}_v G_v^{13}u + \sqrt{G}_v G_v^{23}v\right) + p\right] = -\sqrt{G}_v\rho' g$$

But we have the following relation between w and $\tilde{w}$

$$\sqrt{G}_v\tilde{w} = w + \sqrt{G}_v G_v^{13}\,u + \sqrt{G}_v G_v^{23}\,v,$$

which further simplifies the w-Eqn.

$$\frac{\partial(\sqrt{G}_v\,\rho w)}{\partial t}+\frac{\partial(\sqrt{G}_v\,\rho wu)}{\partial x}+\frac{\partial(\sqrt{G}_v\,\rho wv)}{\partial y}+\frac{\partial(\sqrt{G}_v\,\rho w\tilde{w}+p)}{\partial \zeta}=-\sqrt{G}_v\rho' g \tag{A.23}$$

In the (x^1, x^2, z) coordinates, we can write the w-Eqn (A.22) by assuming the Jacobian $\sqrt{G}_h$ is independent of z, as follows:

$$\frac{\partial(\sqrt{G}_h\,\rho w)}{\partial t}+\frac{\partial(\sqrt{G}_h\,\rho wu^1)}{\partial x^1}+\frac{\partial(\sqrt{G}_h\,\rho wu^2}{\partial x^2}+\frac{\partial[\sqrt{G}_h\,(\rho ww+p)]}{\partial z}=-\sqrt{G}_h\,\rho' g \tag{A.24}$$

Employing the same **tricks** used for Cartesian case, we can transform $(x^1, x^2, z) \to (x^1, x^2, \zeta)$ in an analogous manner for (A.25) as follows, with $\sqrt{G} = \sqrt{G}_h\,\sqrt{G}_v$:

$$\frac{\partial(\sqrt{G}\,\rho w)}{\partial t}+\frac{\partial(\sqrt{G}\,\rho wu^1)}{\partial x^1}+\frac{\partial(\sqrt{G}\,\rho wu^2}{\partial x^2}+\frac{\partial[\sqrt{G}\,\rho w\tilde{w}+\sqrt{G}_h\,p)]}{\partial \zeta}=-\sqrt{G}\,\rho' g \tag{A.25}$$

where $\tilde{w}$ is the vertical velocity in ζ-coordinate, should be computed with

$$\sqrt{G}_v\tilde{w} = w+\sqrt{G}_v G_v^{13}u^1+\sqrt{G}_v G_v^{23}u^2 \tag{A.26}$$

Dimension Check:

If the independent variable (central angles) x^1, x^2 are non-dimensional as the metric $\sqrt{G}_v$;

$$G_v^{13}=\frac{\partial\zeta}{\partial x^1} \implies \text{dim } m; \quad G_v^{23}\equiv\frac{\partial\zeta}{\partial x^2} \implies \text{dim } m; \quad \sqrt{G} \implies \text{dim } m^2;\ (u^1,u^2) \implies \text{dim } 1/s$$

Then the dimensions matches for both sides of (A.25) and (A.26).